ONE AND TWO DIMENSIONAL NUMERICAL SIMULATION OF DEFLAGRATION
TO DETONATION TRANSITION PHENOMENON IN SOLID ENERGETIC
MATERIALS

A THESIS SUBMITTED TO
THE GRADUATE SCHOOL OF NATURAL AND APPLIED SCIENCES
OF
MIDDLE EAST TECHNICAL UNIVERSITY

BY

BEKİR NARİN

IN PARTIAL FULFILLMENT OF THE REQUIREMENTS
FOR
THE DEGREE OF PHILOSOPHY OF DOCTORATE
IN
AEROSPACE ENGINEERING

MARCH 2010

Approval of the thesis:

ONE AND TWO DIMENSIONAL NUMERICAL SIMULATION OF DEFLAGRATION TO DETONATION TRANSITION PHENOMENON IN SOLID ENERGETIC MATERIALS

submitted by **BEKİR NARİN** in partial fulfillment of the requirements for the degree of **Philosophy of Doctorate in Aerospace Engineering Department, Middle East Technical University** by,

Prof. Dr. Canan Özgen
Dean, Graduate School of **Natural and Applied Sciences** _____

Prof. Dr. Ozan Tekinalp
Head of Department, **Aerospace Engineering** _____

Prof. Dr. Yusuf Özyörük
Supervisor, **Department of Aerospace Engineering** _____

Assoc. Prof. Dr. Abdullah Ulas
Co-supervisor, **Department of Mechanical Engineering** _____

Examining Committee Members:

Prof. Dr. İsmail Hakkı Tuncer
Department of Aerospace Engineering, METU _____

Prof. Dr. Yusuf Özyörük
Department of Aerospace Engineering, METU _____

Assoc. Prof. Dr. Sinan Eyi
Department of Aerospace Engineering, METU _____

Asst. Prof. Dr. Oğuz Uzol
Department of Aerospace Engineering, METU _____

Asst. Prof. Dr. Sıtkı Uslu
Department of Mechanical Engineering, TOBB-ETU _____

Date: _____

I hereby declare that all information in this document has been obtained and presented in accordance with academic rules and ethical conduct. I also declare that, as required by these rules and conduct, I have fully cited and referenced all material and results that are not original to this work.

Name, Last Name: BEKİR NARİN

Signature   :

ABSTRACT

ONE AND TWO DIMENSIONAL NUMERICAL SIMULATION OF DEFLAGRATION
TO DETONATION TRANSITION PHENOMENON IN SOLID ENERGETIC
MATERIALS

Narin, Bekir

Ph.D., Department of Aerospace Engineering

Supervisor   : Prof. Dr. Yusuf Özyörük

Co-Supervisor   : Assoc. Prof. Dr. Abdullah Ulas

March 2010, 129 pages

In munitions technologies, hazard investigations for explosive (or more generally energetic material) including systems is a very important issue to achieve insensitivity. Determining the response of energetic materials to different types of mechanical or thermal threats has vital importance to achieve an effective and safe munitions design and since 1970's, lots of studies have been performed in this research field to simulate the dynamic response of energetic materials under some circumstances.

The testing for hazard investigations is a very expensive and dangerous topic in munitions design studies. Therefore, especially in conceptual design phase, the numerical simulation tools for hazard investigations has been used by ballistic researchers since 1970s. The main modeling approach in such simulation tools is the numerical simulation of deflagration-to-detonation transition (DDT) phenomenon. By this motivation, in this thesis study, the numerical simulation of DDT phenomenon in solid energetic materials which occurs under some mechanical effects is performed. One dimensional and two dimensional solvers are developed by using some well-known models defined in open literature for HMX ($C_4 H_8 N_8 O_8$) with 73 % particle load which is a typical granular, energetic, solid, explosive ingredient. These mod-

els include the two-phase conservation equations coupled with the combustion, interphase drag interaction, interphase heat transfer interaction and compaction source terms. In the developed solvers, the governing partial differential equation (PDE) system is solved by employing high-order central differences for time and spatial integration. The two-dimensional solver is developed by extending the complete two-phase model of the one-dimensional solver without any reductions in momentum and energy conservation equations.

In one dimensional calculations, compaction, ignition, deflagration and transition to detonation characteristics are investigated and, a good agreement is achieved with the open literature. In two dimensional calculations, effect of blunt and sharp-nosed projectile impact situations on compaction and ignition characteristics of a typical explosive bed is investigated. A minimum impact velocity under which ignition in the domain fails is sought. Then the developed solver is tested with a special wave-shaper problem and the results are in a good agreement with those of a commercial software.

Keywords: Munitions, Detonation, Insensitivity, Runge-Kutta,Compaction

ÖZ

KATI ENERJİK MALZEMELERDE YANMA-PATLAMA GEÇİŞİ OLAYININ BİR VE İKİ BOYUTLU SAYISAL BENZETİMİ

Narin, Bekir

Doktora, Havacılık ve Uzay Mühendisliği Bölümü

Tez Yöneticisi   : Prof. Dr. Yusuf Özyörük

Ortak Tez Yöneticisi   : Doç. Dr. Abdullah Ulas

Mart 2010, 129 sayfa

Mühimmat teknolojilerinde, patlayıcı (ya da en genel tanımıyla enerjik malzeme) içeren sistemlerin zarar verebilirlik incelemeleri, duyarsızlık özelliğinin sağlanması açosondan önemli bir konudur. Enerjik malzemelerin değişik tipte mekanik ve ısıl tehditlere karşı verdiği tepkinin hesaplanması, verimli ve güvenli bir mühimmat tasarımı açısından hayati önem taşımaktadır. 1970'lerden beri bu araştırma alanında pek çok çalışma yapılmıştır.

Mühimmat tasarım çalışmalarında deneysel yöntemler, oldukça pahalı ve tehlikelidir. Bu nedenle, özellikle kavramsal tasarım aşamsında, sayısal benzetim araçları 1970'lerden itibaren balistik araştırmacıları tarafından yoğun bir şekilde kullanılmaya başlanmıştır. Bu tarz benzetim araçlarındaki temel modelleme yaklaşımı, yanma-patlama geçişi (YPG) olayının sayısal olarak modellenmesidir. Buradan hareketle, bu tez çalışmasında, katı enerjik malzemelerde bazı mekanik etkiler altında meydana gelen YGP olayının sayısal benzetimi yapılmıştır. Hesaplamalarda, tipik bir enerjik malzeme olan HMX'in ($C_4 H_8 N_8 O_8$) %73 parçacık yüklemeli versiyonu için açık kaynaklarda verilen modelleri kullanarak bir-boyutlu ve iki boyutlu çözücüler geliştirilmiştir. Bu modeller yanma, fazlar arası sürükleme ve ısı transferi etkileşimi ve sıkışma kaynak terimlerini içeren iki faz korunum denklemlerinden oluşmaktadır. Geliştirilen

çözücülerde tanımlanan kısmi diferansiyel denklem (KDD) sistemi yüksek-çözünğrlğklğ merkezi farklar yönteminin zamanda ve uzayda integrasyon için kullanılması ile çözülmüştür. İki-boyutlu çözücü, bir-boyutlu çözücünün temel aldığı tam iki-fazlı modelin, momentum ve enerji denklemlerinde herhangi bir indirgeme yapılmadan genişletilmesi ile geliştirilmiştir.

Bir boyutlu hesaplamalarda, sıkışma, tutuşma, yanma ve patlamaya geçiş karakteristikleri incelenmiştir ve açık kaynak sonuçları ile uyumlu sonuçlar elde edilmiştir.İki boyutlu hesapla-malarda ise farklı hızlarda mermi çarpmasının tipik bir patlayıcı bloğunda sıkışma ve tutuşma karakteristikleri üzerindeki etkisi irdelenmiştir. İncelemeler sonunda belli bir çarpma hızı değerinin altında patlayıcı bloklarında tutuşma meydana gelmeyeceği sonucuna varılmıştır. Bu çalışmanın ardından iki boyutlu çözücü özel tanımlanmış bir dalga-şekillendirici prob-leminin çözümü ile test edilmiş ve elde edilen sonuçların ticari bir yazılım kullanılarak elde edilen sonuçlarla iyi bir uyum içinde olduğu belirlenmiştir.

Anahtar Kelimeler: Mühimmat, Detonasyon, Duyarsızlık, Runge-Kutta, Sıkışma

To my family.

ACKNOWLEDGMENTS

TABLE OF CONTENTS

LIST OF TABLES

LIST OF FIGURES

FIGURES

LIST OF ABBREVIATIONS

ROMAN SYMBOLS

c_j	Shock capturing model constant
d_j	Filtering model constant
D	Drag
E_g	Gas phase total energy
E_p	Solid phase total energy
$\vec{F}, \vec{G}$	Flux vectors
n	Particle number density
p_e	Configuration pressure
p_g	Gas phase pressure
p_p	Solid phase pressure
$\dot{Q}$	Heat transfer
r_i	Shock sensor
r_p	Explosive particle radius
r_{th}	Shock threshold
$\vec{S}$	Source vector
s	Entropy
t	Time
T_g	Gas phase temperature
T_p	Solid phase temperature
u_g, v_g	Gas phase velocity components
u_p, v_p	Solid phase velocity components
$\vec{U}$	Conservative flow variables
U_c, V_c	Contravariant velocity components
x, y	Spatial Cartesian coordinates

GREEK SYMBOLS

γ	Specific heat ratio
Γ_g	Rate of gas generation
Γ_p	Regression of explosive particle
Δ	Step size operator
ϕ_g	Gas phase volume fraction
ϕ_p	Solid phase volume fraction
Φ	Helmholtz free energy
λ_{max}	Maximum characteristic speed
μ_c	Compaction viscosity
ν	Artificial viscosity
ρ_g	Gas phase density
ρ_p	Solid phase density
σ^{sf}	Filtering strength
ξ, η	Spatial computational coordinates
$\xi_x, \xi_y,$ η_x, η_y	Metrics of transformation
ω_k	k^{th} finite difference coefficient in the stencil

SUBSCRIPTS

c_j	Related to boundary
cj	Related to detonation (Chapman-Jouget detonation condition)
g	Related to gas phase phase
$ghost$	Related to ghost cell
i, j	Node indices
p	Related to solid phase
pis	Related to piston
r, l	Shock tube right and left states
x, y	Spatial directions
ξ, η	Computational spatial directions

SUPERSCRIPTS

l	Runge-Kutta stage
n	Time step
sf	Related to selective filtering

CHAPTER 1

INTRODUCTION

1.1 Background and motivation

Deflagration to Detonation Transition (DDT) in reactive gaseous mixtures and energetic solid propellants is an important phenomenon in the combustion science. The response of energetic materials in munitions systems should be deeply investigated to improve the insensitive munitions technology. However, the simulation for the dynamic behavior of DDT is highly difficult due to the complex structure of the problem. Before going further, the insensitive munitions concept will be discussed first.

1.1.1 Insensitive munitions

A simple definition for the insensitive munitions is as follows: An insensitive munitions will not detonate under any conditions other than its intended mission to destroy a specific target. Reduction of hazardous effects caused by energetic-material containing munitions systems is one of the current research interests in munitions engineering field. The studies have been conducted for about the last twenty years.

The possible consequences of accidents caused by munitions are often very severe. Lots of human-live losses and damage on related subsystems are recorded in many accidents, especially occurring during production, storage, transportation and handling of munitions systems [1].

A well known accident related to the usage of conventional munitions systems is the fire aboard the US Forestal aircraft carrier(Figure 1.1). In this fire, which took place in 1967,

lots of aircraft bombs stored aboard got detonated, and 42 aircrafts are lost. Moreover, 134 personnel were killed in this accident with 161 injuries[1, 2].

Figure 1.1: US Forrestal aircraft carrier accident,1967 [2]

Another severe accident occurred in the US Kuwait Camp Doha Base in 1991 during the 1st Golf War (Figure 1.2). After a detonation which took place due to the fire in an artillery re-supply vehicle, three personnel were lost with 52 injuries, and 150 vehicles are destroyed [3, 4].

Figure 1.2: US Kuwait Camp Doha Base accident,1991 [3, 4]

Because of the potential risks of the conventional munitions systems, insensitive munitions concept has been explored, and has been applied to several munitions systems including rocket motors, artillery bombs, warheads etc. Insensitive munitions are expected to fulfill their performance, readiness, and operational requirements on demand while minimizing the probability of inadvertent initiation and severity of subsequent collateral damage to weapon platforms, logistics systems and personnel when subjected to external thermal or mechanical hazardous effects [5, 6]. The external effects (e.g. threats) may be summarized as follows [6]:

- **Fast cook-off**

  This threat may be explained as direct effect of an accidental fire in places where the munitions are stored or handled.

- **Slow cook-off**

  Slow cook-off is caused by smooth increase in temperature in the energetic material. For example, a munitions system under the sunlight may be under slow cook-off threat. Also a fire in an adjacent store may cause slow cook-off in the stored munitions.

- **Bullet impact**

  The munitions under the enemy fire during handling or during storage period may show accidental detonation due to bullet impact.

- **Fragment impact**

  The particles thrown because of the detonation of another munitions may cause detonation on the other system.

- **Shaped-charge impact**

  Shaped-charge is a very special and very effective munitions type. Under enemy fire or under any accidental situation, shaped-charge attack may cause detonation.

- **Sympathetic detonation**

  Blast caused by the detonation of another munitions system may affect other munitions to react in different levels.

All these threats are illustrated in Figure 1.3. Corresponding insensitive munitions testing procedure and reaction types for each threat type are also specified in the figure. The reaction types are schematically explained in Figure 1.4. Here, detonation (Type I) is defined as the most severe reaction type. In case of any hazardous effect, detonation reaction takes place in the reactive medium, and an intense shock (e.g. blast) is formed in the surrounding medium. Moreover, plastic deformation of the munitions case may lead in harmful fragmentation. During the detonation, almost all reactive material is consumed. A similar intense shock formation is observed in the partial detonation (Type II). However, for this time, some part of the case is broken into small fragments, and other parts of the case produce large fragments [5, 6]. Unlike detonation, some part of the reactive material may not detonate during partial detonation. Explosion (Type III) causes the ignition and rapid burning of the confined

energetic material. This builds up locally high pressure values which lead to violent pressure rupture of the confining munitions case. The fragments and unburned energetic material may be spread up to long distances. Blast pressure is also observed in this reaction type although it is not as strong as in Type I and Type II reactions. Deflagration (Type IV) is defined as the ignition and burning of the energetic material with non-violent pressure release. The pressure is not high as a result of a low-strength case or venting through the case walls. Although the munitions case ruptures, fragmentation does not occur. The only significant damage during this reaction type is the heat and the smoke released from the burning energetic material. Burning (Type V) is the least severe reaction type. The munitions case may rupture violently to allow the release of combustion gases. The fire debris may not produce any fatal situation against the personnel. The force produced due to the reaction may impart flight to the munitions. This is called as the propulsion reaction type [7].
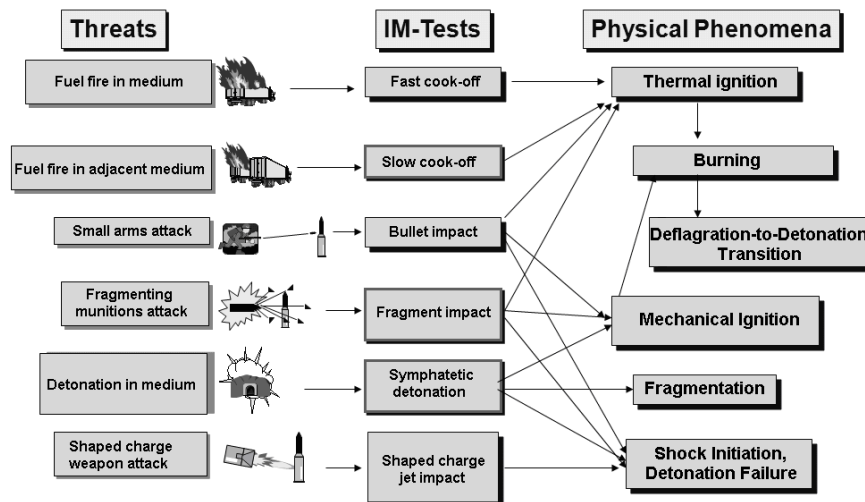
Figure 1.3: Threats, test procedures and related responses of munitions [7]

The objective of designing insensitive munitions is to control the response of a typical munitions system such that the hazardous threats are ordered from "no-reaction" to "Type I". In fact, Type I and Type II are the unacceptable physical responses [7]. In some cases, Type III, Type IV and propulsion are also considered as unacceptable. Therefore, an insensitive munitions design is mainly planned for Type V. If Type V is not possible, Type IV is considered. The main goal for the development of insensitive munitions is enhancing the survivability of logistical and tactical systems, and reducing the risk of injury against some accidental situations [6, 7].
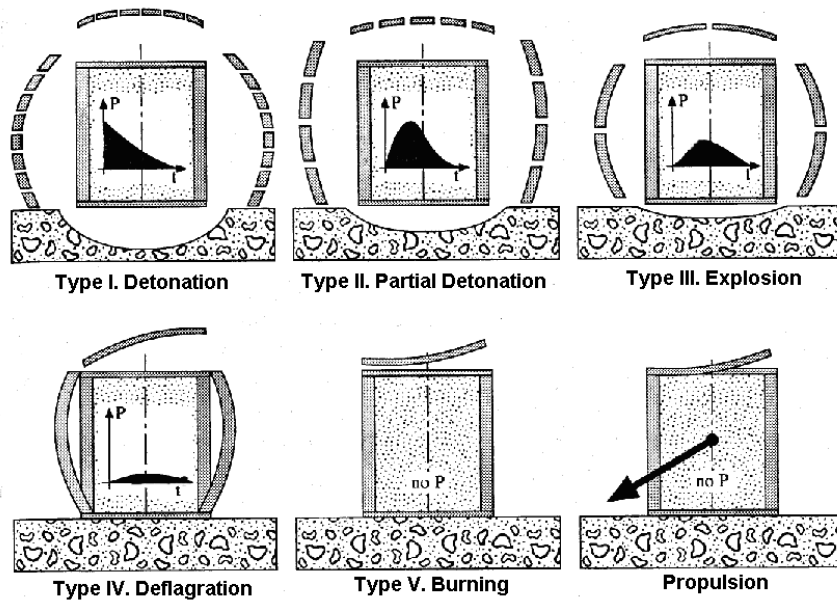
Figure 1.4: Reaction responses for different thermal or mechanical threats [7]

Insensitive munitions design efforts mainly focus on the development of insensitive energetic materials and some specific mechanical design. During the last twenty years, insensitive propellant technology is improved as the researches on composite propellants lead to enhanced capabilities [7]. Specifically, plastic-bonded explosives (PBX) are explored, and applied to the munitions systems in order to increase their insensitivity. However, PBX is itself not sufficient to ensure a complete insensitivity. During mechanical design of a munitions system, there are also some important aspects to be taken into considerations, which are beyond the scope of this study. An example for such an aspect is the usage of special materials in some munitions locations to avoid the Type I, II or III reactions.

In insensitive munitions design, testing process has a vital importance with high costs and danger. For fast cook-off testing, test item is subjected to a direct-fuel fire, and reaction pattern is observed via visualization. The related working-safety regulations must be taken into account since the test item has the possibility to give Type I reaction response. The personnel and test equipments must be sufficiently away, that is at a safe-distance which depends on the explosive amount in the munitions. These circumstances cause to decrease the testing numbers, and increase the effort to develop the numerical simulation techniques [7].

5

The investigation of the response of the reactive materials under some specific mechanical or thermal effects (threats) is very important in order to determine the insensitive features and the performance of the system. During the last $20 - 30$ years, various computational studies are done on the numerical modelling of the reactive material response under some specific conditions.

In this study, the development of a numerical solver is aimed for investigation of the effects of some mechanical or thermal situations on the deflagration-to-detonation transition (DDT) characteristics of reactive materials. The physical properties of HMX (cyclotetramethylene-tetranitramine : $C_4H_8N_8O_8$), which is a typical explosive ingredient, is considered to develop the solver [8, 9, 10]. HMX is widely used in PBX technology as a reactive ingredient. For example, an insensitive munitions explosive, PBX-110, contains HMX as 85 %.

1.1.2   Physical description of DDT phenomenon

DDT is briefly sequential chemical reactions which take place in reactive energetic materials (explosives, rocket propellants, reactive gaseous mixtures, etc.) due to any external thermal or mechanical hazardous effect. Such an effect is generally a thermal or mechanical ignition source. In the rest of this dissertation, the word "explosive" will be used to refer to reactive and/or energetic materials. Figure 1.5 shows a typical explosive bed, which has a *granular* structure.

In the primary stage of a DDT phenomenon, the first few explosive particles in the explosive bed are ignited by an external ignition source as shown in Figure 1.6. This stage of the DDT phenomenon is a very slow process during which the heat conduction between the explosive grains is more effective. Therefore, after the ignition of the first particles, the neighboring particles are ignited as a result of the heat conduction.

The next DDT stage introduces the generation of the hot gases. The hot gases are generated because of the combustion of explosive grains which penetrate through the porous structure of the unburned explosive bed (Figure 1.7). This process is called as *Flame-Spreading* [11, 12, 13, 14]. Flame-Spreading preheats the explosive grains, leading to the formation of a convectively driven flame (deflagration, combustion) front. In this stage, the convection is

Solid Explosive Grains Packed in Strong Confinement
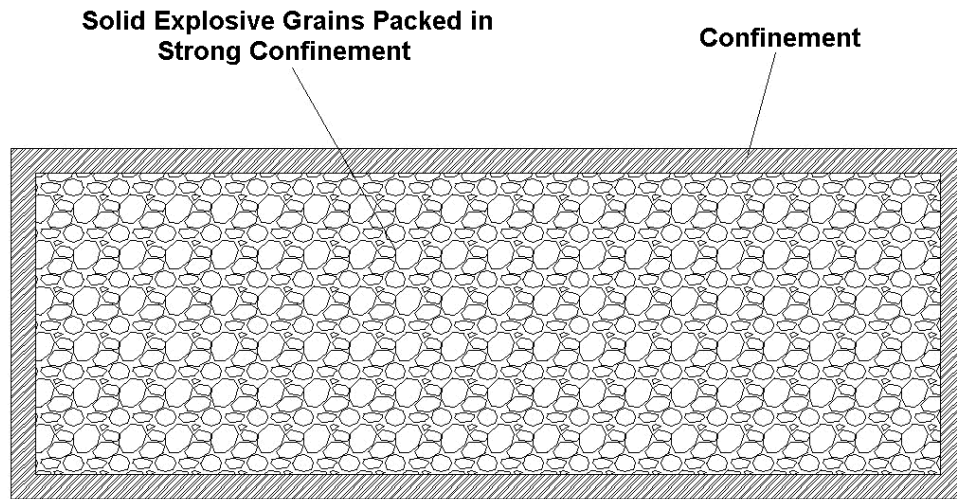
Confinement

Figure 1.5: A typical explosive bed

dominant since the convective heat transfer is much more rapid than the conductive mode.

The convection ignites more explosive grains under the effect of strong confinement, which significantly increase the gas temperature and pressure. The increase is in several orders beyond the deflagration limit. Progressive nature of this process leads in a steady detonation wave [12, 13].

As a summary, the process starts with the heat conduction followed by the convection. Then, a subsonic deflagration wave (flame-front) is observed. Finally, this wave becomes supersonic, and the *steady* detonation occurs. The whole process covering all this sequence is called as Deflagration-to-Detonation Transition (DDT) phenomenon.
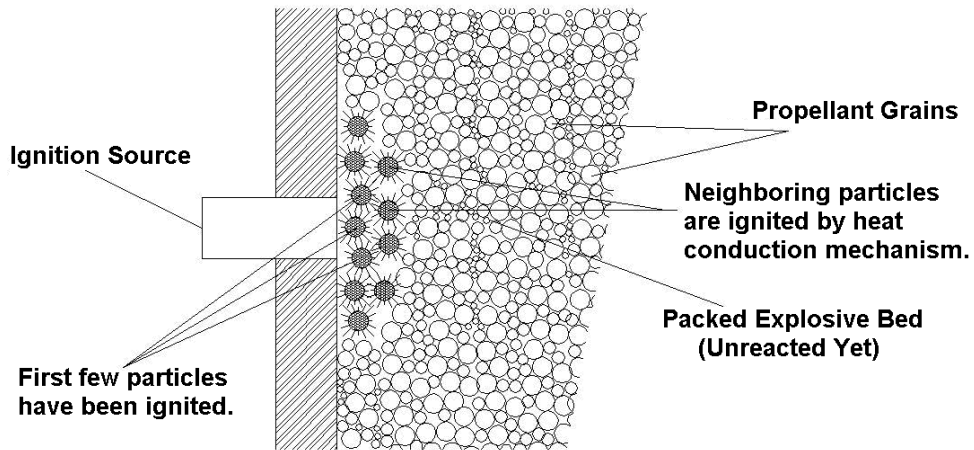
Figure 1.6: Ignition of granular bed

1.2 Historical background and literature survey

Starting from the beginning of the 20th century, lots of experimental and numerical studies have been performed in this research field. The first recorded studies were performed by Chapman and Jouget [15, 16, 17]. These researchers proposed a theory named Chapman-Jouget Theory. This theory assumes that detonation phenomenon occurs in chemical equilibrium and in steady-state conditions. During 1940s, Zeldovich [18], von Neumann [19] and Döring [20] proposed a theory independently that assumes chemical reaction takes place in a finite region and in finite reaction steps which stacks with the shock wave in the medium during a typical DDT phenomenon in reactive gaseous medium. These approaches were applied to simulate the reactive behavior in condensed phase energetic materials. But as mentioned, since these two models take into account steady-state process, a complete dynamic behavior of energetic materials during chemical reactions cannot be modeled with these approaches.

Since 1970s, with the increasing computational capabilities, dynamic simulation studies of DDT phenomenon in both gaseous and condensed phase energetic materials have been performed. Conservation laws were applied with suitable constitutive models. DDT phenomenon is described by applying Continuum Mechanics principles for reactive, two-phase flow and a system of partial differential equations (PDE) is constructed. The phase interaction effects are included in this system of PDE as constitutive models.

One of the pioneering studies of Kuo et al. [21] sheds light to the DDT phenomenon. They

8
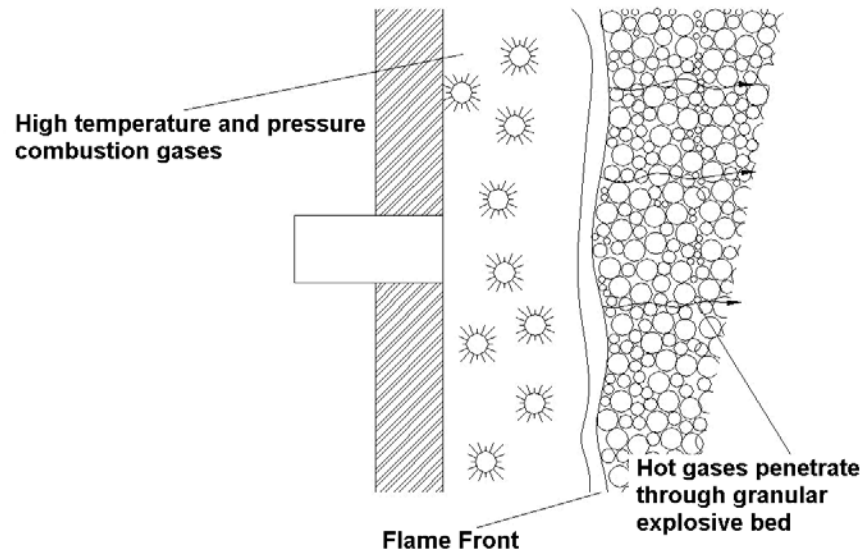
Figure 1.7: Flame spreading phenomenon

also introduce the principles of "continuum mixture theory" in this study. In this study to solve the governing partial differential equations numerically, central differences in space and generalized implicit differences scheme in time are facilitated. They state that this is a very stable and fast convergent numerical scheme and very suitable to handle hyperbolic partial differential equations and their boundary conditions of the present type. The constructed model is applied to a packed bed of granular pellet and the results are compared with those of some experiments. This study concludes that combustion waves are driven by the internal pressure gradient and the flame advances into porous medium by convection. Pressure distribution displays a "continental divide" where gas flows in opposite directions from the peak. Another finding is that burning velocities are nearly 1000 times greater than that of normal burning of propellants.

In [11], flame spreading phenomenon in gas-permeable explosive materials is investigated numerically, and for this purpose a two-phase continuum model with related constitutive equations is employed. For ignition, a simple mass source is assumed, and it is proposed that if the bulk temperature of the propellant exceeds a critical value, the propellant is to be ignited. A pressure dependent burning-rate law is proposed. Interphase drag and heat transfer correlations are described. In this paper, ideal gas equation of state is used for gaseous state calculations and for solid phase equation of state (EOS) is ignored. For numerical cal-
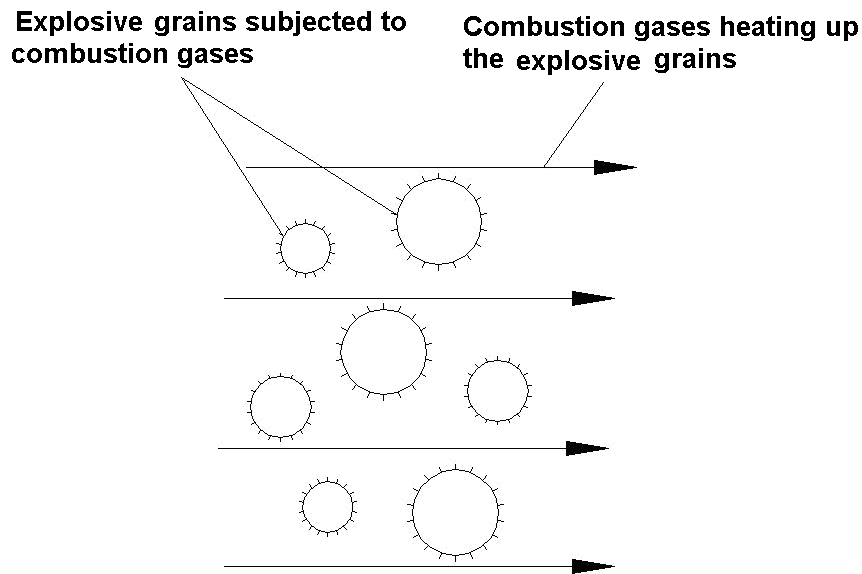
Figure 1.8: Two-phase flow action during DDT sequence

culations, the Richtmyer two-step variation of the Lax-Wendroff scheme is used. The effects of the varying the interphase drag and heat transfer coefficients, burning rate law and initial packing of the propellant bed are explored by the constructed mathematical model.

Krier and his coworkers [12] describe a two-phase continuum-mixture approach applied to the analysis of flame-spreading and combustion of small solid explosive grains. In this model, an unignited bed of small solid explosive grains contained in a cylindrical chamber is assumed and combustion process is sustained by convection in this explosive bed. Although the model explosive grains are located in a cylindrical chamber, the model equations are constructed as one-dimensional. To ignite the bed, an igniter mass flow is described through the bed. For individual explosive grain burning, a pressure-dependent burning rate law is described. Interphase mass, momentum, and energy interactions are described as constitutive models. For gaseous phase, perfect gas law is assumed, and solid phase pressure is ignored. Actually these definitions of gaseous and solid state equations of state are very simplified approaches and just used for initial calculations. A modified form of the explicit two-step Richtmyer variation of the Lax-Wendroff scheme is used for numerical computation. It is proposed that, this technique provides a very stable and, accurate solution to such kinds of problems. The stability is guarantied by applying Courant-Friedrichs-Levy (CFL) criterion since the numerical method used is explicit. Results are shown to agree well with experiments.

10

Becstead et al. [22] also explains a two-phase reacting flow analysis with constitutive modeling to predict DDT possibility in packed bed of granulated HMX. A special criterion is depicted for onset of detonation. It is explained by the results of the calculations that important parameters for DDT are particle diameter, porosity, burn rate and chemical energy of explosives. Besides, it is shown that drag and heat transfer correlations, ignition criterion, and numerical smoothing do not affect the run-up length to detonation.

In the study of Krier and Gokhale [23] "continuum-mixture approach" is used to analyze the transient reactive flow through highly loaded but mobile particles of solid explosive, and to determine whether the high-speed flame front may provide a pressure wave that can interact with the flow to build up a condition of detonation. Constitutive relations used to close the equation system are based on the ignition criterion in terms of the bulk temperature of the solid explosive, the interphase heat transfer coefficient, the interphase drag coefficient, the rate of explosive burning in terms of local pressure and the particle temperature, and finally the axial normal stress to account for the particle-particle interaction. For gaseous detonation products, Noble-Able Equation of State (EOS) is used. Solid phase EOS is proposed in terms of volume fraction of solid phase. The proposed hyperbolic partial differential equation system is solved by a modified form of the explicit two-step Richtmyer variation of the Lax-Wendroff Scheme by using artificial damping to insure stability. It is predicted through the solution of this system that, a rapid build-up of pressure in the bed interior, leading to "continental-divide" type pressure distribution as described by [21] and steep pressure gradients forming a shock-like front.

Gough and Zwarts [24] give the balance equations for heterogeneous two-phase reacting flow. A formal averaging technique is used instead of commonly used continuum-mixture approach. A detailed constitutive modelling has been studied, and the equation system is solved using the explicit MacCormack Scheme.

Gokhale and Krier [25] construct a model describing the two-phase reactive flow through a gas-solid mixture. Both continuum-mixture and separated-flow continuum models are used. In separated flow approach, two distinct flows (i.e., gas and solid) each through a separate control volume are considered and it is assumed that sum of the volumes represents an average mixture volume. The governing partial differential equation systems are solved by two-step finite difference methods (MacCormak and Lax-Wendorf) and results of both approaches (i.e.,

continuum mixture and separated flow) are compared.

Butler and Krier [26] present a technical report, which is also the Ph.D. dissertation of Butler, on deflagration-to-detonation transition (DDT) phenomenon modeling, which was one of the pioneering studies on the subject, for granular energetic materials. A preliminary work which is the base of this study is also performed by Butler and his co-workers [27]. A full continuum model with related constitutive models is proposed by using the separated flow approach and the governing partial differential equation set is solved by Method of Lines (MOL) technique. In this report, three different mechanisms which causes the high-energy granular solid explosive undergo DDT are studied. Butler and Krier presented a similar study with some additional results [28].

Baer and Nunziota [13] propose a two-phase mixture theory which describes the DDT in reactive granular materials. It is indicated that this theory is based on the continuum theory of mixtures and compressibility of all phases and the compaction behavior of the granular materials are also included in the theory. The interphase mass, momentum and energy interactions are included which are based on the known empirical models and these interactions are hoped to obey an entropy or dissipation inequality in mathematical model. For gaseous and solid state pressure definitions JWL and thermo-elastic equations of state (EOS) are used respectively. The constructed model is applied to DDT simulation of a pressed HMX bed. Method of Lines (MOL) technique is used to solve the hyperbolic partial differential equations system. It is proposed that the run-up distance for detonation is in a well agreement with experimental values. Effects of particle size and porosity, bed compaction with different compaction viscosity values are also investigated. In a similar study [14] Baer et al. perform an experimental and theoretical study on a different type of granular explosive which is called CP (cyanotetrazolato pentaaminecobalt perchlorate : $C_2H_{15}N_{10}CoCl_2O_8$).

In [29] Markatos describes a theoretical model to calculate the transient dynamics resulting from pressure wave formation and flame spreading in porous energetic materials. Two-phase continuum-mixture model is constructed. It is mentioned that there are some differences from other studies in constructed mathematical model. The governing partial differential equation system is solved by a fully-implicit finite difference scheme without any time-step limitations.

Baer [30] studies numerical modeling of dynamic compaction of granular materials. A multiphase mixture (i.e. continuum mixture) model which takes into account two-phase non-

equilibrium flow is applied to describe dynamic compaction experiments. Compaction is modeled by a grain distortion description driven by pressure differences. In this study, dynamic compaction behaviors of various inert and energetic materials are investigated by the developed model. It is stated that, the generated multiphase mixture model correctly predicts observed steady compaction wave characteristics.

Powers et al. [31] describes a one-dimensional, two-phase model to describe the detonation of granulated solid explosives. The proposed model satisfies that the mixture mass, momentum and energy are conserved and the mathematical structure of the model is strictly hyperbolic. In this study it is stated that all the constitutive relations and model parameters do not violate the second law of thermodynamics. The Powers et al. stated that in the limit of no chemical reaction or gas phase effects the inclusion of compaction work is in violation of second law of thermodynamics.

The second part of the study described by [31] is presented by Powers et al. in [32]. In this study, ordinary differential equations from continuum mixture theory are solved numerically to determine steady wave structure. It is stated that, in the limiting case where heat transfer and compaction effects are negligible, the model reduces to two ordinary differential equations that have a clear geometrical interpretation in a two-dimensional phase plane. The model proposed in this study is one of the base models used in this Ph.D. study.

In [33] a brief description on DDT phenomenon in reactive granular materials is given. It is stated that, combustion in granular materials begins with ignition of a few grains and the hot product gases generated in early stages of DDT process penetrate into the pores of the inert material. The flame spread is augmented by several orders of magnitude above the deflagration rate driven by thermal conduction alone. This flame spread process can be self accelerating under strong confinement, and then high gas pressures are produced and this leads to detonation. In this study, theory behind the reactive two- phase flow modelling is given. Conservation equations and constitutive relations are expressed and are applied to a one-dimensional model. Constitutive relations are given for the state of inert condensed state and reacted gaseous products; interphase mass, momentum and energy exchange terms; interphase drag; burning rate of a propellant grain in terms of surface-to-volume ratio and finally an ignition criterion for HMX. Mathematical structure is constructed and numerical strategies to solve such a reactive flow problem are stated. Method of Lines (MOL) and

Adaptive Finite Element Methods are explained briefly. Some numerical results are given for HMX.

Bdzil and Son [34] study three different modeling approach for DDT and make a comparison of the results obtained with these three models: (i) Baer-Nunziato Model [13], (ii) Stewart-Prasad-Asay (SPA) Model, and (iii) Bdzil-Kapila-Stewart (BKS) Model. SPA and BKS models are obtained by some asymptotic reductions in momentum and energy conservations. In [35] a similar effort is performed to obtain reduced model equations for DDT modeling. It is concluded that the usage of one-velocity BKS model (i.e. with asymptotic reduction in momentum equations) is more preferable to other models (full-model of Baer-Nunziato and the SPA model with asymptotic reduction in energy equation).

Xu and Stewart discuss and compare the results of three different approaches for the numerical modeling of DDT phenomenon [36]. A new reaction model is presented which is based on autocatalytic decomposition of porous energetic material. In their study, HMX is used as the base energetic material which is one of the most widely used explosive material in calculations of most studies in open literature.

Bdzil et al. [37] make a review study on a previously developed two-phase continuum mixture model of Baer and Nunziato [13]. The phase interaction terms are improved and it is stated that these improved terms supply a better implementation of energy with the dynamic compaction. Determination of constitutive relations of Baer-Nunziota model is clarified and connections between the mechanical and energetic phenomena are investigated.

In [38], non-ideal behavior of condensed phase explosives with metal additives is investigated. First, an unsteady, one-dimensional model is constructed to determine the DDT phenomenon in porous energetic materials without any metal additives. It is assumed that there are three regions in the flow field which are the solid explosive region, a region in which both solid explosive and product gases are included, and an expansion region which only contains product gases. The conservation equations for these three regions are constructed without considering interphase interactions (i.e., interphase drag and heat transfer). Only ignition delay and chemical kinetics are taken into account while constructing the model. HMX is used as the model porous energetic materials and to validate the constructed model, results are compared with that of analytical and experimental studies. Then constructed model is updated to include the metal additive effects.

Xu [39] constructs a two-phase mixture model (i.e. continuum mixture model) to predict DDT in porous energetic materials. It is stated that, since it is difficult to treat the governing partial differential equation system numerically, some simplifications are made on the mathematical model. Three different approaches are studied. These models are defined as "Single Velocity" models and these models include only one velocity term in balance equations then governing system includes fewer partial differential equations to treat. Some comparative calculations are performed between these three different models. A new high-resolution technique is presented in the study. Temporal integration is performed by 3rd order Runge-Kutta method with the property of total variation diminishing (TVD) and spatial integration is performed by 4th order essentially non-oscillatory (ENO) scheme. A new reaction kinetics model is proposed which takes into account the slow and fast energy release and it is stated that this new model is capable to predict the detonation initiation.

Gonthier and Powers [40] study a conservative, upwind method for the solution of two-phase DDT models in energetic granular materials. It is indicated that, conventional numerical methods like "Method of Lines" (MOL) has less ability to resolve fine-scale detonation structure due to numerical smearing caused by artificial viscosity which is included in the mathematical model to insure the stability. The mathematical model is capable to capture shocks associated within each phase and to resolve the fine-scale detonation structure caused by the interaction between the phases. In a preliminary work [41] performed by these researchers, a bulk ignition temperature criterion is facilitated with similar model equations. Whereas in [40] an ignition conservation equation is defined to capture the ignition delay characteristics of the physical model.

In the Ph.D. study performed by Yoh [42], a thermochemical model for an energetic material is constructed by using continuum mechanics approach including phase transformations from solid to liquid to gas with exothermic chemical reactions. A detailed interphase mass, momentum and energy interaction modeling is not given in this study and the phase change mechanism is modeled by a balance of "configuration" forces acting very close the phase boundaries. It is argued that these configuration forces do work and then the effect of these forces is accounted in the overall energy balance to simulate the phase transitions effects. The generated code is modified and a multi-dimensional, multi-material impact hydrodynamic impact code was also generated in this study. The governing equation system is solved by a high resolution numerical method which facilitates fourth order convex essentially non-oscillatory

(ENO) scheme for spatial discretization and third order total variation diminishing (TVD) Runge-Kutta for time integration. In this study, HMX is used as the model energetic material.

The mechanism of detonation formation due to a temperature gradient is studied by Kapila and his co-workers [43]. In this study reduced one-velocity and one-pressure (i.e. with asymptotic reductions in momentum and energy equations) model equations are used as defined by [34] and [35].

In the study of Prokhnitsky [44] a detonation model for granular energetic materials is developed which takes into account the compression of solid-state particles and the presence of a solid component in detonation products. An Arhenius-type homogenous reaction mechanism is proposed. Detonation is said to be initiated by the region of high-pressure and high-temperature gases and it is commented that there is an initiation-pressure limit below which the proposed homogenous mechanism is not applicable.

Chinnayya et al. [45] performs the computation of detonation waves in heterogeneous explosives. It is stated that the heterogeneity of the explosive is caused by compressible multiphase mixtures due to the chemical decomposition of the energetic material or the initial heterogenous formulation. In this study a numerical method is developed to simulate the physical phenomena between the explosive and its surrounding media including inert or reactive materials.

In [46], solution of the Riemann problem for Baer-Nunziato model [13] is performed. In this study, the structure of the Riemann problem for Baer-Nunziato DDT model is studied and an exact solution is formulated. A similar study is performed by Saurel and Massoni [47] before. The HLLC Riemann solver is adapted to Baer-Nunziato model with an Eulerian MUSCL scheme. A shock-tracking scheme is also adapted to the developed algorithm. It is concluded that this shock- tracking scheme is very accurate for one-dimensional DDT applications.

Schewendeman et al. [48] study on Baer-Nunziato model like many others to construct a numerical approach which is a modification of conventional Godunov scheme.

Some studies presented in 13th International Detonation Symposium are investigated. In the study of DeOliveira et al. [49], the model deficiencies arise by the usage of ignition-and-growth model, which is a widely used approach in hydrocode simulations, are resolved by applying some modified reaction models. Actually in this Ph.D. study, ignition-and-growth

model is not applied but this literature gives a clear definition of two-dimensional corner turning type problems. Stevens et al. [50] proposes a numerical model that is capable of accurately simulating the dilute or dense particle (i.e. solid phase) loading conditions. In [51] Chan proposes an analytical model to predict the effects of confinement on the diameter change of an explosive bed (i.e. case-expansion) as a function of the detonation velocity. This model can provide the determination of the case expansion analytically caused by the detonation of the explosive.

A high-order numerical modelling technique is defined by Stewart et al. [52] for the interaction of energetic and inert materials. Energetic and inert materials are modelled using non-ideal equations of state and simulations are conducted by employing high-resolution shock-capturing numerical algorithms.

In [53], [54], and [55], compaction induced energy dissipation for granular energetic materials is taken into account. These studies provide an understanding of the reaction mechanism caused by compaction effects.

Some references related to gaseous detonation are also investigated. Oran et al. [56] released an article related to two-dimensional computations of the propagation of a detonation in a low pressure, argon-diluted mixture of hydrogen and oxygen. It is indicated that a detailed chemical reaction mechanism is used and a typical two-dimensional cellular structure is obtained. In a similar study [57] Togashi et al. perform the numerical simulation of hydrogen-air detonation by using detailed reaction models. Khoklov et al. [58] presents a theoretical approach for predicting the onset of detonation in unconfined turbulent flames. Fedkiw et al. [59] extend the Navier-Stokes equations to model multi-species, chemically reacting gas flows. They use the finite-difference ENO space discretization with the 3rd order TVD Runge-Kutta time discretzation and the developed numerical model is tested with one-dimensional reacting shock-tube and two-dimensional combustor problems. In the study of Gu et al. [60], the results of computations with detailed chemical kinetic schemes for the auto-ignition of stoichiometric gas mixtures under high pressure and temperature are given. In the study of Trotsyuk et al. [61], numerical simulations are performed to study regular and Mach reflections of oblique shock waves in a steady supersonic flow of a homogeneous combustible gas mixture.

1.3 Literature on numerical modelling

A system of partial differential equations (PDE) is set up to investigate the DDT phenomenon. In the literature, various numerical solution methods are presented for the solution of the PDE system. Some of the numerical methods are as follows:

- Method of Lines

- MacCormack Method

- Essentially Non-Oscillatory (ENO) Scheme with Total Variation Diminishing (TVD)

- Godunov's Method

References [40] and [47] use Godunov-type characteristics based numerical models. Mac-Cormack method, Runge-Kutta time integration with spatial central-differencing, and other central difference based methods are applied by Xu[39] and by other researchers. Although it appears that using Godunov-type methods is more suitable for accurate and stable solutions, the construction of the eigenstructure for two-phase DDT phenomenon is not straightforward. In addition to that, the computational cost (time and hardware requirements) is more than that of central-differencing based methods. A disadvantage of central-differencing is its requirement for some additional diffusion terms to ensure the stability of the numerical solution. These additional terms negatively affect the accuracy of the solution. However, recent studies introduce proper artificial diffusion techniques which make central-differencing be more preferable than characteristics-based for DDT simulations.

Strang [62] sets up and compares several central difference schemes. He evaluates some previously done studies on the application of artificial dissipation. Swanson et al. [63], investigate and compare the results obtained using different artificial dissipation models.

Caramana et al. [64] propose a new artificial dissipation formulation for multi-dimensional shock wave computations. Recently a new approach for central-difference numerical models are proposed. In this new approach, spatial filtering (preferably low-pass) is applied to filter high-frequency waves. Some filter transfer functions are employed to avoid the excessive spreading of the shock (i.e. shock-capturing). From the open literature, the studies of two

research groups, Visbal-Gaitonde [65, 66] and Bogey-Bailley [67, 68, 69, 70], are taken into account. The details of these models will be given in the next chapter.

1.4 Objective of the study

The first objective of this thesis work is to develop an in-house numerical solver to simulate the two-dimensional DDT phenomenon of granular explosives. The solver is developed to be executed in a parallel computing environment. As the final target, this solver is considered to be used for the insensitive and optimal munitions design investigations at TUBITAK-SAGE.

In Chapter 2, the description of the one-dimensional model is given. Chapter 3 presents the results obtained using the one-dimensional solver. The extension of the one-dimensional model to two-dimension is discussed in In Chapter 4. The main aspects of the parallel processing are also given in this chapter. In Chapter 5, results of the two-dimensional case studies are given. Finally, the summary of this study and concluding remarks are given in Chapter 6.

CHAPTER 2

ONE-DIMENSIONAL MATHEMATICAL AND NUMERICAL MODEL

Basic mathematical considerations behind the physics of the DDT phenomenon and a detailed description of the numerical solution for 1-D problems are given in this chapter. The mathematical modelling mainly consists of the simulation of a transition process in granular energetic materials. This process is initialized from an accelerating convective ignition front, and ends with a steady state detonation. The following sections describe the process and the mathematical model.

2.1 Physical process

This phenomenon can be briefly described as sequential chemical reactions which take place in reactive energetic materials due to the effect of any thermal or mechanical ignition source. In the first stage of a typical DDT process, only few explosive particles in the explosive bed are ignited [13]. This stage is very slow, and heat conduction between the explosive grains is more effective. Therefore, after the ignition of the first particles, the neighboring particles are ignited by heat conduction mechanism. In the second stage, the hot gases generated by the combustion of explosive grains penetrate through the porous structure of the unburned explosive bed. This event preheats the explosive grains, leading to formation of a convectively driven flame (deflagration, combustion) front [21, 26]. This convective mode of heat transfer is a much more rapid process than conduction; therefore, in this stage convection is dominant. With the effect of strong confinement, the convective heat transfer causes to ignite more explosive grains and this leads to an increase in the gas temperature and pressure by

several orders beyond the deflagration limit. Due to the progressive nature of this process, a steady detonation wave is reached. The physical process that covers all this sequence is called as Deflagration-to-Detonation Transition (DDT) phenomenon [13, 21, 26, 39, 41].

2.2 Mathematical model

Solid (or more generally "condensed-phase") explosive grains are ignited with the thermal actions of the flame-spreading phenomenon which preheats the grains, and flame front passing through the heated up grains [13, 41]. Because of the combustion of explosive grains in a progressive manner under strong confinement, high pressure and temperature combustion gases are generated. Finally the pressure and temperature achieves high values beyond the deflagration limit and steady detonation is reached.

In order to develop a suitable and practical mathematical model, a common approach is to consider that two separate phases of the reactive material take place in the flow domain: *Condensed Phase* for solid explosive grains and *Gaseous Phase* for combustion gases generated by burning of these grains [13]. Unlike the conventional single-phase flow modelling, the studies to model the two-phase flows take into account the interactions between the separate flow regimes. The conservation laws are also applied for separate phases assuming the condensed phase of the reactive material as a continuous medium [13, 21, 41].

There are two basic approaches stated in open literature for mathematical modelling of the DDT phenomenon:

- Continuum-Mixture Approach [21, 25, 35]

- Seperated-Flow Approach [13, 21, 26, 31, 40, 39, 41]

In the continuum-mixture approach, the conservation laws are applied assuming that both separate phases cause a mixture which behaves like a continuum fluid. That is, the mixture of the continuum fields described for both gas and solid phases is treated as a single continuum field [21].

In the separated-flow approach, it is assumed that each phase (solid and gas) is existent in all spatial locations at the same time with different volumetric ratios. That is, each phase is

21

treated as a separate continuum field. Interphase interactions are modelled using analytical expressions, which are included in constitutive relations of the numerical model [13, 31, 40]. Some less sophisticated approaches named as "statistical" and "formal-averaging" are also discussed in the literature [29].

The model used in this study is based on the separated-flow approach, and taken from References [13, 25, 26, 31, 32, 40]. In the development of the mathematical model describing the DDT phenomenon, it is assumed that the solid and gas phases occupy a given spatial position simultaneously. The corresponding local volume fractions sum to unity (Equation 2.1).

$$\phi_g + \phi_p = 1 \tag{2.1}$$

The conservation equations of mass, momentum and energy for the solid and gas phases are written accounting for the gains or losses due to mass (solid phase burning and producing gas), and the associated momentum and energy transfers. The rates at which these transfers occur are based on some constitutive models. Hence, to simulate the DDT phenomenon in the investigated granular explosive bed (i.e. for HMX), the following two-phase, one-dimensional PDE system is described [13, 41]:

Gas and solid phase conservation of mass equations

$$\frac{\partial(\phi_g \rho_g)}{\partial t} + \frac{\partial(\phi_g \rho_g u_g)}{\partial x} = \Gamma_g \tag{2.2}$$

$$\frac{\partial(\phi_p \rho_p)}{\partial t} + \frac{\partial(\phi_p \rho_p u_p)}{\partial x} = -\Gamma_g \tag{2.3}$$

In Equations 2.2 and 2.3, subscripts g and p are used to define the properties of gas and solid phases, respectively. The rate of gas generation due to chemical reactions is determined using Equation 2.4. This expression is actually pressure-dependent and defines the reaction rate of individual explosive grains. Here it is assumed that the mass transfer rate from the solid to the gas phase is a function of the particle radius, r_p, the solid volume fraction, ϕ_p, the solid phase density ,ρ_p, and the gas phase pressure p_g. In this equation a and n are the model constants (Table 2.1).

$$\Gamma_g = \frac{3}{r_p(t)} \phi_p \rho_p a (p_g)^n \tag{2.4}$$
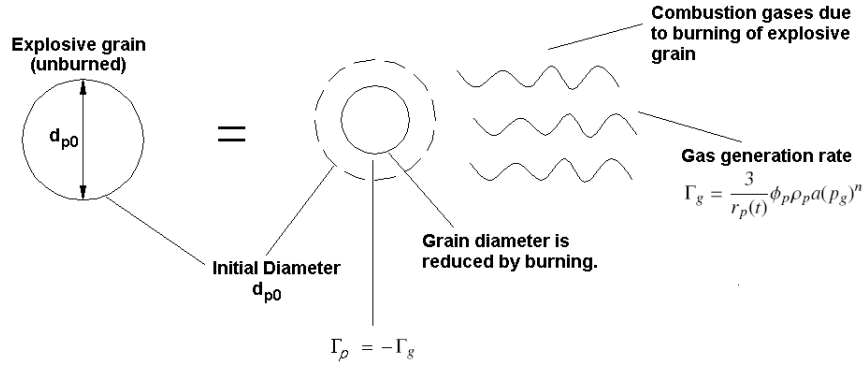
Figure 2.1: Burning of an individual explosive grain and gas generation phenomenon

Physically, the flow of high pressure combustion gases through the grains drives the reaction. As seen in Figure 2.1, the quantity of the explosive grains burn is equal to the combustion gases generated. In other words, the gas generation rate is equal to the negative value of the explosive burning (regression), $\Gamma_p = -\Gamma_g$. This definition for the gas generation rate assumes that the chemical reactions occur instantaneously, i.e. at an *infinite rate* since the pressure levels for a typical DDT process is (on the order of GPa) high .The finite-rate behavior of the deflagration part of the DDT process is not taken into account in this study. The relation defined in Equation 2.4 is used to simulate the burning and thereby regression of an individual explosive particle.

Gas and solid phase conservation of momentum equations

$$\frac{\partial(\phi_g\rho_g u_g)}{\partial t} + \frac{\partial(\phi_g\rho_g u_g^2 + \phi_g p_g)}{\partial x} = \Gamma_g u_p - D \tag{2.5}$$

$$\frac{\partial(\phi_p\rho_p u_p)}{\partial t} + \frac{\partial(\phi_p\rho_p u_p^2 + \phi_p p_p)}{\partial x} = -\Gamma_g u_p + D \tag{2.6}$$

Due to burning of an individual explosive grain in the domain, generated high pressure and temperature gases exert a momentum effect on the unburned or partially-burned explosive grains. This effect is mathematically defined in Equations 2.5 and 2.6 using $\Gamma_g u_g$ and $\Gamma_p u_p$ terms. Figure 2.2 shows the physical representation of interphase momentum interactions.

In Equations 2.5 and 2.6, a drag term (D) is used to simulate the interphase drag interaction (Equation 2.7) due to the relative motion of both gas and solid phases. In Equation 2.7, f_{pg} is
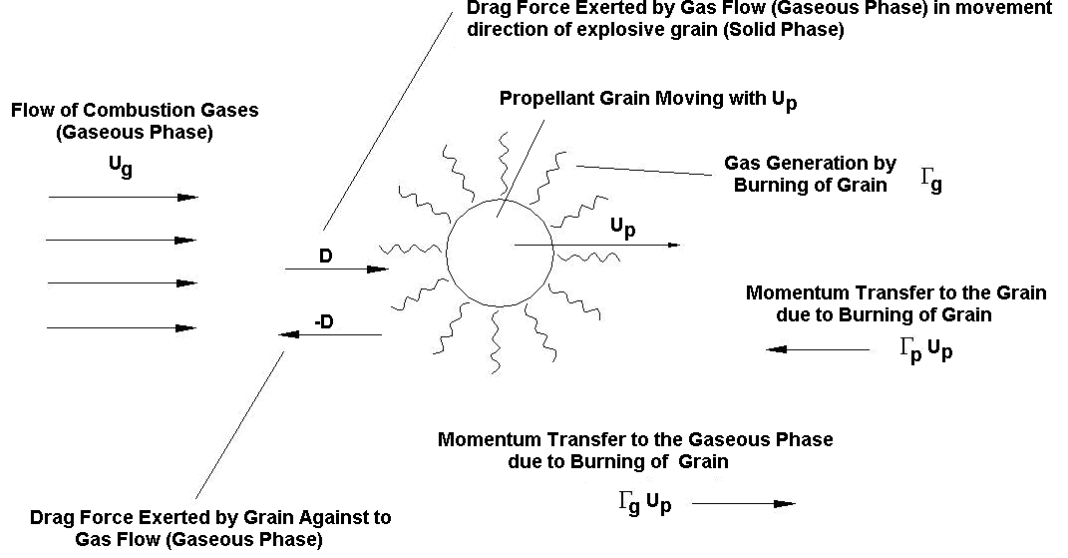
Figure 2.2: Interphase drag interactions and momentum transfers exerted

the drag coefficient and β_{drag} is the model constant for this coefficient.

$$
\begin{aligned}
D &= f_{pg}\left(u_g - u_p\right) \\
f_{pg} &= \frac{\beta_{drag}\phi_g\phi_p}{r_p}
\end{aligned}
\tag{2.7}
$$

Gas and solid phase conservation of energy equations

$$
\frac{\partial(\phi_g\rho_g E_g)}{\partial t} + \frac{\partial(\phi_g\rho_g E_g u_g + \phi_g p_g u_g)}{\partial x} = \Gamma_g E_p - \dot{Q} - D u_p
\tag{2.8}
$$

$$
\frac{\partial(\phi_p\rho_p E_p)}{\partial t} + \frac{\partial(\phi_p\rho_p E_p u_p + \phi_p p_p u_p)}{\partial x} = -\Gamma_g E_p + \dot{Q} + D u_p
\tag{2.9}
$$

In Equations 2.8 and 2.9 $\dot{Q}$ defines the interphase heat transfer interaction between both phases (Equation 2.10). Here h_{pg} is the heat transfer coefficient and, h_{heat} is the model constant for these coefficient (Table 2.1) :

$$
\begin{aligned}
\dot{Q} &= h_{pg}\left(T_g - T_p\right) \\
h_{pg} &= \frac{h_{heat}\phi_g\phi_p}{r_p^{1/3}}
\end{aligned}
\tag{2.10}
$$

The following equation is used to determine the volume fraction change:

24

$$\frac{\partial(\rho_p)}{\partial t} + \frac{\partial(\rho_p u_p)}{\partial x} = -\frac{\rho_p \phi_g}{\mu_c}\left(p_p - p_e - p_g\right) \qquad (2.11)$$

In some of the models defined in open literature [26], the mechanical (or pressure) equilibrium of both phases must be supplied. In contrast to these approaches, our model which is based on the models of [13, 40, 41] does not require such an equilibrium. Instead, both phases are forced toward the mechanical equilibrium via the compaction rate law defined by Equation 2.11. Source term of this equation drives the both phases toward the mechanical equilibrium and, compaction viscosity μ_c characterizes the relaxation rate [37]. The stress exerted on the solid phase because of the configuration change in the explosive bed (i.e. change in volume fractions of each phase) is defined as the *configuration pressure*, which is defined as:

$$p_e = \frac{p_{p0} - p_{g0}}{\phi_{p0}}\phi_p \qquad (2.12)$$

During calculations it is checked that if $p_p - p_e \geqslant 0$. If this condition is not supplied, the minimum value of solid phase pressure (p_p) is set to be equal to configuration pressure $(p_p = p_e)$. After setting the solid-phase pressure, the solid phase temperature and solid phase internal energy are updated. Equation 2.11 is used to determine the updated solid-phase volume fraction during the calculations. Once ρ_p and $\phi_p\rho_p$ are solved using Equation 2.3, the solid phase volume fraction, (ϕ_p), is determined.

Equation 2.13 is used to assure that the total number of particles in the system is conserved. This equation basically simulates the evolution of the particle number density. In the equation, n is the particle number density (Equation 2.14).

$$\frac{\partial n}{\partial t} + \frac{\partial n u_p}{\partial x} = 0 \qquad (2.13)$$

$$n = \frac{3\phi_p}{4\pi r_p^3} \qquad (2.14)$$

A very important question may arise at this point what is the physical considerations behind this number particle evolution equation and, the conservation of particles has a physical meaning? To avoid from numerical problems, a control switch is applied in the calculations, which states that the solid-volume fraction (ϕ_p) does not go below a specific value (i.e. $1x10^{-4}$). This point is defined as the *complete combustion point* [31, 40, 41]. Because of this control

mechanism in the calculations, total number of explosive particles are conserved mathematically. There may be a confusion because of the *n* definition given in Equation 2.14. This is the number particle density, not the particle number. According to Equation 2.13, the number particle density in the system evolves and due to decreases in solid volume fraction and solid particle radius, the number particle density changes while the total number of particles is conserved. The source term *0* of this equation denotes that the total number of particles is conserved and no particle agglomeration or break-up occurs in the system [31].

Equation 2.13 is used to determine the change in the particle radius. During the calculations, the number particle density is determined. After the determination of solid-phase volume fraction by Equation 2.11 with the $\phi_p \geqslant 1x10^{-4}$ constraint, the particle radius is calculated by using Equation 2.14. The regression of a single explosive particle may be modelled by pressure-based burn rate definition given in Equation 2.15 also. But this approach does not assure the conservation of total number of particles in the system and particles are allowed to break-up or coalesce without any proper rule [31]. In some studies including the Baer and Nunziato [13] and the Butler and Krier [26], this approach is used to determine the particle regression but in this study, the model defined by Gonthier and Powers [31, 40, 41] in Equation 2.13 is used.

$$\frac{dr_p}{dt} = -a(p_g)^n \tag{2.15}$$

Equations of states for gas-phase in virial form (Equations 2.16 and 2.17) and for solid-phase in tait form (Equations 2.18 and 2.19) are given below [31, 40]:

$$p_g = \rho_g R_g T_g \left(1 + \acute{\eta}\rho_g\right) \tag{2.16}$$

$$e_g = C_{vg} T_g \tag{2.17}$$

$$p_p = \left(\gamma_p - 1\right) C_{vp}\rho_p T_p - \frac{\rho_{p0}\zeta}{\gamma_p} \tag{2.18}$$

$$e_p = C_{vp}T_p + \frac{\rho_{p0}\zeta}{\gamma_p\rho_p} + E_{ch} \tag{2.19}$$

Virial form means the equation of state form in power series expansion in powers of the density [40]. In Equation 2.16, only first power of the density is taken into account with

model constant (i.e. expansion constant) of $\acute{\eta}$. Tait equation of state form for solid phase supplies us to deal with moderate pressures (i.e. on the order of 10^8 Pa) for the solid phase [40].

All the constitutive relations given above are determined under the 2nd law of thermodynamics [13, 31, 40]. Table 2.1 gives the model constants in the constitutive relations.

Table 2.1: Model constants for 73% particle load HMX [41]

Parameter	Reference	Unit	Value
a	[26, 32]	$[m/(sPa)]$	$2.9x10^{-9}$
β_{drag}	[32, 40]	$[kg/(sm^2)]$	$1x10^4$
h_{heat}	[32, 40]	$[J/(sKm^{8/3})]$	$1x10^7$
C_{vg}	[26, 32, 40]	$[J/(kgK)]$	2400
C_{vp}	[26, 32, 40]	$[J/(kgK)]$	1500
R_g	[32, 40]	$[J/(kgK)]$	$8.5x10^2$
ζ	[32, 40]	$[m^2/s^2]$	$8.98x10^6$
γ_p	[32, 40]		5
$\acute{\eta}$	[32]	$[m^3/kg]$	$1.1x10^{-3}$
μ_c	[32]	$[kg/(ms)]$	$1x10^6$
T_{g0}	[32]	$[K]$	300
T_{p0}	[32]	$[K]$	300
E_{ch}	[13, 26, 32, 40]	$[J/kg]$	$5.84x10^6$

2.2.1 2nd law of thermodynamics suitability of constitutive relations

In a typical DDT modelling study, it is a desirable attempt to investigate that the governing equations do not violate the *Second Law of Thermodynamics* [26, 31, 41]. It is pointed out that the constitutive relations used in the mathematical models defined by [26, 31, 41] are determined by considering the suitability to *Second Law of Thermodynamics*. Since the mathematical model used in this study is based on the models of these researchers, and the *Second Law of Thermodynamics* suitability of the models are well-documented by these researchers, we do not perform any investigations to check the suitability of the models.

2.3   Numerical method

The partial differential equation (PDE) system defined for the solution of a typical DDT problem contains highly coupled and non-linear equations. The PDE system also includes some source terms to define the combustion of explosive grains and interphase interactions. As a consequence, and also due to the existence of disparate eigenvalues, the PDE system is very

stiff. In addition, the DDT phenomenon is inherently unsteady. Therefore, very small time scales exist, and numerical integration of the above system is not straightforward.

Accuracy and robustness of the numerical method to be used becomes important. Although implicit or upwind schemes may be more feasible for numerically stiff equations, it appears that high-order Runge-Kutta time integration methods with high-order central differencing in space works also reasonably well [13, 36]. Controlled artificial diffusion terms are also added to the equations in order to prevent excessive dispersion due to central differencing.

2.3.1 Bogey-optimized Runge-Kutta (RK) time integration with high order spatial discretization and optimized selective filtering-shock capturing (SF) artificial dissipation model

The governing PDE system may be written in a compact from as follows:

$$\frac{\partial \vec{U}}{\partial t} + \frac{\partial \vec{F}}{\partial x} = \vec{S} \tag{2.20}$$

The time integration of Equation 2.20 is achieved through a 6-stage, low-storage Runge-Kutta algorithm and, the spatial derivatives are approximated by using an 11-points stencil central difference method optimized by Bogey and his coworkers [67, 68, 69]. If Equation 2.20 is rearranged as

$$\frac{\partial \vec{U}}{\partial t} = -\frac{\partial \vec{F}}{\partial x} + \vec{S} = \vec{H} \tag{2.21}$$

then, the 6-stage, low-storage Runge-Kutta algorithm is defined as:

$$
\begin{aligned}
\vec{U^{o}} &= \vec{U^{n}} \\
\vec{U^{l}} &= \vec{U^{n}} + \alpha_{l} \Delta t \, \vec{H}\left(\vec{U^{l-1}}\right) \qquad l = 1, \dots, 6 \\
\vec{U^{n+1}} &= \vec{U^{p}}
\end{aligned} \tag{2.22}
$$

Here α_{l} defines weight fractions of the RK stages optimized by [67, 68, 69], and Δt is the time-step.

28

Spatial derivatives are approximated using a 5th order central difference scheme which requires, 11-points stencil with optimized ω_k constants:

$$\frac{\partial F_i}{\partial x} \approx \frac{\sum_{k=-5}^{5} \omega_k F_{i-k}}{\Delta x} \qquad (2.23)$$

In central finite difference schemes, artificial dissipation terms are added to the system of equations in order to prevent the non-physical, high-frequency waves and dispersion errors occurring during the unsteady solution steps. The accuracy of the solution is highly dependent on the artificial dissipation model constant, and this situation brings superficiality to the numerical solution.

In this study, a special artificial dissipation model is facilitated with the optimized RK6 time integration and, optimized central-difference spatial discretization. In the application of this artificial dissipation, independent variables (i.e., each element of $\vec{U}$ vector) are updated after every time step of solution.

$$U_i^{sf} = U_i - \sigma^{sf} D_i^{sf} \qquad (2.24)$$

$$D_i^{sf} = \sum_{j=-5}^{5} d_j U_{i+j} \qquad (2.25)$$

This process is defined as the selective-filtering (SF) [68]. The selective-filtering concept is explored to filter the non-physical high frequency during numerical integration. The existent of such high frequency waves is also defined as the grid-to-grid oscillations [69] and, the purpose of the selective-filtering is to avoid these oscillations. Here, $0 \leq \sigma^{sf} \leq 1$ is the filtering strength, and d_j are the filtering model constants.

After applying the SF process, shock-capturing (SC) is applied. SC is needed to avoid the oscillations around the shock-discontinuities since SF alone may not be enough to avoid the oscillations. SC is also applied directly to the independent variables like in the SF case:

$$U_i^{sc} = U_i^{sf} - \left(\sigma_{i+\frac{1}{2}}^{sc} D_{i+\frac{1}{2}}^{sc} - \sigma_{i-\frac{1}{2}}^{sc} D_{i-\frac{1}{2}}^{sc} \right) \tag{2.26}$$

$$D_{i+\frac{1}{2}}^{sc} = \sum_{j=-1}^{2} c_j U_{i+j}^{sf} \tag{2.27}$$

$$D_{i-\frac{1}{2}}^{sc} = \sum_{j=-1}^{2} c_j U_{i+j-1}^{sf} \tag{2.28}$$

Here, c_j are the shock-capturing model constants. The self-adjusting, shock-capturing filtering strength terms, $\left(\sigma_{i+\frac{1}{2}}^{sc}, \sigma_{i-\frac{1}{2}}^{sc} \right)$, are determined using a shock-sensor, r_i, based on pressure.

$$Dp_i = \frac{-p_{i+1} + 2p_i - p_{i-1}}{4} \tag{2.29}$$

$$Dp_i^{magn} = \frac{1}{2} \left[(Dp_i - Dp_{i+1})^2 + (Dp_i - Dp_{i-1})^2 \right] \tag{2.30}$$

In Equation 2.30, Dp_i^{magn} defines the high-pass filtered pressure value. The shock-sensor is then calculated as follows:

$$r_i = \frac{Dp_i^{magn}}{p_i^2} \tag{2.31}$$

Next, shock-capturing filtering strength is determined:

$$\sigma_i^{sc} = \frac{1}{2} \left(1 - \frac{r_{th}}{r_i} + \left| 1 - \frac{r_{th}}{r_i} \right| \right) \tag{2.32}$$

In the equation, r_{th} is a threshold parameter, and its value ranges from 10^{-10} to 10^{-4} regarding to problem. Finally $\sigma_{i+\frac{1}{2}}^{sc}$ and $\sigma_{i-\frac{1}{2}}^{sc}$ are computed using Equation 2.33:

$$\begin{aligned} \sigma_{i+\frac{1}{2}}^{sc} &= \frac{1}{2} \left(\sigma_{i+1}^{sc} + \sigma_i^{sc} \right) \\ \sigma_{i-\frac{1}{2}}^{sc} &= \frac{1}{2} \left(\sigma_i^{sc} + \sigma_{i-1}^{sc} \right) \end{aligned} \tag{2.33}$$

The model constants of SF-SC artificial dissipation approach are optimized by coupling with the above defined time-integration and spatial discretization. Again the optimized model constants supplied by [67, 68, 69] are taken into account.

2.3.2 Numerical Stability Criteria

During the numerical solution of the hyperbolic equation systems, Courant-Friedrichs-Lewy (CFL) condition (Equation 2.34) must be supplied.

$$\lambda_{max} = (|u| + c)_{max} < \frac{\Delta x}{\Delta t} \tag{2.34}$$

Here λ_{max} denotes the maximum characteristic speed, which includes the absolute value of the speed determined by continuum calculations (i.e. $|u|$) and, the speed of sound in medium (i.e. c). Characteristic speed is the speed of information propagation and, CFL condition assures that this propagation speed does not exceed the numerical calculation speed (i.e. $\Delta x / \Delta t$). To ensure that the stability criterion is supplied, the CFL condition is defined in the following form to determine the suitable time-steps in the calculations.

$$\Delta t = c_t \frac{\lambda_{max}}{\Delta x} \tag{2.35}$$

In Equation 2.35 c_t is the CFL constant for numerical stability. During the calculations c_t value is typically taken as 0.9.

2.3.3 Piston boundary condition

Compaction-induced detonation problems such as bullet-impact are simulated applying a "piston" type boundary condition (BC) in the developed solver. The schematic representation of this application is shown in Figure 2.3.

Solutions of the compaction-induced detonation problems include a compaction wave resulting from the piston impact, which is then convected through the domain of reactive explosive particles and the inert gas (air). As illustrated in Figure 2.4, the piston supplies the inert compaction of the explosive particles up to initiation point, and then an ignition takes place in the explosive bed domain.

The piston effect is provided using wall boundary conditions[71, 72]. The ghost-cell values required during the unsteady computation are determined in each time step as follows:
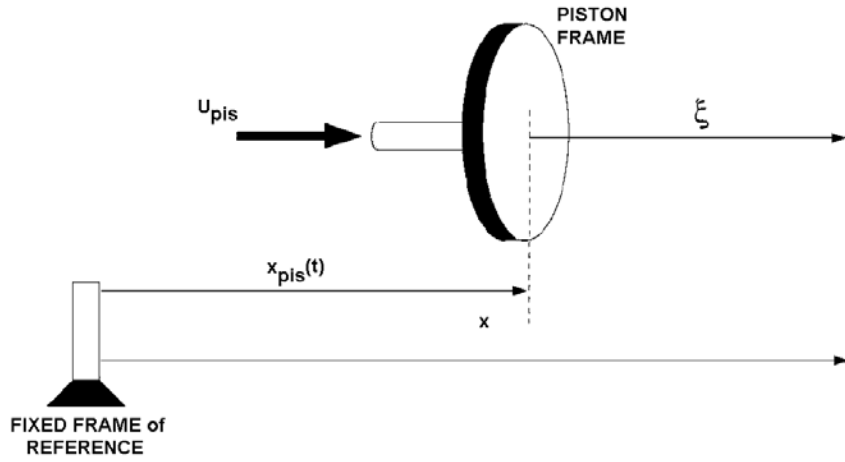
Figure 2.3: Schematic representation of piston BC application
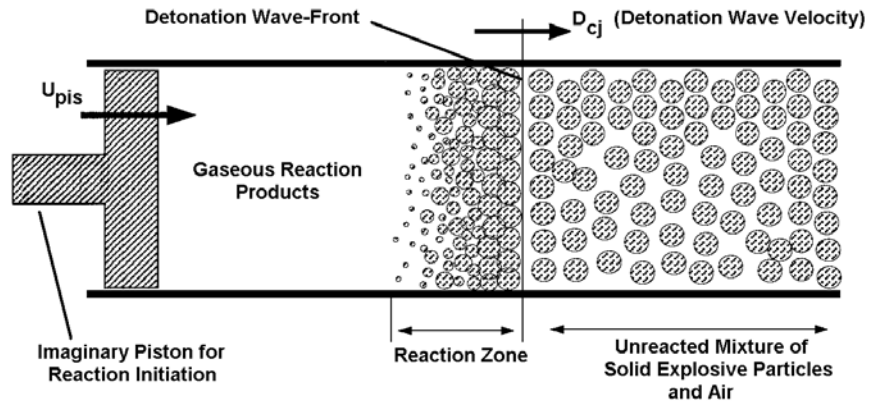
Figure 2.4: Schematic representation of piston induced detonation [40]

$$u_{ghost_0} = u\rangle_0 = -\left(u\rangle_1 - 2 \cdot U_{pis}\right) \tag{2.36}$$

$$\rho_{ghost_0} = \rho\rangle_0 = \rho\rangle_1 \tag{2.37}$$

$$p_{ghost_0} = p\rangle_0 = p\rangle_1 \tag{2.38}$$

$$u\rangle_{-1,..,-4} = u\rangle_{2,..,5} \tag{2.39}$$

$$\rho\rangle_{0,..,-4} = \rho\rangle_{1,..,5} \tag{2.40}$$

$$p\rangle_{0,..,-4} = p\rangle_{1,..,5} \tag{2.41}$$

$$u\rangle_{imax+1,..,imax+5} = u\rangle_{imax,..,imax-4} \tag{2.42}$$

$$\rho\rangle_{imax+1,..,imax+5} = \rho\rangle_{imax,..,imax-4} \tag{2.43}$$

$$p\rangle_{imax+1,..,imax+5} = p\rangle_{imax,..,imax-4} \tag{2.44}$$

For the cases considered, it is assumed that the piston moves at a velocity much lower than the steady detonation wave speed, i.e, $D_{cj} >> U_{pis}$. Therefore, a grid deformation or motion is not applied in the developed solver, and the flux terms are computed as the grid coordinates are fixed. After determining velocity, density and pressure values at $i = 0$ ghost point, the properties at other ghost points (i.e. $i = -1, -2, -3, -4$) are determined by first-order extrapolation of flow properties from interior points.

CHAPTER 3

ONE-DIMENSIONAL RESULTS

The results obtained using one dimensional solver are presented in this chapter. In the first part, application of the high-order Bogey-optimized method is tested based on an inert shock-tube problem, and the suitable model parameters are determined by comparing the results obtained with this high-order method with those of conventional 2nd order numerical method.

In following parts of the chapter, the results of one-dimensional inert compaction, compaction to ignition transition (CIT), and deflagration to detonation transition (DDT) calculations are presented. The results are then discussed by comparing to those presented in the open literature. It is concluded that the results computed using the developed solver are in a good agreement with the results given in the open literature.

3.1 Shock tube problem

For code validation and to test the application of Bogey-optimized RK6 time integration and, 11-points stencil central discretization with SF-SC artificial dissipation [69], a special problem is investigated using the properties of a well-known benchmark shock-tube problem. Shock-tube can be defined as a tool to investigate the chemical reaction kinetics, shock structure type physical phenomena experimentally. A typical shock tube has a constant cross-section area and is divided into two regions which include high pressure and low pressure gases. Conventionally, the high pressure region is called as "driver" while the low pressure region is called as "driven". These regions are separated from each other by a non-permeable diaphragm. In this study, the driver region is on the "left", and the driven region is on the "right".

Once the diaphragm is ruptured by any auxiliary effect, a normal shock wave forms and propagates through the driven region, and an expansion wave forms through the driver section. Since an analytical solution for the shock-tube is available, the numerical simulation of this physical phenomenon is a very useful benchmark problem in computational fluid dynamics (CFD) to test the numerical efficiency of a solver in the development phase.

In the shock-tube problem, all viscous effects are ignored and tube is assumed to be sufficiently long to avoid the reflections at both end of the tube. In this study, a special shock-tube problem called Sod-case problem is used with the following initial conditions [71]:

$$p_l = 1, p_r = 0.1$$

$$\rho_l = 1, \rho_r = 0.125 \tag{3.1}$$

In order to perform shock-tube calculations, solid phase conservation equations and constitutive relations have been switched off in the developed two-phase algorithm. The problem is used by two numerical approaches separately: (i) high-order Bogey-optimized numerical integration method used in this study and, (ii) conventional RK4 time-integration with 2nd order central differencing for spatial discretization and, 2nd order artificial dissipation. The results by using these two different approaches are compared in further parts of this subsection. The obtained results are compared those of the analytical solutions computed by an open-source algorithm published by Toro [72].

The threshold parameter (r_{th}) used in dissipation model by Bogey-optimized RK6 time-integration and, 11-points stencil central differencing algorithm is noted to vary between 10^{-10} and 10^{-4} in the SF-SC method [69].

The 2nd order conventional artificial dissipation applied with the RK4 and 2nd order central differencing is defined in the following form:

$$AD = \epsilon (q_{i-1} - 2q_i + q_{i+1}) \tag{3.2}$$

where;

$$\epsilon = \nu \frac{\lambda_{max}}{\Delta x} \tag{3.3}$$

In Equation 3.3, λ_{max} is the maximum characteristic speed (i.e. eigenvalue) and ν is the model constant. Typical values of ν varies between 0.05 to 0.5.

In Figure 3.1, the solution of the Sod-case shock tube problem using the conventional RK4 time-integration with 2nd order central differencing for spatial discretization and, 2nd order artificial dissipation is given for various model constants. Calculations are performed with $N = 500$ grid-points resolution. It is observed that for $v = 0.05$ and 0.1, some oscillations are existent near the shock discontinuity. However for $v = 0.2$, 0.3, and 0.5, no oscillations are observed. In the light of these results, it is decided to use $v = 0.2$ as the model constant for comparison with the results obtained by use of the Bogey optimized numerical solution method.

In Figure 3.2, the solution of the Sod-case shock tube problem by using the high-order Bogey-optimized method is given for various threshold parameters. It is observed that the oscillatory behavior near discontinuities disappears as the r_{th} value decreases. Therefore for this type of problems, it is concluded that $r_{th} = 10^{-10}$ to 10^{-7} may be used.
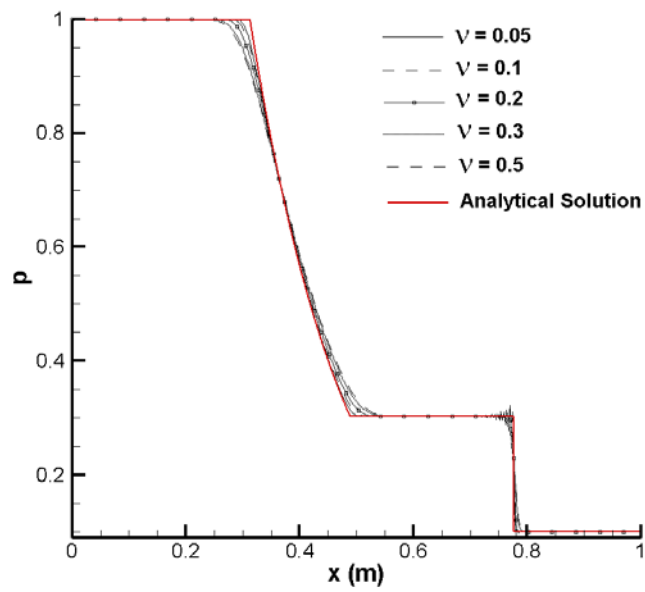
(a)
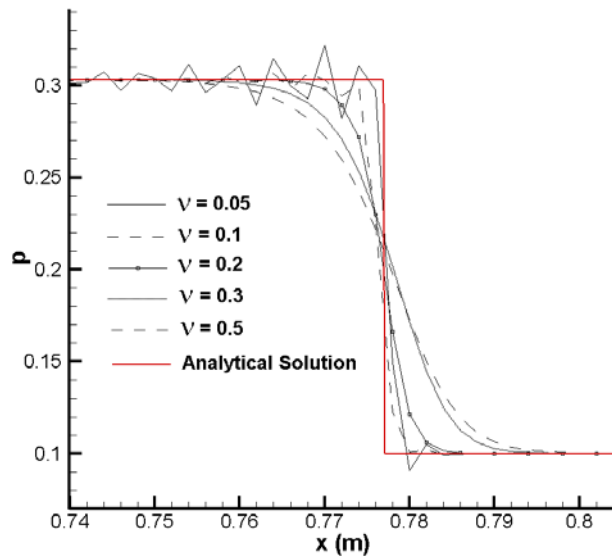
(b)

Figure 3.1: Sod-case shock tube problem solution with conventional RK4 time-integration with 2nd order central differencing for spatial discretization and, 2nd order artificial dissipation (t_{final} =0.15) (a) pressure profile (b) close-up view on shock-discontinuity on pressure profile
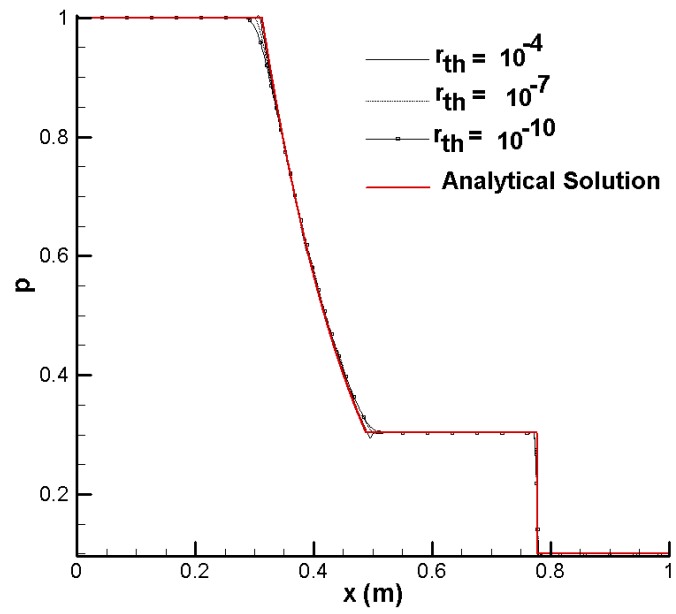
(a)
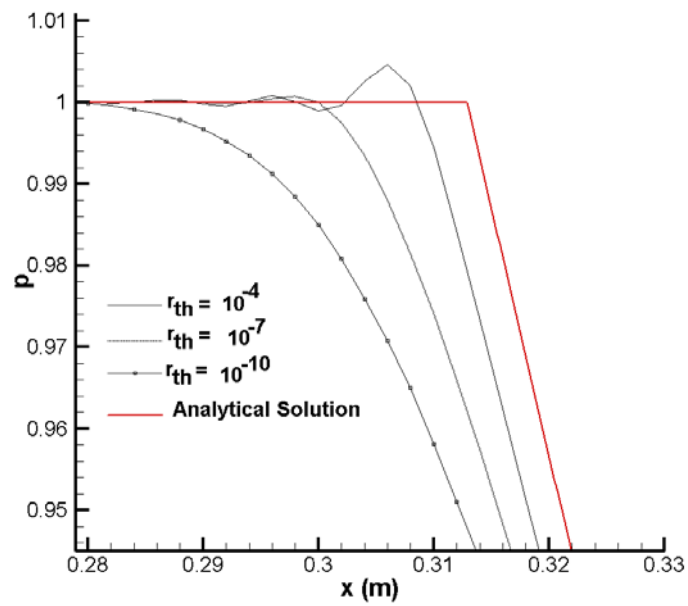
(b)

Figure 3.2: Sod-case shock-tube problem solution Bogey-optimized method (t_{final} =0.15)(a) pressure profile (b) close-up view on shock-discontinuity on pressure profile

The comparison of the results obtained with high-order Bogey-optimized method and, with conventional 2nd order method is given in Figure 3.3. For the same grid resolution ($N = 500$), the high-order Bogey-optimized method gives closer results to the analytical solution than the conventional 2nd order method does. Moreover, it is determined that the high-order Bogey-optimized method gives faster grid-convergence (i.e. grid-independency) than conventional 2nd order method.
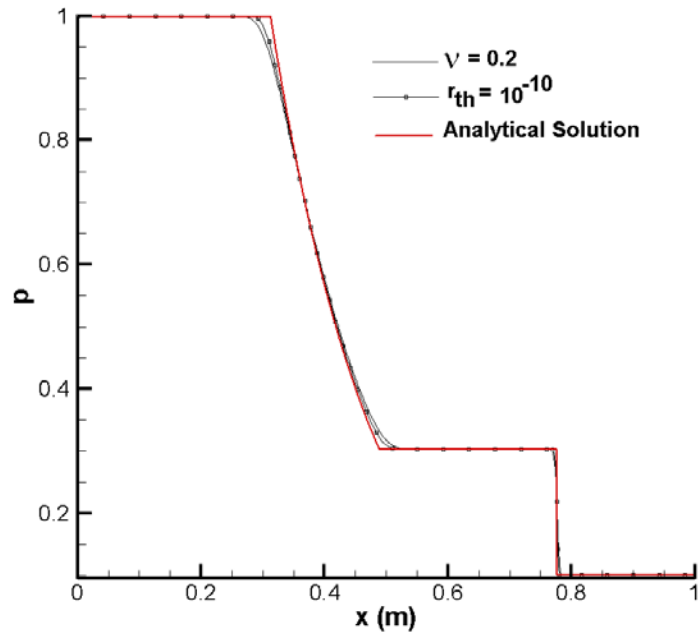
(a)
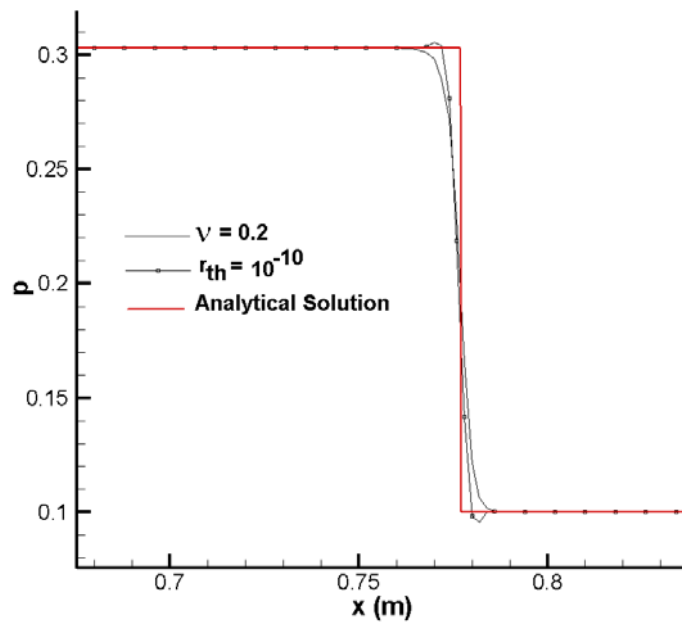
(b)

Figure 3.3: Comparison of the results by using both numerical method for Sod-case shock-tube problem (t_{final} =0.15) (a) pressure profile (b) close-up view on shock-discontinuity on pressure profile

3.2 One dimensional inert compaction, CIT, and DDT calculations

In this section, results of two-phase inert compaction and reactive deflagration to detonation transition (DDT) calculations are presented. Because the physical model in this study is mainly based on the model defined by Gonthier and Powers [31, 40, 41], the results of this section are compared to theirs.

3.2.1 Inert compaction calculations

This calculation aims the simulation of formation and evolution of piston-induced compaction wave. Due to the impact of a moving piston at a specific constant speed ($100m/s$), a mechanical imbalance takes place in the domain, which causes to the formation and convection of a stress wave in two-phase structure of the explosive domain.

Compaction wave simulation is a quite useful tool to validate the application of the mathematical model. For this purpose, a well defined inert model for HMX found in open literature is used [40]. HMX (C_4 H_8 N_8 O_8) is a highly energetic reactive material used in most of present military explosives. In the calculations, a 0.8 m-long bed of HMX is considered. For the sake of similarity with [40], 600 grid points is used in the calculations. It is assumed that the HMX explosive bed is packed to a 73% initial density (i.e. solid phase volume fraction is 0.73) with uniform particles of a surface-mean diameter of 200 μm.

In calculations, interphase drag, heat transfer, and compaction sources are coupled with gas and solid phase convection. To initiate the compaction process, piston BC defined in Chapter 2 is used (Figure 2.4). The conditions defined by [40] are matched for a proper comparison of the results. These conditions are listed below:

- Configuration pressure

  For inert compaction calculations, the following "configuration pressure" form is used instead of Equation 2.12 :

$$p_e = (p_{p0} - p_{g0}) \frac{\phi_p^2}{\phi_{p0}^2} \frac{(2 - \phi_{p0})^2}{(2 - \phi_p)^2} \frac{\ln\left(\frac{1}{1-\phi_p}\right)}{\ln\left(\frac{1}{1-\phi_{p0}}\right)} \tag{3.4}$$

- In solid phase calorific equation of state (Equation 2.19), mass specific chemical energy term (i.e. E_{ch}) is set to zero.

41

- Gas generation term, Γ_g , is set to zero.

- Compaction viscosity is taken as, $\mu_c = 1x10^3$ kg/(m s)

- Interphase drag (Equation 2.7) and heat transfer (Equation 2.10) are used in these calculations [40].

- The domain length is assumed to be 0.8 m.

- Solutions are performed with 600 grid points. (This is the grid resolution used by [40]. For a complete comparison, 600 points grid resolution is used.)

Figures 3.4 and 3.5 show the gas and solid phase pressure and velocity evolutions for inert compaction simulations. In Figure 3.4, pressure profiles of Gonthier and Powers [40] are also given for comparison. It is observed that after the piston impact, a smooth increase takes place both in gas and solid phase pressure values. In the further parts of the process these increases continue up to a steady value. In Figure 3.4(a), the gas phase pressure value rises from its ambient value of 2.58 MPa to a steady value of 25.82 MPa after 0.25 ms from piston impact. It is given in [40] that gas pressure value increases to 26.5 MPa after 0.3 ms from piston impact (Figure 3.4(b1)). In Figure 3.4(c), it is determined that the solid phase pressure value rises from its ambient value of 9.12 MPa to 66.73 MPa again after 0.25 ms from piston impact. In [40] it is pointed out that solid pressure value rises from its ambient value of 9.12 MPa to a maximum value of 67.1 MPa in 0.2 ms. There is a very good agreement between the results of this study and those of Gonthier and Powers.
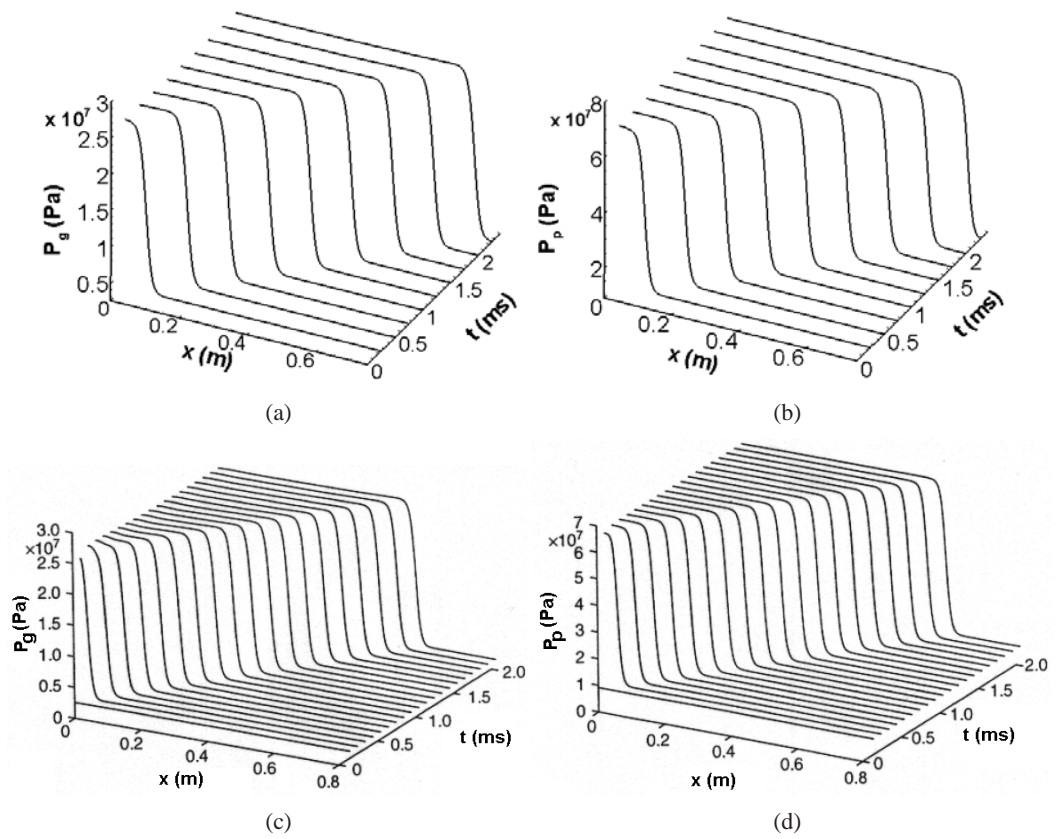
Figure 3.4: Comparison of gas and solid phase pressure evolution for the inert compaction simulation : profiles of current study, (a) gas-phase pressure, (b) solid phase pressure; profiles of Gonthier and Powers [40], (c) gas-phase pressure, (d) solid-phase pressure
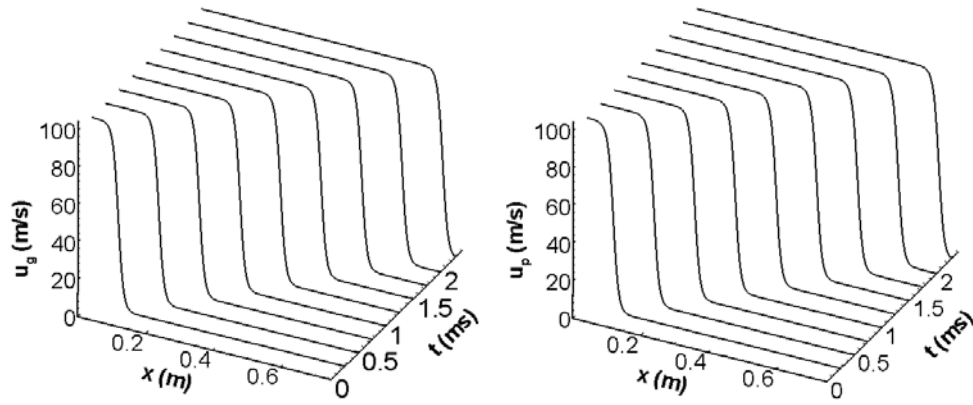
Figure 3.5: Gas and solid phase velocities from current study

The last investigation is done for the comparison of compaction wave velocities. The compaction wave velocity is determined to be about 417 m/s in this study. Gonthier and Powers mention that the compaction wave velocity is predicted to be 418.3 m/s. Gonthier and Powers also say that the experimental compaction wave velocity is 432 m/s. There is a good agreement between the compaction wave velocity predictions of current study and those of Gonthier and Powers [40]. The comparison of solid-phase volume fractions of current study and Gonthier and Powers is given in Figure 3.6. Here it is observed that for both solutions the solid-phase volume fraction values increase to about 0.96 for both solutions. The comparison of solid-phase volume fraction profiles at a specific instant (i.e. at $t = 2$ ms) is given in Figure 3.7. There is a good agreement.

(a)   (b)
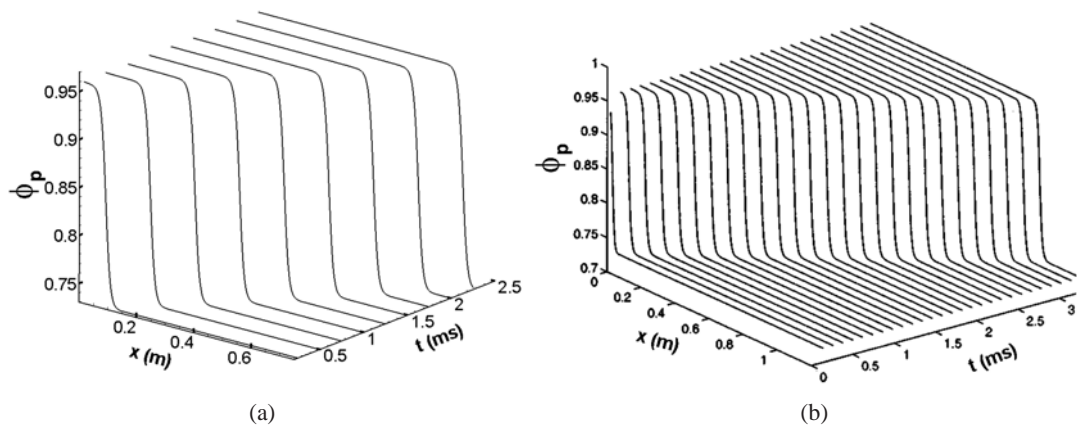
Figure 3.6: Comparison of the solid-phase volume fraction profiles for (a) current study and (b) Gonthier and Powers [40]
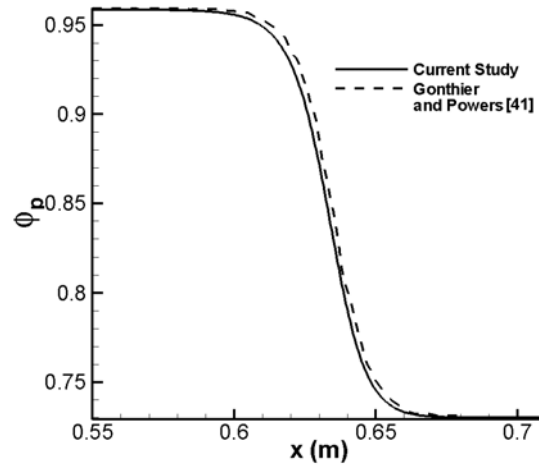
Figure 3.7: Comparison of current result with those of Gonthier and Powers [41] for solid phase volume fraction at $t_{final} = 2$ ms

The comparison of the number particle evolutions is given in Figure 3.8. In inert compaction case, since no reaction takes place, the particle radius does not change. The change in number particle density is driven by the solid volume fraction evolution (Figure 3.6) in the domain. The number particle density value increases to about $2.3x10^{11}$ ($particle/m^3$) behind the compaction wave and, propagates with this constant value. There is good agreement between the both results.
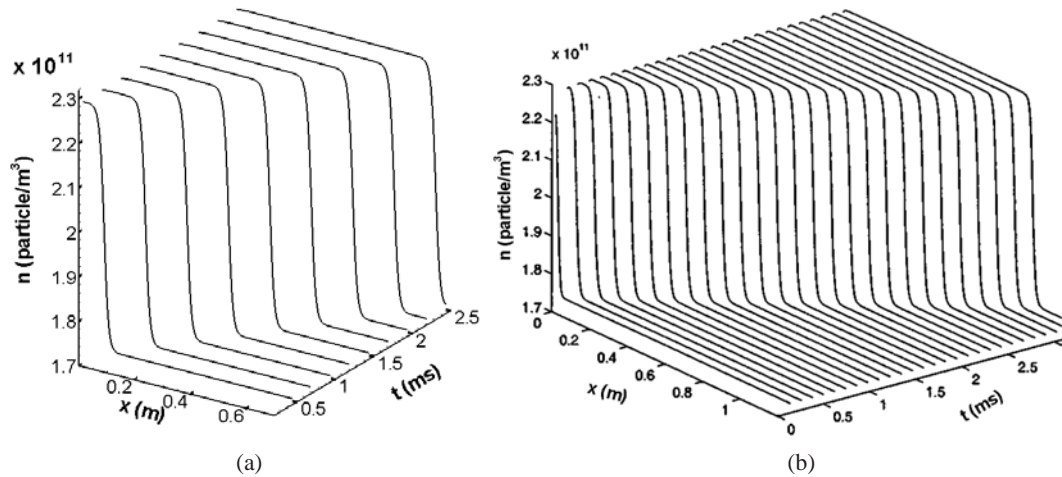
Figure 3.8: Comparison of number particle density evolutions for (a) current study and (b) Gonthier and Powers [40]

Based on the comparisons of the results presented in this section, one may conclude that the application of the mathematical model for the inert compaction problem is validated. This validation gives a very good guidance to validate the mathematical model of reactive DDT model based on this study. In the following section, one dimensional reactive calculations are performed, and the computed results are compared to those obtained by Gonthier and Powers [41].

3.2.2 Reactive solutions: model validation with one-dimensional CIT and DDT calculations

In this section, the reactive physical model is validated against a typical one dimensional CIT and DDT problem. Similar to the inert compaction problem, the model defined for HMX in open literature is used. In calculations, compaction induced detonation is taken into account, and therefore, piston boundary condition explained in Chapter 3 is applied on the left boundary. On the right boundary, outflow boundary conditions are applied [40, 41] employing a simple extrapolation method for the flow variables from interior points.

Before performing the comparative calculations, some numerical investigations are performed to show the grid independency of numerical solutions by using the high-order Bogey-optimized numerical method and conventional 2nd order method. Solutions are computed at grid resolutions of $N = 1000, 2000, 4000, 8000$ and 16000 nodes ($\Delta x = 1/N$). The results are plotted in Figure 3.9. On the left, the full scale views of gas phase pressure profiles are shown, while close-up views for the peak regions of the these profiles for calculations with both artificial dissipation models are shown on the right. It is evident that as the grid resolution is increased, peak pressure values show a converging behavior. It is observed that solutions with the SF-SC model, peak pressure value increases from 13.9 GPa to 14.51 GPa for 1000 and 8000 grid resolutions, respectively (Table 3.1). Similarly, for the solutions with the 2nd order AD model, peak pressure value increases from 12.61 GPa to 14.45 GPa for 1000 and 16000 grid resolutions. It is observed that, calculations with the high-order Bogey-optimized method show faster grid-convergence than those of the conventional 2nd order method. Our criterion here is that the % deviation of peak pressure values for different grid resolutions is less or equal to 1 %. For the high-order Bogey-optimized method, deviation between 2000 grid points and 4000 grid resolution is 0.97 %. Whereas for the conventional 2nd order method, we may obtain the deviation of 0.9 % between 8000 and 16000 grid resolution.
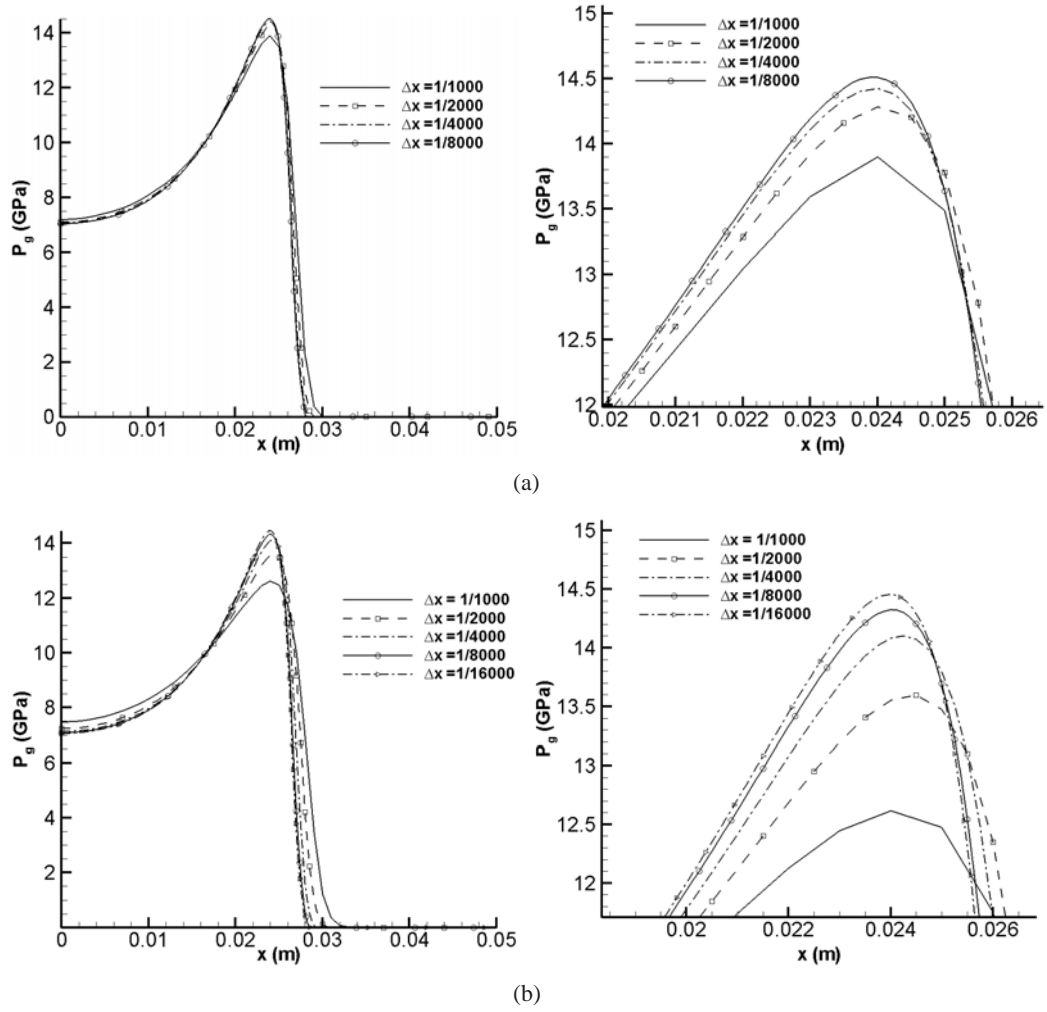
Figure 3.9: Variation of gas phase pressure values with different grid resolutions by using (a) the high-order Bogey-optimized method and, (b) the conventional 2nd order method

Table 3.1: Grid convergence results

Grid Points Resolution	Bogey − optimized Method	% Deviation	Conventional 2nd Order Method	% Deviation
1000	13.9 GPa		12.61 GPa	
2000	14.28 GPa	2.66	13.59 GPa	7.21
4000	14.42 GPa	0.97	14.1 GPa	3.62
8000	14.51 GPa	0.62	14.32 GPa	1.54
16000	−	−	14.45 GPa	0.9

The deviation between 2000-point and 4000-point grid resolutions goes under 1% for the high-order Bogey-optimized method. It is concluded that $N = 2000$ grid points (i.e. $\Delta x = 1/2000m$) may be used for the high-order Bogey-optimized method in order to obtain grid independent solutions. Whereas for the conventional 2nd order method, $N = 8000$ grid points

are needed to assure grid independency. Therefore, considering its fast grid-convergence behavior, the high-order Bogey-optimized method is selected for the computations.

After determining the grid-independency behavior of the numerical model for the DDT problem, calculations are performed to simulate the transition from compaction to ignition and, from deflagration (i.e. combustion) to detonation using a 5000-points grid resolution. Although converged results are obtained with 2000-points grid resolution, the one-dimensional calculations given in this subsection are performed with 5000-points grid resolution. The unsteady profiles are obtained in the time range of $t_{final} = 5$ and $95\,\mu s$ after the imaginary piston impact which starts the process. In the calculations ignition is assumed to occur when the solid phase bulk temperature (T_p) exceeds a specific *ad hoc* value of 310 K [41]. The effect of this ignition criterion is investigated in further parts of this chapter.

Instantaneous profiles are shown in Figures 3.10 and 3.14 to investigate the CIT and DDT mechanisms. In Figure 3.10 gas phase velocity values determined in this study and by Gonthier and Powers are shown. There is a very good agreement between both results. In Figure 3.10(a) basic processes for typical CIT and DDT phenomena are explained. After the piston impact it is observed that an inert compaction wave forms and propagates away the virtual piston surface. This stage is shown in detail in Figure 3.11. It is observed that for the time interval of $t = 0 - 26\,\mu s$, inert compaction wave propagates with a speed of about 3100 m/s. At $t = 26\,\mu s$, it is observed in gas velocity profile, the ignition of the explosive particles takes place with a sharp increase in gas velocity from $100\,m/s$ to about $1200\,m/s$. This point is called as the "ignition point" and all this phenomenon is defined as the compaction to ignition transition (CIT). The prediction at $26\,\mu s$ for ignition is in a very good agreement with the $30\,\mu s$ prediction of Gonthier and Powers [41]. In another study, Baer and Nunziato also state that time to ignition is determined to be $33\,\mu s$ [13].
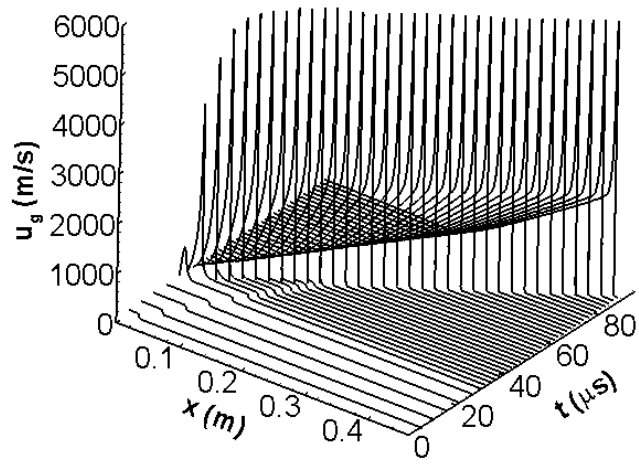
(a)
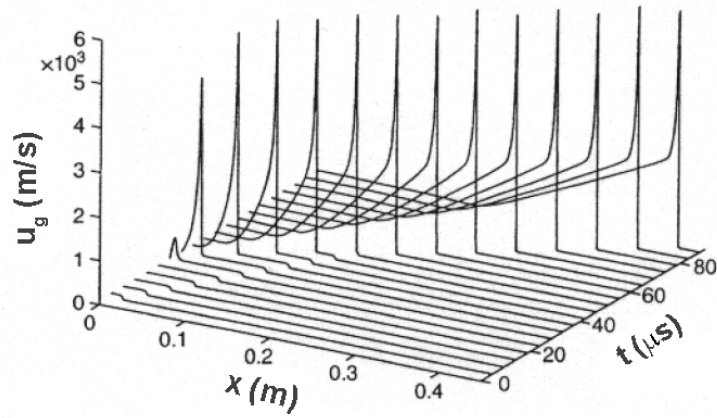
(b)

Figure 3.10: Grid-independent gas phase velocity profiles (a) Current study (b) Gonthier and Powers [41]
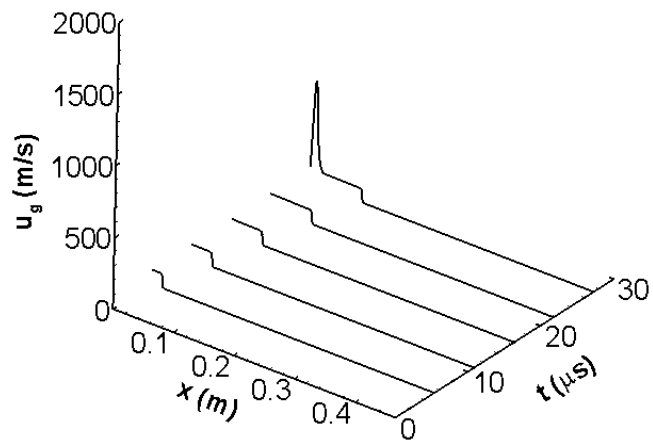
Figure 3.11: Close-up view of gas-phase velocity profile for CIT point

After the ignition of explosive particles, a high pressure and temperature region forms behind the compaction wave (Figure 3.12). In this region explosive particles are ignited by their neighboring particles by heat conduction mechanism as defined in Chapter 1. Burn rate in this combustion (deflagration) stage is relatively slower in this region. Then generated hot gases in high pressure and temperature region penetrate through the porous structure of the explosive and then by the effect of this mechanism burn rates increase in the domain. This increase causes the formation of a detonation wave front in the domain. Since being faster than the compaction wave, this detonation wave catches-up the compaction wave and overtakes it (Figure 3.13). After this point a single wave propagation behavior is observed without any compaction wave in domain. During all this flame propagation, gas pressure and temperature increase in the domain, and burn rate also accelerates and, this acceleration goes up to a specific point and after which, pressure and temperature in the domain are not enhanced further. This specific point is defined as the detonation transition point. All the processes starting from the slow-burn rate deflagration up to the steady detonation is defined as the DDT phenomenon. After DDT is achieved, a steady detonation wave propagates in the domain. It is observed from Figure 3.10 that the transition to detonation takes place at about $t = 55 \ \mu s$ after piston impact. Spatial location of the transition point is about $x = 0.18 \ m$. To determine the post-detonation properties (i.e. detonation pressure (P_{cj}) ,temperature (T_{cj}) and velocity (D_{cj})), this point is taken as reference.
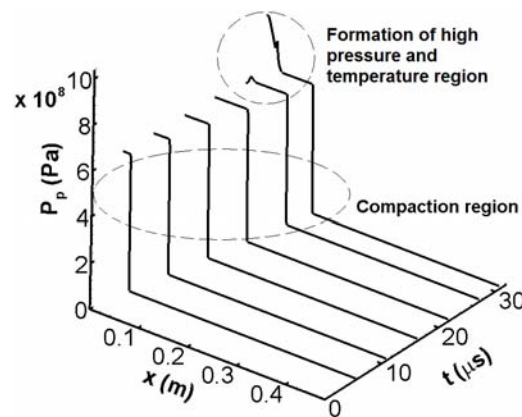
Figure 3.12: Formation of high pressure and temperature region
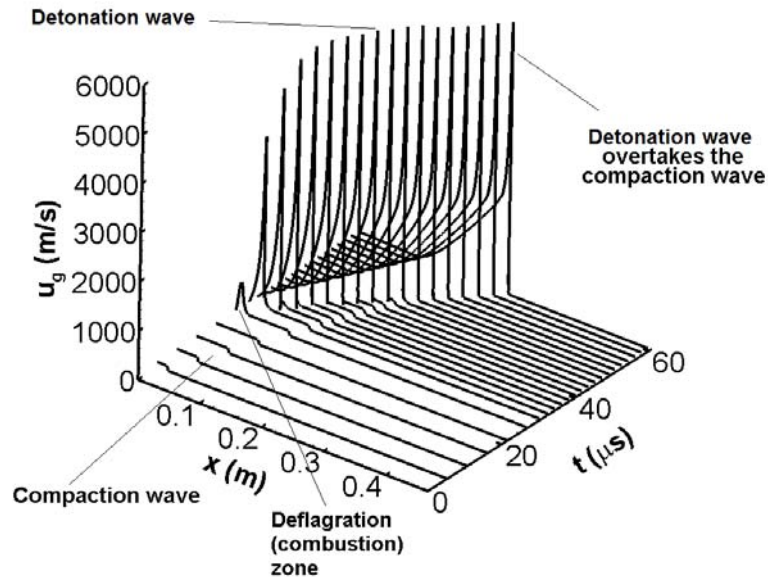
Figure 3.13: Overtaken of compaction wave by detonation wave

In Figure 3.14, computed gas and solid phase pressure profiles are shown and compared to the results given by Gonthier and Powers [41]. The results are again in a good agreement. For gas phase pressure profiles, it is observed that the peak pressure values after steady detonation behavior is achieved at about 25 GPa for both studies. Similarly, in solid phase pressure profiles for both solutions, the pressure value increases to about $6x10^{8}$ Pa in the compaction region, and the wave propagates steadily at this value with a speed of about 3100 m/s up to the ignition point. The gas and solid phase temperature profiles are given in Figure 3.15. The post detonation gas-phase temperature value given in Table 3.2 is determined from these profiles.

(a)

(b)
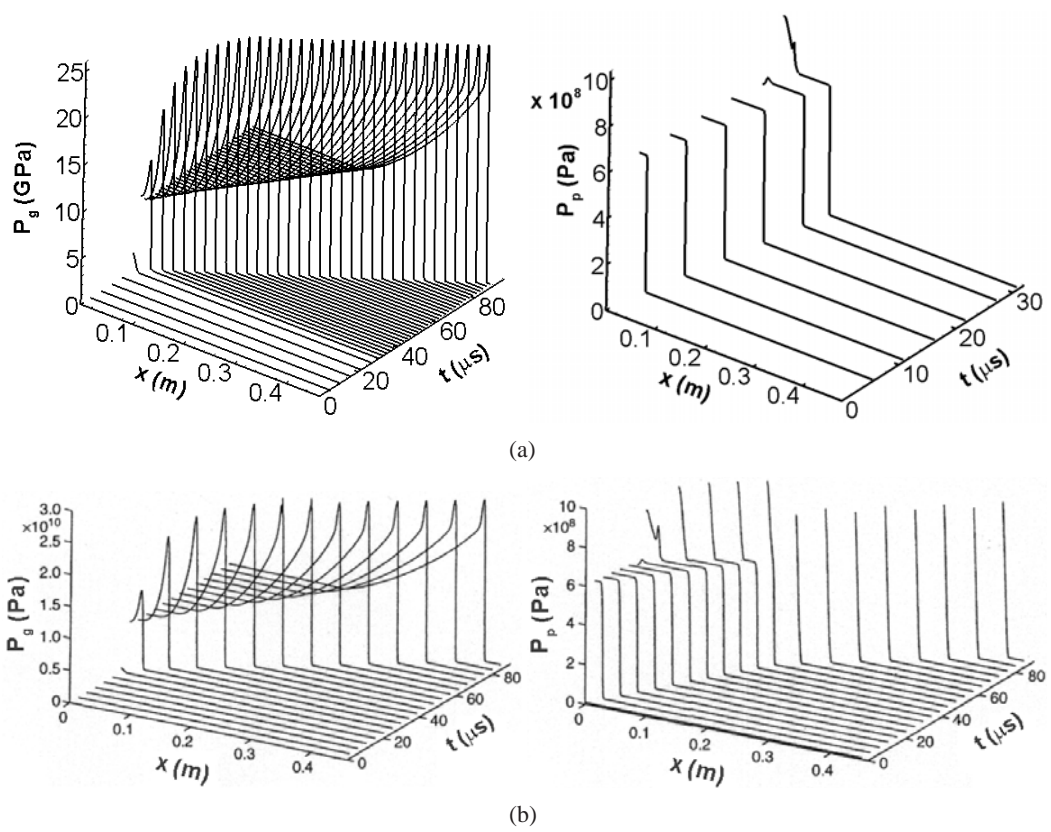
Figure 3.14: Grid-independent gas and solid phase pressure profiles (a) Current study (b) Gonthier and Powers [41]
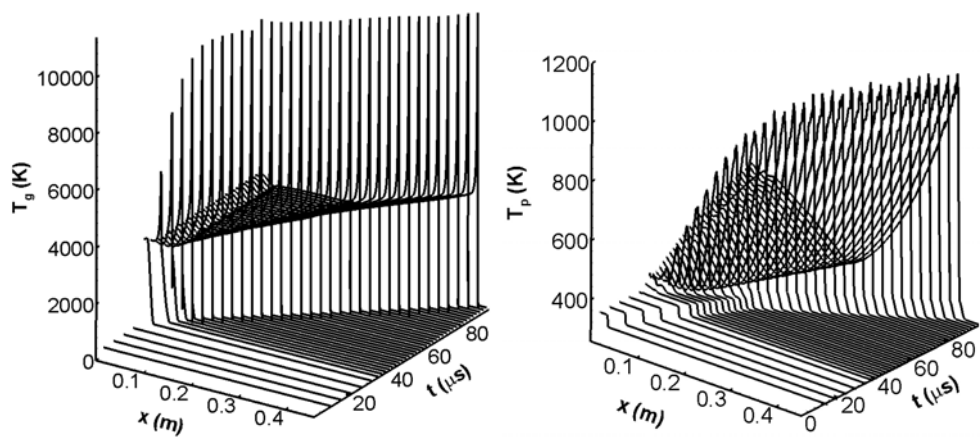
Figure 3.15: Gas and solid phase temperature profiles for current study

The grid independent, steady peak values (peaks of detonation waves) are compared in Table 3.2 to those obtained using a thermochemical code named EXPLO5 [73, 74, 75] and to those of the transient calculations of Baer and Nunziato [13]. In the table, P_{cj}, T_{cj} and D_{cj} denote the detonation pressure, temperature, and velocity, respectively. The EXPLO5 code determines the post detonation properties at steady-state and chemical equilibrium conditions. The transient solutions computed using the developed solver and the solutions of Baer and Nunziato are in a good agreement for P_{cj}, T_{cj}, and D_{cj}, while the P_{cj} and T_{cj} values of steady calculations by EXPLO5 differ. This situation is not surprising, and has been previously addressed in literature [13, 76], with a conclusion that the detonation pressure results of transient calculations may differ $10-20\%$ from the steady, chemical equilibrium calculations, while the detonation velocities may agree to within a few percent. It is also indicated that actual gas temperature values may reach above 10000 K [13]. Since the non-steady nature of the physical problem cannot be captured in steady, chemical equilibrium calculations, the detonation temperature and pressure results obtained by such models are significantly lower than those given by transient calculations. That is, unsteady calculations are capable to capture the real physical processes during DDT phenomenon better than steady calculations.

Table 3.2: Comparison of the results

	Present Study	*EXPLO5* [73, 74, 75]	*Gonthier Powers* [41]
P_{cj}	25.2 *GPa*	18.4 *GPa*	25 *GPa*
T_{cj}	11000 *K*	4370 *K*	10000 *K*
D_{cj}	7480 *m/s*	7318 *m/s*	7500 *m/s*

3.2.3 Reactive solutions : investigation of ignition temperature and particle size

In the calculations performed in this study, ignition of the particles is started with the reach of solid phase temperature (T_p) to a specific value. This specific value is defined as 310 K [41] and this is an *ad hoc* value. In this subsection, the effect of different ignition temperatures on CIT characteristics are investigated. Another important parameter is the initial size (i.e. initial particle diameter, d_{p0}) of the explosive particles. In this subsection, for different initial particle diameters, CIT characteristics investigated. In the calculations, the explosive domain is assumed to be 1 m long with 200 μm explosive particles diameter.

For the ignition temperature investigations, calculations are performed with T_{ign} = 320 and

330 K ignition criteria and compared with the above original results obtained with T_{ign} = 310 K. In Figure 3.16 (a) the CIT determination for T_{ign} = 320 K is given. In the first stage of the process, inert compaction wave propagation is observed of to about 100 μs. At this instant (i.e. at t= 100 μs) ignition of the first particles is observed and therefore, CIT is achieved. Whereas, for T_{ign} = 330 K (Figure 3.16 (b)), inert compaction wave propagation does not cause any ignition in the 1 m long HMX explosive domain. The comparison of the ignition characteristics for these three different ignition temperatures are given in Table 3.3. It may be concluded that the increase of the ignition temperature causes the increase of the time-to-ignition and, therefore, the spatial location of the ignition point moves forward. Whereas if the explosive domain is not sufficiently long, ignition may not be observed in the explosive domain with the increase of the ignition temperature. In our case study, it is observed that for T_{ign} = 330 K, 1 m long explosive domain is not sufficient to observe ignition.
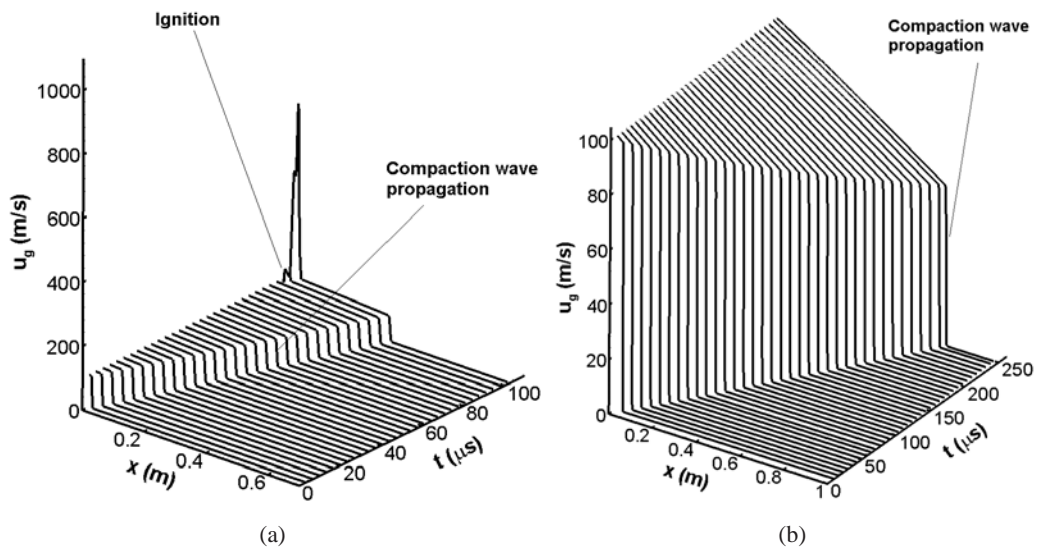
Figure 3.16: Investigation of CIT characteristics for T_{ign} values of; (a) 320 K and, (b) 330 K

Table 3.3: Comparison of the time-to-ignition values for different ignition temperatures

Ignition Temperature (T_{ign})	Time-to-ignition
310K	26 μs
320K	100 μs
330K	No ignition

The results of the calculations for the investigation of different particle sizes on the ignition characteristics are given in Figure 3.17. In these results the time-to-ignition characteristics are

determined for the initial particle diameter (d_{p0}) values 150 and 250 μm and compared with those of original results in Subsection 3.2.2 determined with 200 μm initial particle diameter. The time-to-ignition values for different particle sizes are given in Table 3.4. It is determined that the time-to-ignition value increases with increase of the initial particle diameter.
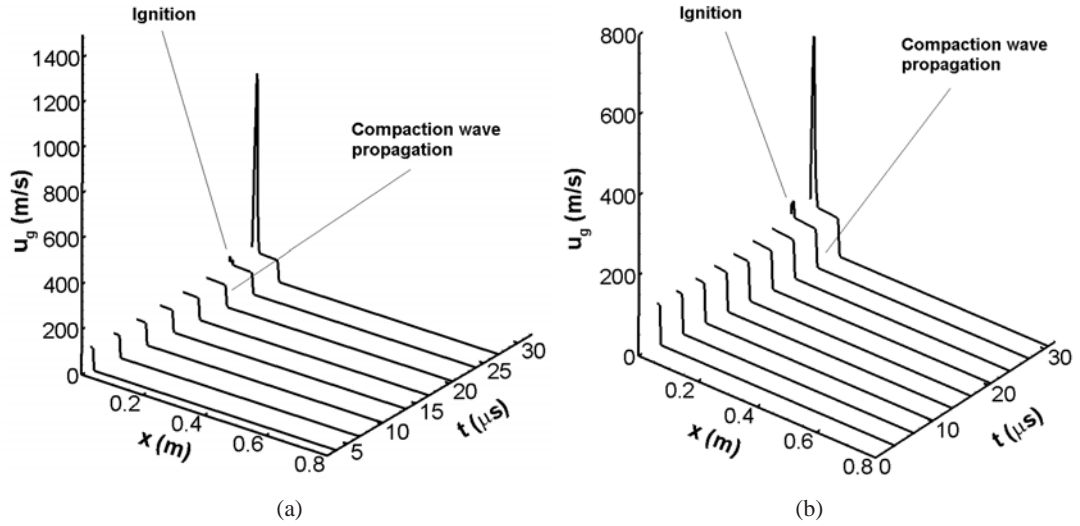
Figure 3.17: Investigation of CIT characteristics for different initial particle diameter (d_{p0}) values of; (a) 150 μm and, (b) 250 μm K

Table 3.4: Comparison of the time-to-ignition values for different initial particle sizes

Initial Particle Diameter (d_{p0})	Time-to-ignition
150 μm	23.5 μs
200 μm	26 μs
250 μm	27.3 μs

3.2.4 Multiple particle size effects: modelling approach

Investigation of different particle sizes on ignition characteristics brings the considerations about the simulation of ignition characteristics if multiple size explosive particles are included in the whole explosive domain. There are some approaches in open literature to model this multiple size modelling [25]. Below some important points of this modelling approach defined by [25] is given.

For the multiple size particle modelling, volume fraction of each particle size is given as follows:

$$\gamma_i = \frac{V_i}{V_{mix}} \tag{3.5}$$

Here V_i denotes the volume occupied for each particle size and, V_{mix} denotes the total volume occupied by gas and solid phases. In this case, the volume fraction of the total solid phase is given as follows:

$$\phi_p = \frac{V_p}{V_{mix}} \tag{3.6}$$

Here $V_p = \sum_i V_i$. The volume fraction of the total solid phase is given as;

$$\phi_p = \sum_i \gamma_i \tag{3.7}$$

Following these definitions, continuity, momentum and energy conservation equations for each particle sizes are described [25]:

$$\frac{\partial(\gamma_i \rho_{pi})}{\partial t} + \frac{\partial(\gamma_i \rho_{pi} u_{pi})}{\partial x} = S_{cont}$$

$$\frac{\partial(\gamma_i \rho_{pi} u_{pi})}{\partial t} + \frac{\partial(\gamma_i \rho_{pi} u_{pi}^2 + \gamma_i p_{pi})}{\partial x} = S_{mom} \tag{3.8}$$

$$\frac{\partial(\gamma_i \rho_{pi} E_{pi})}{\partial t} + \frac{\partial(\gamma_i \rho_{pi} E_{pi} u_{pi} + \gamma_i p_{pi} u_{pi})}{\partial x} = S_{en}$$

In the same manner, interphase drag and heat transfer relations for each particle size may be defined as $D = \sum_i D_i$ and $\dot{Q} = \sum_i \dot{Q}_i$.

CHAPTER 4

TWO-DIMENSIONAL MATHEMATICAL AND NUMERICAL MODEL

This chapter describes the extension of the one-dimensional model to two dimensions. Mainly, one-dimensional momentum transfers due to the gas generation rate and the interphase drag interaction are extended to include the two-dimensional effects.

4.1 Two dimensional mathematical model

In Chapter 2 and 3, the basic features of ignition delay, ignition, deflagration and transition to detonation are investigated under the assumption of one-dimensional physics. However, deflagration and detonation waves in complex geometries appear to be significantly influenced by multidimensional effects. For this reason, the one dimensional mathematical model and the corresponding numerical algorithms are extended to two dimensions in order to capture the multidimensional effects. Each phase is assumed to exist simultaneously on every spatial location as assumed in the one dimensional case.

The mathematical model is given below:

Gas Phase Equations

$$\frac{\partial(\phi_g\rho_g)}{\partial t} + \frac{\partial(\phi_g\rho_g u_g)}{\partial x} + \frac{\partial(\phi_g\rho_g v_g)}{\partial y} = \Gamma_g \tag{4.1}$$

$$\frac{\partial(\phi_g\rho_g u_g)}{\partial t} + \frac{\partial(\phi_g\rho_g u_g^2 + \phi_g p_g)}{\partial x} + \frac{\partial(\phi_g\rho_g u_g v_g)}{\partial y} = \Gamma_g u_p - D_x \tag{4.2}$$

$$\frac{\partial(\phi_g\rho_g v_g)}{\partial t} + \frac{\partial(\phi_g\rho_g u_g v_g)}{\partial x} + \frac{\partial(\phi_g\rho_g v_g^2 + \phi_g p_g)}{\partial y} = \Gamma_g v_p - D_y \tag{4.3}$$

$$\frac{\partial(\phi_g\rho_g E_g)}{\partial t} + \frac{\partial(\phi_g\rho_g E_g u_g + \phi_g p_g u_g)}{\partial x} + \frac{\partial(\phi_g\rho_g E_g v_g + \phi_g p_g v_g)}{\partial y}$$
$$= \Gamma_g E_p - \dot{Q} - D_x u_p - D_y v_p \tag{4.4}$$

Solid Phase Equations

$$\frac{\partial(\phi_p\rho_p)}{\partial t} + \frac{\partial(\phi_p\rho_p u_p)}{\partial x} + \frac{\partial(\phi_p\rho_p v_p)}{\partial y} = -\Gamma_g \tag{4.5}$$

$$\frac{\partial(\phi_p\rho_p u_p)}{\partial t} + \frac{\partial(\phi_p\rho_p u_p^2 + \phi_p p_p)}{\partial x} + \frac{\partial(\phi_p\rho_p u_p v_p)}{\partial y} = -\Gamma_g u_p + D_x \tag{4.6}$$

$$\frac{\partial(\phi_p\rho_p v_p)}{\partial t} + \frac{\partial(\phi_p\rho_p u_p v_p)}{\partial x} + \frac{\partial(\phi_p\rho_p v_p^2 + \phi_p p_p)}{\partial y} = -\Gamma_g v_p + D_y \tag{4.7}$$

$$\frac{\partial(\phi_p\rho_p E_p)}{\partial t} + \frac{\partial(\phi_p\rho_p E_p u_p + \phi_p p_p u_p)}{\partial x} + \frac{\partial(\phi_p\rho_p E_p v_p + \phi_p p_p v_p)}{\partial y}$$
$$= -\Gamma_g E_p + \dot{Q} + D_x u_p + D_y v_p \tag{4.8}$$

$$\frac{\partial(\rho_p)}{\partial t} + \frac{\partial(\rho_p u_p)}{\partial x} + \frac{\partial(\rho_p v_p)}{\partial y} = -\frac{\rho_p \phi_g}{\mu_c}\left(p_p - p_e - p_g\right) \tag{4.9}$$

$$\frac{\partial n}{\partial t} + \frac{\partial n u_p}{\partial x} + \frac{\partial n v_p}{\partial y} = 0 \tag{4.10}$$

Unlike the one-dimensional model, the source terms in momentum and energy conservation equations (momentum and energy transfers due to gas generation rate) include the effects of solid-phase transverse velocity, v_p. Besides, interphase drag interaction term is extended to second dimension using the gas-phase and solid-phase transverse velocities, v_g and v_p:

Interphase Drag Interaction Terms

$$D_x = f_{pg}\left(u_g - u_p\right) \tag{4.11}$$

$$D_y = f_{pg}\left(v_g - v_p\right) \tag{4.12}$$

Some similar approaches to extend the one-dimensional DDT models are also given in open literature [33, 39]. However, in most two-dimensional modelling applications, interphase drag and heat transfer interaction terms are ignored, and momentum and energy equations are described as a single equation for each employing some reductions [38, 39]. The main contribution of this study is the application of two-dimensional extension to the complete two-phase model. In this study, interphase drag, momentum and energy transfers due to burning of explosive particles are defined in two-dimensional form, unlike the other two-dimensional models in literature.

4.2 Numerical method

The numerical algorithm is based on central-differences on structured curvilinear grids. In Figure 4.1, the schematic representation of a typical grid system using the O-grid topology is shown.
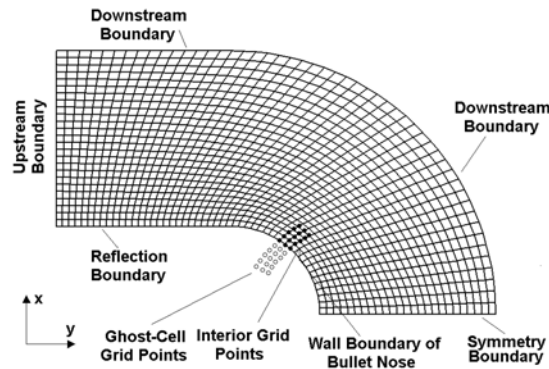
Figure 4.1: A typical grid system generated for bullet impact problem (in O-grid topology)

Ghost-cells (ghost-cell points) are defined beyond boundaries for implementing boundary conditions. The values of variables on the ghost cell points are determined using proper definitions of the boundary conditions.

4.2.1 Generalized coordinates

Governing equations in the Cartesian coordinate system in (x, y) are transformed to generalized coordinates $(\xi = \xi(x, y), \eta = \eta(x, y))$ to be used for body-fitted grids:

$$\frac{\partial}{\partial t}\left(\frac{\vec{U}}{J}\right) + \frac{\partial}{\partial \xi}\left(\frac{\xi_x\vec{F} + \xi_y\vec{G}}{J}\right) + \frac{\partial}{\partial \eta}\left(\frac{\eta_x\vec{F} + \eta_y\vec{G}}{J}\right) = \frac{\vec{S}}{J} \qquad (4.13)$$

4.2.2 Symmetry/Reflection boundary conditions

As seen from Figure 4.1, all flow variables at ghost points are extrapolated from interior points in order to apply the symmetry or reflection boundary conditions. It should be noted that the sign of the vertical velocities are reversed.

$$u\rangle_{0,...,-4} = u\rangle_{1,...,5}$$
$$v\rangle_{0,...,-4} = -v\rangle_{1,...,5}$$
$$\rho\rangle_{0,...,-4} = \rho\rangle_{1,...,5} \qquad (4.14)$$
$$p\rangle_{0,...,-4} = p\rangle_{1,...,5}$$

Here subscripts *0,...,-4* denote the ghost points and, *1,...,5* denote the interior grid points.

4.2.3 Downstream/Upstream boundary conditions

For downstream boundary conditions, the flow variables on the ghost cell points are also determined using the values on the interior grid points(Figure 4.1).

$$u\rangle_{0,...,-4} = u\rangle_{1,...,5}$$
$$v\rangle_{0,...,-4} = v\rangle_{1,...,5}$$
$$\rho\rangle_{0,...,-4} = \rho\rangle_{1,...,5} \qquad (4.15)$$
$$p\rangle_{0,...,-4} = p\rangle_{1,...,5}$$

Subscripts *0,...,-4* denote again the ghost points and, *1,...,5* denote the interior grid points.

4.2.4   Piston wall boundary condition

In the bullet-impact type problems considered in this study, impact boundaries are assumed to be located on left of the domain(Figure 4.1).
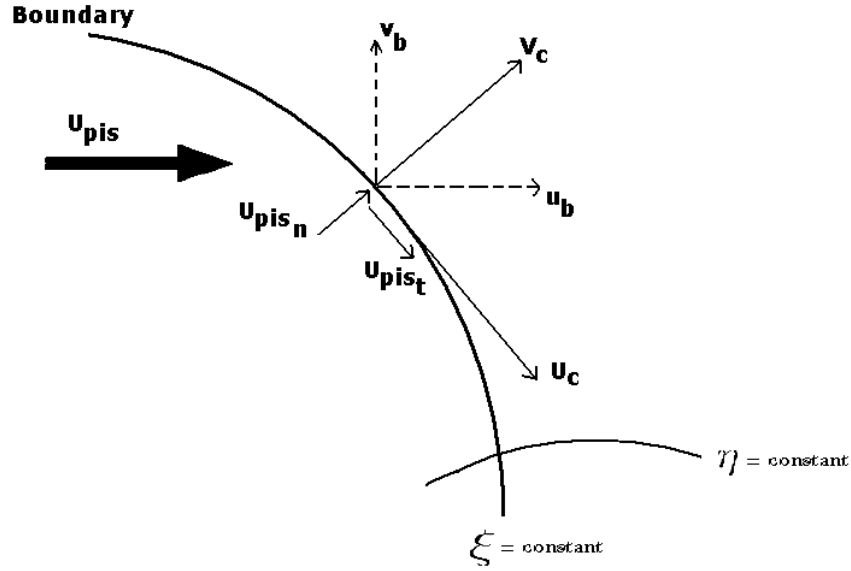
Figure 4.2: Schematic representation of contravariant and piston velocity components on curved boundary

The variables are updated using Equation 4.15 along the left boundary except the impact locations. In order to determine the ghost point velocities for the impact boundary, contravariant velocities (Figure 4.2) in the boundary vicinity are required.

$$U_c = u\xi_x + v\xi_y$$
$$V_c = u\eta_x + v\eta_y \tag{4.16}$$

Contravariant velocity at $i = 0$ ghost point is determined as follows:

$$U_c)_{i=0} = 2U_{pis}\xi_x - U_c)_{i=1} \tag{4.17}$$

For inviscid calculations

$$V_c)_{i=0} = V_c)_{i=1} \tag{4.18}$$

For viscous calculations

$$V_c)_{i=0} = U_{pis}\eta_x \tag{4.19}$$

In these equations $i = 1$ denotes the boundary and, $i = 0$ denotes the first ghost cell point. Velocity components on the ghost point(u_0 and v_0) are then determined as follows:

$$u_0 = \frac{U_c\rangle_{i=0}\eta_y - V_c\rangle_{i=0}\xi_y}{\xi_x\eta_y - \eta_x\xi_y} \tag{4.20}$$

$$v_0 = \frac{-U_c\rangle_{i=0}\eta_x + V_c\rangle_{i=0}\xi_x}{\xi_x\eta_y - \eta_x\xi_y} \tag{4.21}$$

Once the boundary velocity components at $i = 0$ ghost point are evaluated, other variables are determined using first-order extrapolation from interior grid points. The values on the other ghost points (i.e. $i = -1, -2, -3, -4$) are evaluated in the same manner. This definition of the wall boundary condition may be applied for any type of problems by setting $U_{pis} = 0$, such as subsonic flow over a cylinder.

4.3 Parallel Processing

Scientific computing in a parallel environment aims at dividing a large computing task into smaller independent tasks to execute them simultaneously. The flow-chart in Figure 4.3 illustrates the parallel solution of a problem with distributed-memory approach. The execution of these sub-tasks in parallel is expected to last shorter than a sequential execution in serial.

Below is the list of means to enable parallel programming in computers [77]:

- *Library Routines*: A set of library functions is used to support the parallelism and the communication between the processors. Examples of such libraries include MPI and PVM message passing libraries.

- *New Constructs*: The programming language is extended with some new constructs to support the parallelism. An example is the aggregated array operations in Fortran 90.

- *Compiler Directives*: The programming language stays the same, but formatted comments, called compiler directives are added.

The library approach is widely used since it is easy to implement. In this approach, the parallel execution of the sub-tasks and the interaction between the processes are provided by a set of

```
                    ┌──────────────┐
                    │   PROBLEM    │
                    └──────────────┘
      ┌──────────────────┼──────────────────────┐
┌──────────────┐  ┌──────────────┐        ┌──────────────┐
│ Sub–Problem 1│  │ Sub–Problem 2│  ...   │ Sub–Problem n│
│ in processor 1│  │ in processor 2│        │ in processor n│
└──────────────┘  └──────────────┘        └──────────────┘
       │                  │                       │
┌──────────────┐  ┌──────────────┐        ┌──────────────┐
│ Sub–Result 1 │  │ Sub–Result 2 │        │ Sub–Result n │
└──────────────┘  └──────────────┘        └──────────────┘
       └──────────────────┼──────────────────────┘
                    ┌──────────────┐
                    │   RESULT     │
                    └──────────────┘
```
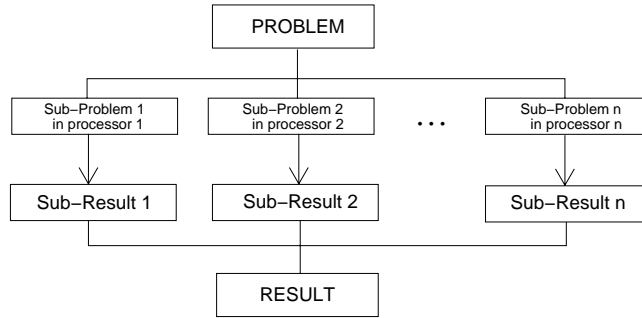
Figure 4.3: Parallel solution of a problem with distributed-memory approach [78]

library routines linked to the code written in C or Fortran, etc. Hence, there is no need for a new compiler.

In this study, MPI message passing library routines for the Fortran language are used in parallel programming. MPI message passing library is recently developed, and considered to be the standard parallel programming tool. The version of MPI library used in this study is 1.2.7p1.

4.3.1 Parallel Programming

The available parallel computing environment is a distributed-memory system. On this parallel system, each processor has its own memory and solves a sub-problem with its own private data. The solver used in this study is developed according to this concept in the form of domain decomposition parallel processing topology. In code parallelization based on domain decomposition, there are two performance and efficiency related definitions which are load balancing and speed-up, explained below.

4.3.1.1 Domain Decomposition

A brief definition for the domain decomposition may be made as data and computational task partitioning among multiple processors. A computational domain given as an input to the developed solver, which is a O-type or H-type grid, is decomposed into its subgrids first, and the solution on each subgrid is assigned to a processor. An example of domain decomposition

64
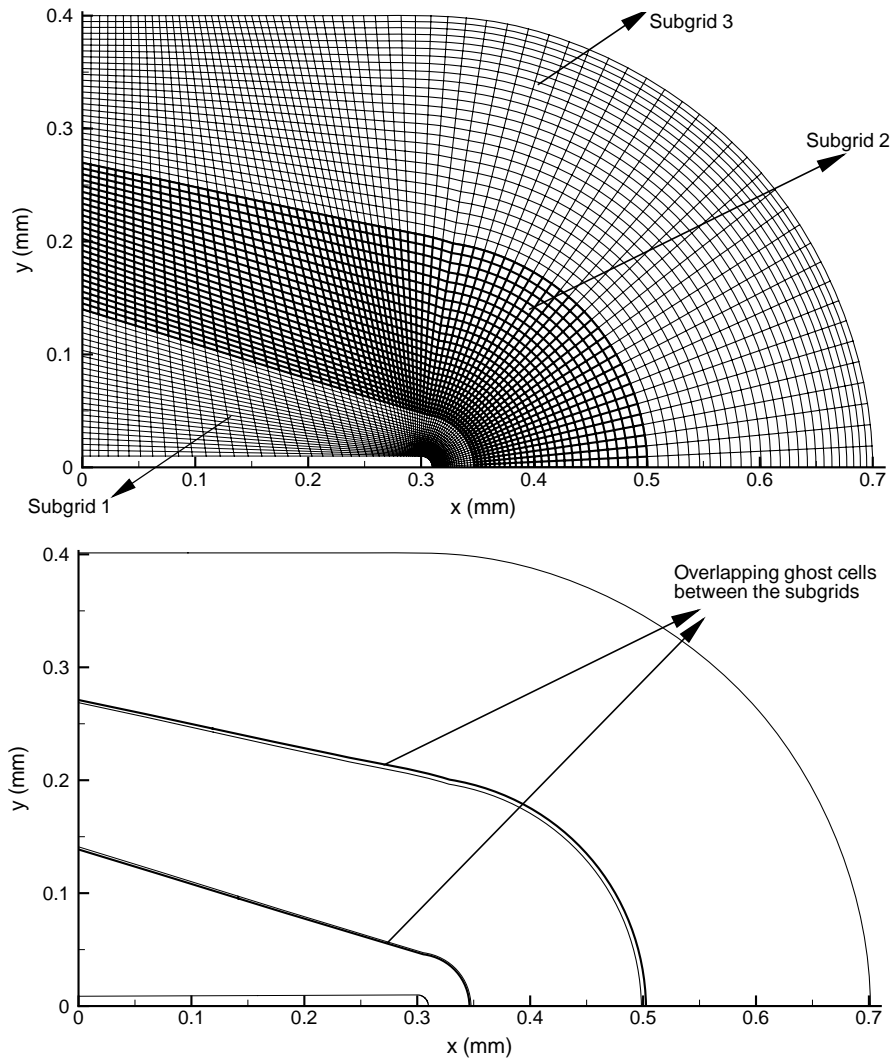
Figure 4.4: Domain decomposition for parallel processing

among the cases studied is given in Figure 4.4.

4.3.1.2 Load Balancing

Uniform computational activity on each processor is an important issue to minimize the wait/waste time of a process which should catch up with another process. Maintaining uniformity on each processor is called as *load balancing*. In the developed solver, the grid is partitioned in such a way that each process deals with almost the same number of grid nodes for a proper load balancing.

4.3.2 Speed-Up

Another parallel processing performance criteria is *speed-up* which measures how fast the parallel code is, compared to its serial counterpart. A good parallel coding algorithm is one for which the ratio in Equation 4.22 is larger. In Figure 4.5, the speed-up characteristics of the parallel processing algorithm facilitated with the solver developed in this study.

$$\mathrm{S}peed\text{--}Up = \frac{CPU\ time\ for\ 1\ serial\ processor}{CPU\ time\ for\ n\ processors\ in\ parallel} \tag{4.22}$$
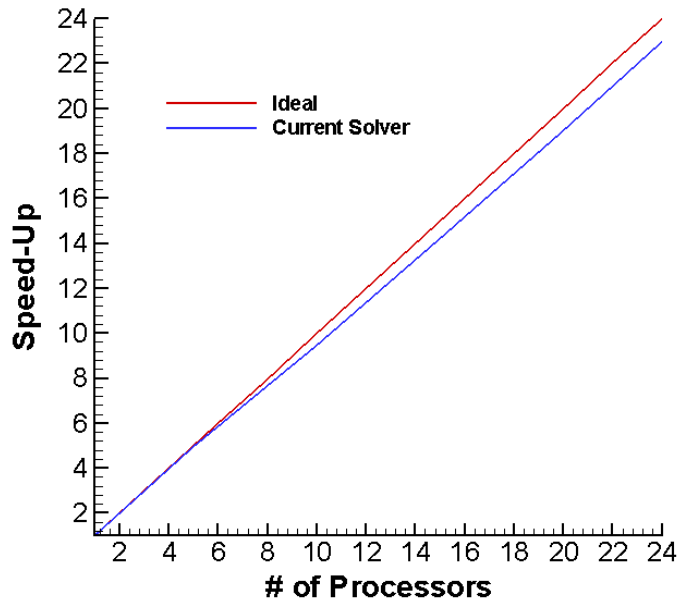
Figure 4.5: Speed-up characteristics

4.3.3 Computing Environment

The computer cluster available for parallel processing consists of 12 rack-type computers with dual-core 2.2 GHz AMD Opteron processors and 2048 MB memory for each processor. Hence, there are a total of 24 processors with 48 GB memory in the cluster. The communication between the processors is provided by a 1 Gbps-ethernet switch. The computers run under the 64-bit Rocks 4.2.1 operating system based on CentOs Linux. The fortran compiler used is 64-bit Intel Fortran Compiler version 10.1 which supports hyperthreading technology provided by the processors in the cluster.

4.3.4 Parallel Algorithm

The parallel algorithm implemented in the developed solver is based on the domain decomposition approach. Various flow and detonation conditions are computed using O-type and H-type grids. Before the computation starts, the grid is partitioned into physically non-overlapping subgrids first (Figure 4.4), and the solution on each subgrid is computed as a separate process in the computer cluster. The subgrids are physically non-overlapping but the ghost cells of a subgrid geometrically overlap the neighboring subgrid. The multi-phase flow variables on the overlapping ghost cells are exchanged among the subgrid processes at each time step of the unsteady solution.

CHAPTER 5

TWO DIMENSIONAL RESULTS

In this chapter, two-dimensional case studies are performed. As aforementioned, the main aim of the thesis is to investigate the hazard as well as sensitivity characteristics of explosives including munitions systems. Developed solver is also used for optimal munitions design investigations. An inert two-dimensional problem is first solved to verify the two-dimensional code. For insensitivity investigations, sharp and blunt-nosed projectile impact problems are considered. Wave-shaper problems for shaped-charge systems are chosen for optimal munitions design investigations. The details of the problems are described in the following sections.

5.1   Code validation

For the validation of developed two-dimensional solver, a special shock-tube problem is selected as depicted in Figure 5.1. The non-planar wall in the shock-tube is similar to wave-shapers in shaped-charge munitions. Therefore, this inert validation study is very useful in understanding the boundary condition implementation on the wave-shapers. The details of wave-shaper in munitions system are given in Section 5.3.

The same problem is also solved using AutoDYN, a commercial, explicit Euler and Lagrange solvers to compare the results of the present study. For the calculations with AutoDYN, Eulerian upwind solver, which is 2nd order accurate both in time and spatial domain is used. The states in the left (denoted l) and right (denoted r) sides in the shock-tube are set to the values given in Section 3.1 to match the conditions of the Sod-case shock-tube problem.

The diaphragm in the tube is assumed to rapture suddenly at $t = 0$ s. The computed pressure field at $t_{final} = 2x10^{-5}$ s after the diaphragm rupture is given in Figures 5.2 and 5.3. The comparison of pressure profiles along the lower wall obtained using the developed solver and AutoDYN is given in Figure 5.4. It is seen from the figures that, there is a good agreement between both solutions.
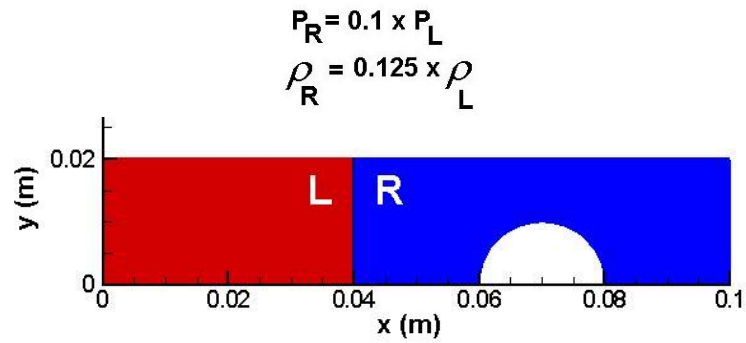
Figure 5.1: Shock-tube with circular obstacle problem
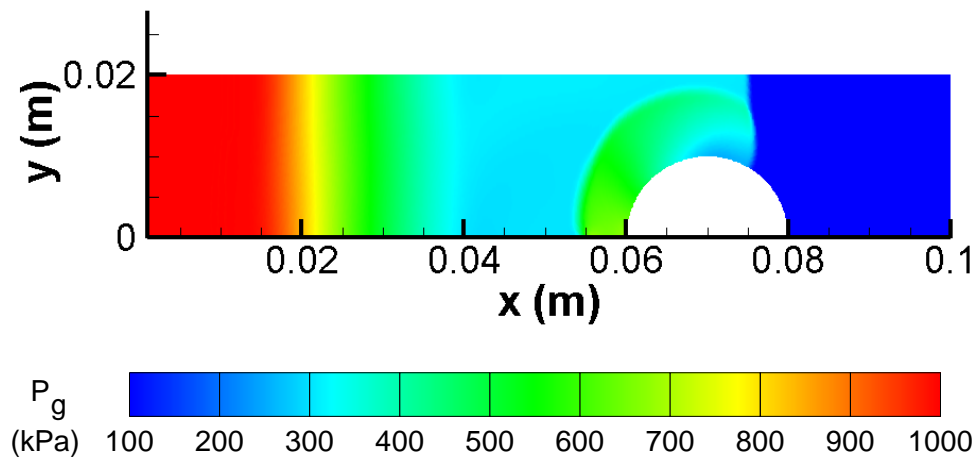
Figure 5.2: Solution of shock-tube with circular obstacle problem $t_{final} = 2x10^{-5}s$)
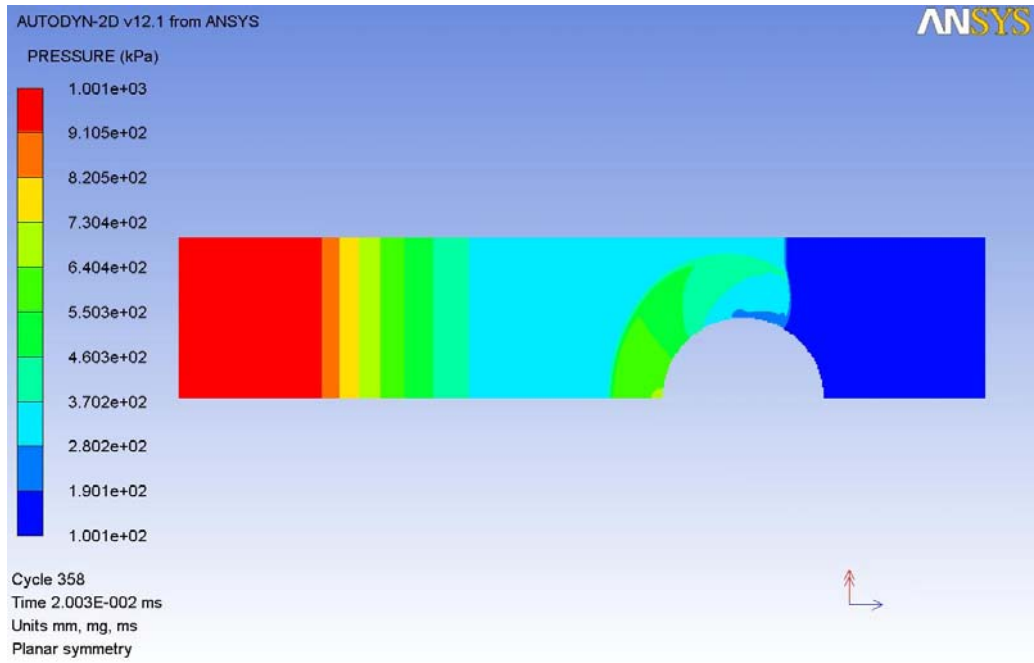
Figure 5.3: Solution of shock-tube with circular obstacle problem with AutoDYN ($t_{final} = 2x10^{-5}s$)
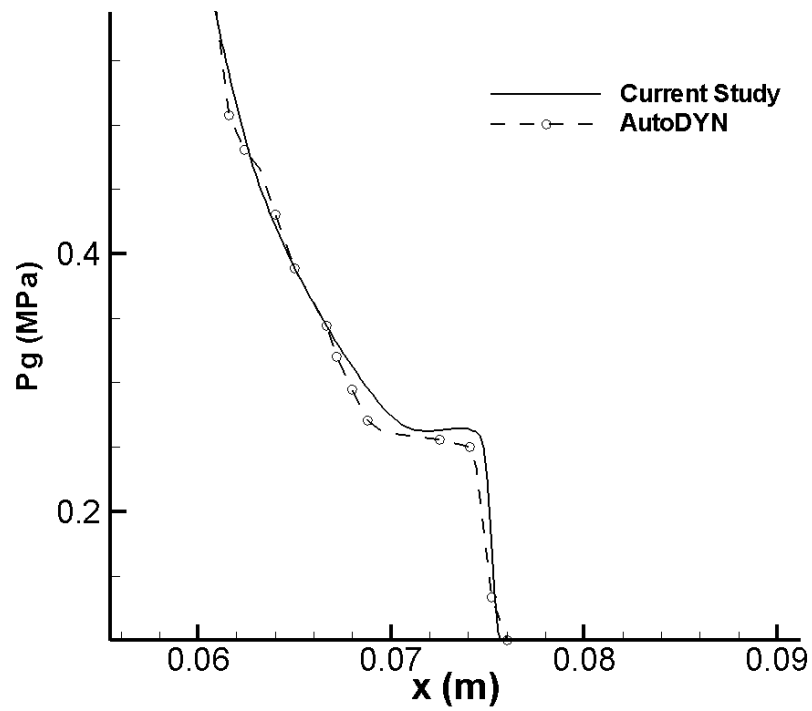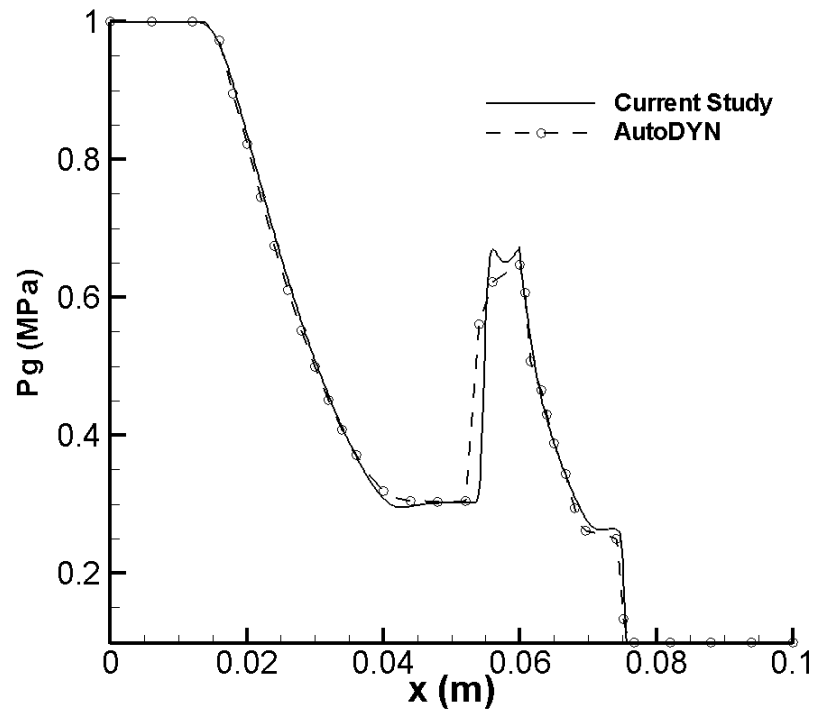
Figure 5.4: Comparison of pressure profiles on lower wall for shock-tube with circular obstacle problem

5.2 Blunt and sharp-nosed projectile impact problems

In this section, the developed solver is used to investigate the effect of the blunt-nosed and sharp-nosed projectile impact situations on ignition characteristics of an HMX explosive bed. The main goal of these studies is the determination of sensitivity of a typical explosive bed to some specific impact velocities. In the calculations it is assumed that upon its strike the projectile somewhat penetrates into the explosive and the compaction starts immediately. It is also assumed that the penetration process is much slower than the compaction process. Therefore, the projectile surface is formed in the explosive and frozen during the numerical integration.

5.2.1 Blunt-nosed projectile impact problem

Blunt-nosed projectile impact situation is illustrated in Figure 5.5. To avoid the possible reflection effects from upstream boundary during numerical integration, the projectile nose is located $0.3m$ away from the boundary.
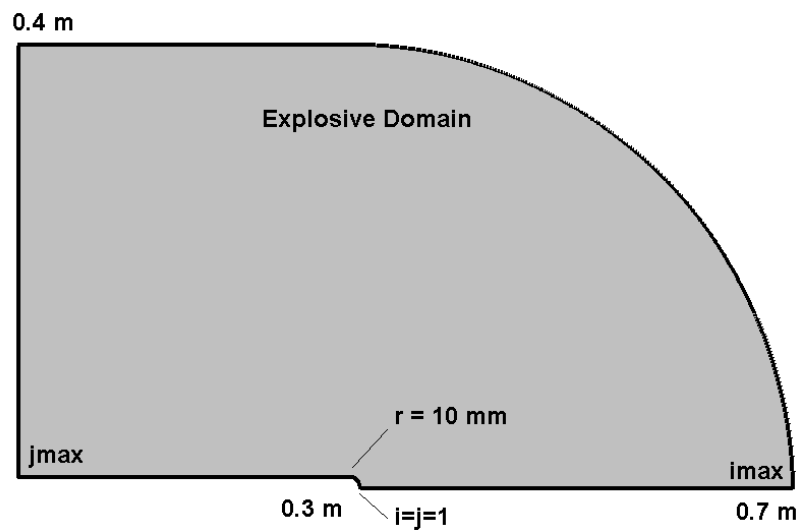
Figure 5.5: Physical demonstration of blunt-nosed projectile impact situation

For the numerical simulation of this problem, an O-grid is generated over the body. Center of the projectile nose is located at 0.3 m. Explosive domain is assumed to extend up to 0.7 m. For this case 1501x1501 grid resolution is used (Figure 5.6). In Subsection 3.2.2 it is stated that the grid-independent results are obtained with $\Delta x = 1/2000 = 5 x 10^{-4} m$ grid resolution. In this two dimensional calculations maximum grid resolution is set to be about $\Delta x = 4.6 x 10^{-4} m$ which is well below the one dimensional solution's grid resolution.

The piston boundary condition is applied for three velocity values, which are 100, 150 and 50 m/s. In Figures 5.7, 5.8, 5.9 and 5.10, the instantaneous fields obtained at t = 3 to 18.5 μs time values for the gas-phase pressure, gas-phase density, solid-phase volume fraction and gas-phase temperature profiles for the 100 m/s impact situation are given, respectively.

(a)

(b)
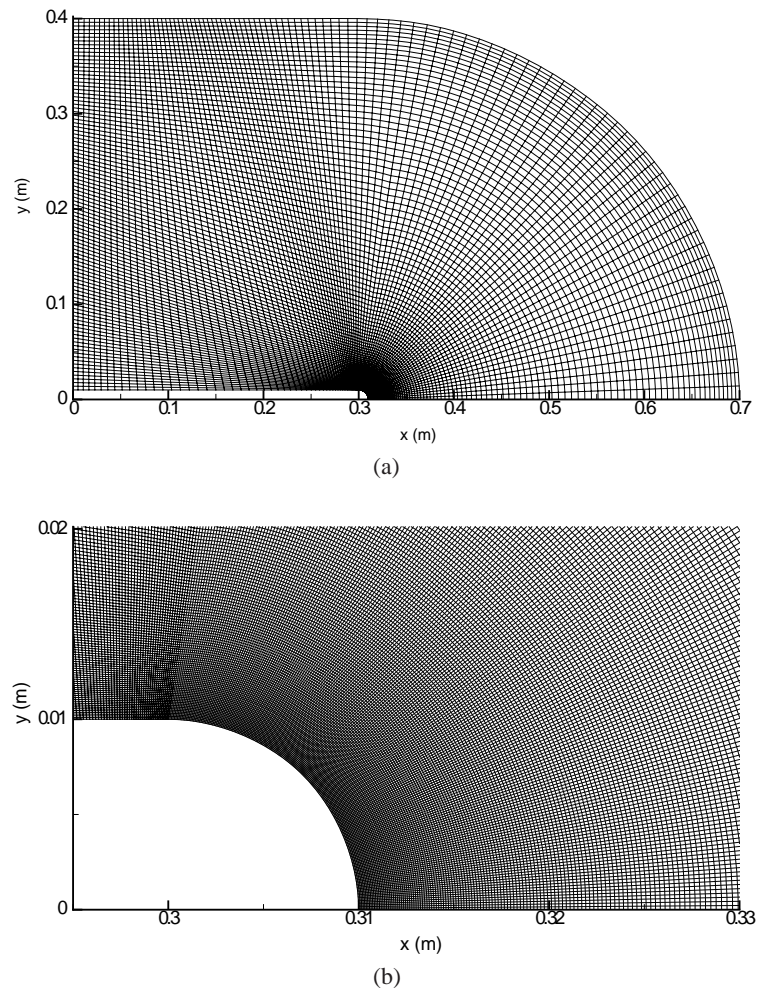
Figure 5.6: Solution grid for blunt-nosed projectile impact situation (a) full-scale view with every 15 points shown, (b) zoomed view with every 3 points shown

The Figures 5.7 (a) and (b) show the formation and the propagation of the compaction wave around the curved part of the projectile nose in the very beginning of the process. It is observed in Figures 5.7 (a) and 5.11 that the gas-phase pressure is increased to about 30 MPa from its ambient value of 2.57 MPa. The formation and propagation of the compaction wave causes the ignition of the explosive particles and at this stage, slow-rate combustion is observed. In the very beginning of this process, gas-phase pressure increases from 30 MPa to about 350 MPa (Figures 5.7 (b) and 5.11 (b))while gas-phase density increases from about 20 kg/m^3 to about 230 kg/m^3 (Figure 5.8 (b)) and solid-phase volume fraction decreases from ambient value of 0.73 to about 0.68 (Figure 5.9 (b)). The ignition of the first few particles in this region around the projectile causes the increase in temperature, pressure and density as mentioned. Therefore, this region is defined as the high pressure and temperature region and, in following parts of the text this definition is used repeatedly. The formation of the high pressure and temperature region is also explained in Subsection 1.1.2. It is mentioned that at the very beginning of the DDT phenomenon, the conduction mechanism is dominant and neighboring particles in the domain is ignited by this manner and in this step, burn-rates are relatively low. During this conduction-initiation of particles, pressure, temperature and, density increases and a high pressure and temperature region forms in the domain at slower burn rate.
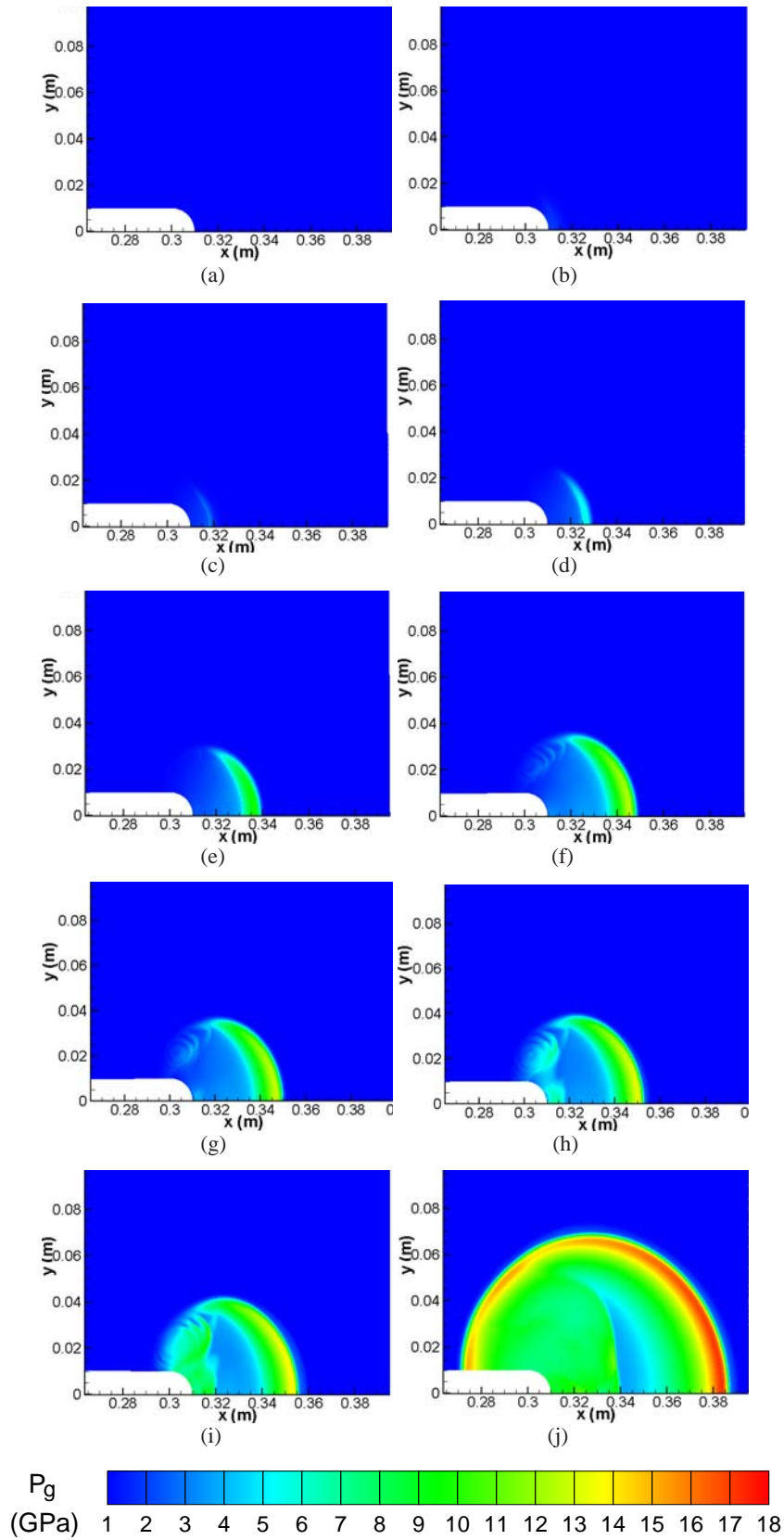
Figure 5.7: Evolution of gas-phase pressure profiles for the blunt-nosed projectile impact case of 100 m/s with $r = 10$ mm cone radius for (a) 3, (b) 5, (c) 6.6, (d) 8.8, (e) 11, (f) 12.7, (g) 13, (h) 13.5, (i) 14, (j) 18.5 μs

75
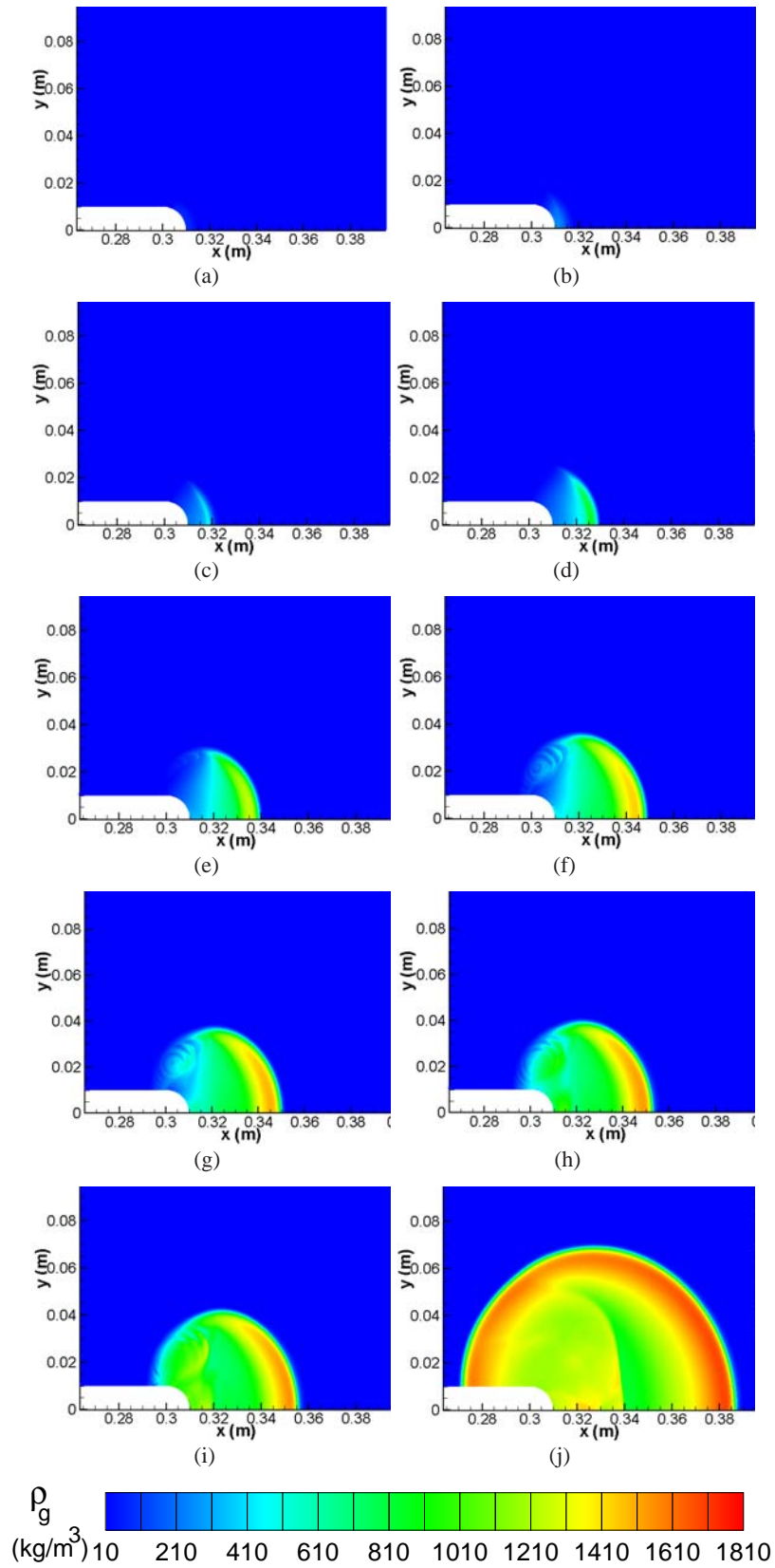
Figure 5.8: Evolution of gas-phase density profiles for blunt-nosed projectile impact case of 100 m/s with $r = 10$ mm cone radius for (a) 3, (b) 5, (c) 6.6, (d) 8.8, (e) 11, (f) 12.7, (g) 13, (h) 13.5 ,(i) 14, (j) 18.5 μs
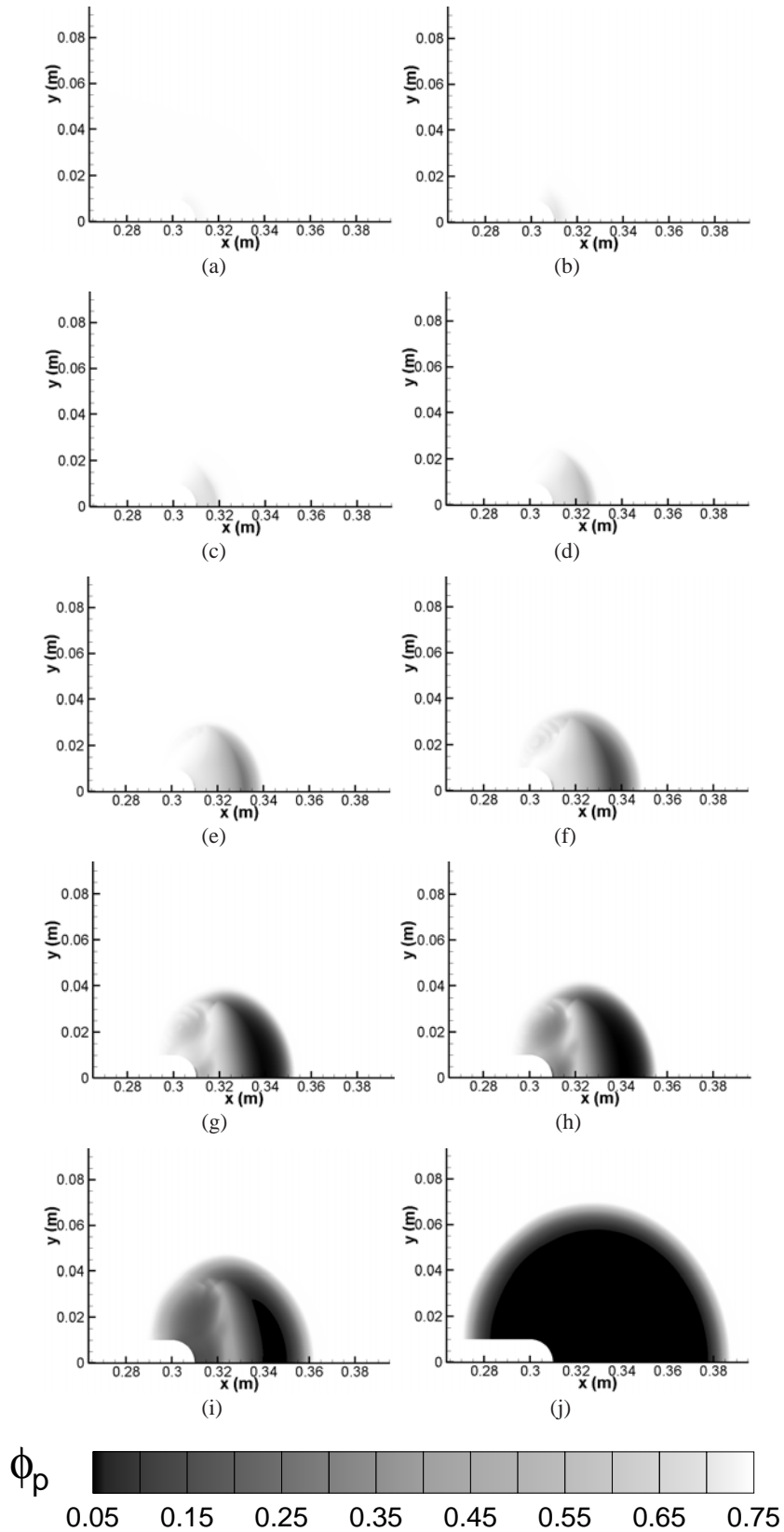
Figure 5.9: Evolution of solid-phase volume fraction for blunt-nosed projectile impact case of 100 m/s with $r = 10$ mm cone radius for (a) 3, (b) 5, (c) 6.6, (d) 8.8, (e) 11, (f) 12.7, (g) 13, (h) 13.5 ,(i) 14, (j) 18.5 μs

77
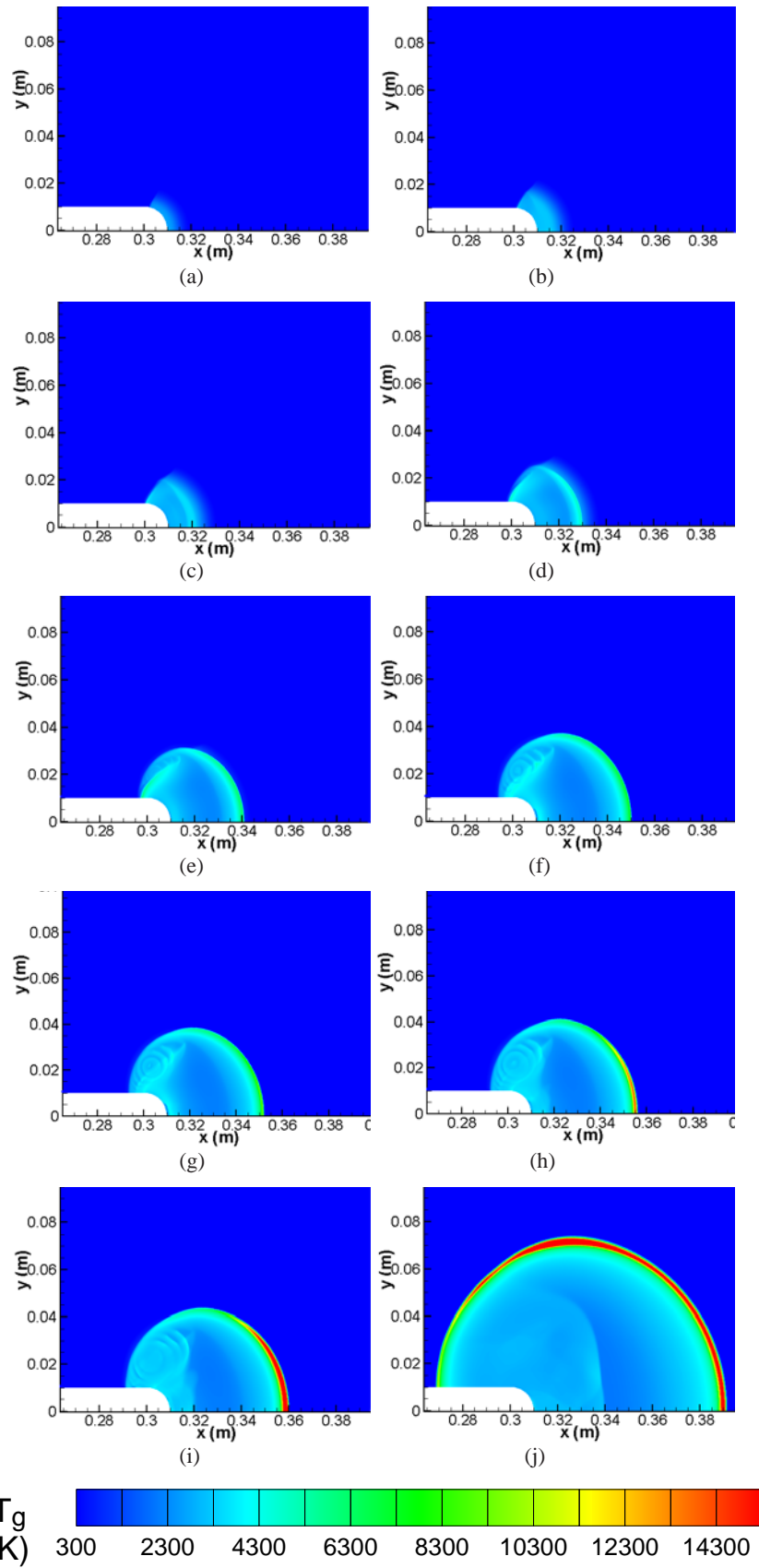
Figure 5.10: Evolution of gas-phase temperature contours for blunt-nosed projectile impact case of 100 m/s with r = 10 mm cone radius for (a) 3, (b) 5, (c) 6.6, (d) 8.8, (e) 11, (f) 12.7, (g) 13, (h) 13.5 ,(i) 14, (j) 18.5 μs
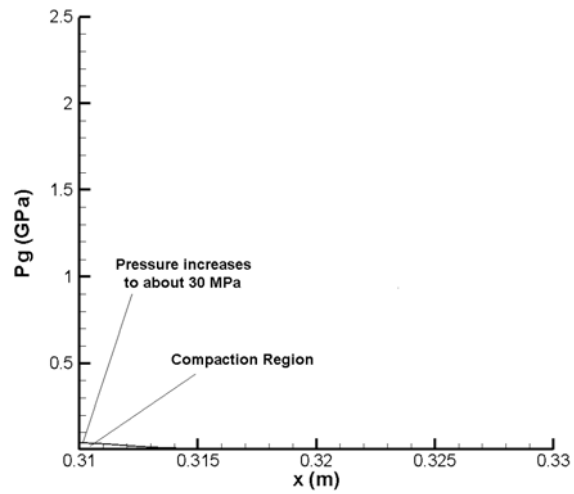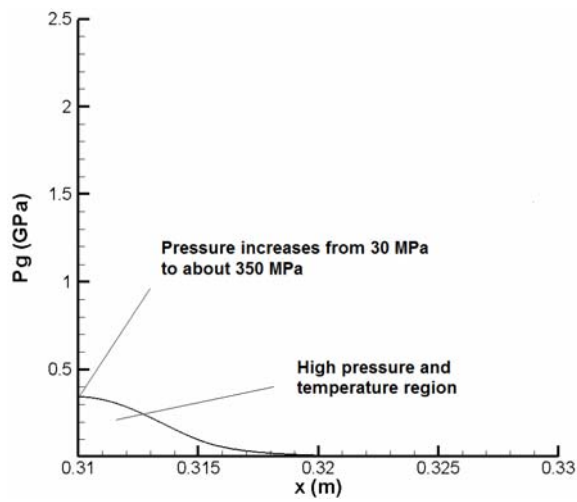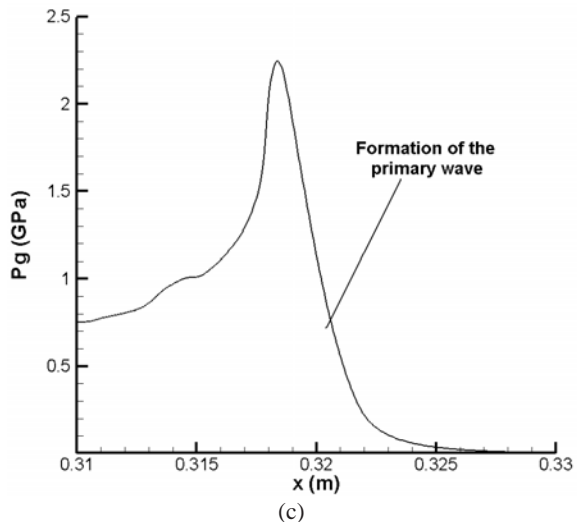
Figure 5.11: Formation of (a) compaction region (3 μs), (b) high pressure and temperature region and (6.6 μs), (c) formation of the primary wave (8.8 μs) for the blunt-nosed projectile impact case of 100 m/s with $r = 10$ mm cone radius (extracted from the $y = 0$ symmetry axis)

After the ignition of the particles and, formation of the high pressure and temperature region, second stage of the process starts with the ignition of more particles in the domain as depicted in Figure 5.12. In this second stage the generated combustion gases with the ignition of the particles penetrate through the porous structure of the explosive bed to preheat the explosive particles in downstream of the domain. This preheating effect improves the ignition sensitivity of the particles and therefore, reaction rates increase in this stage. With the increase of the burn rate, a deflagration wave front forms in the domain. This wave front is defined as the primary wave in this study. Formation of this primary wave is shown in Figures 5.7 (c), 5.8 (c), 5.9 (c) and, 5.11 (c). The formation of the primary wave leads to an increase in the gas-phase pressure from 350 MPa to about 2 GPa (Figure 5.11 (c)).
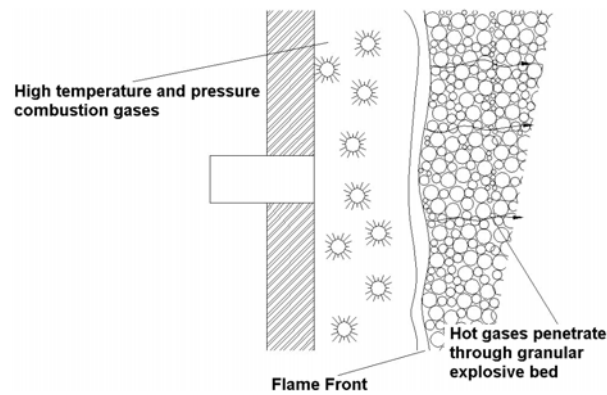
Figure 5.12: Formation of the primary wave and the flame spreading phenomenon (Figure 1.7 repeated)

After the formation of the primary wave, a secondary wave formation is observed on the projectile body. In the high pressure and temperature, following the formation of the primary wave, backward wave propagation takes place. This situation is clearly shown in gas density profiles given in Figures 5.8 (d), (e), (f) and 5.13. With the hit of this backward wave to the projectile body, secondary wave formation is observed (Figure 5.13 (c)). The secondary wave formation phenomenon is also illustrated in Figure 5.14, which show the line plots of gas-phase pressure profiles and solid volume fraction profiles extracted from the $y = 0$ symmetry axis, respectively. In Figure 5.14 (a), the propagation of deflagration wave remaining a high pressure and temperature region behind is shown. While the deflagration wave (primary wave) propagates, a secondary wave forms around the projectile nose as explained above (Figure 5.14 (b)). Here in front of the primary wave, solid-phase volume fraction (ϕ_p) value is in the ambient value of 0.73 and, in the vicinity of the combustion zone behind the primary wave, this value decreases due to burning of the particles.
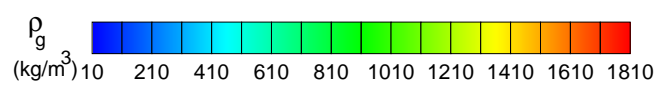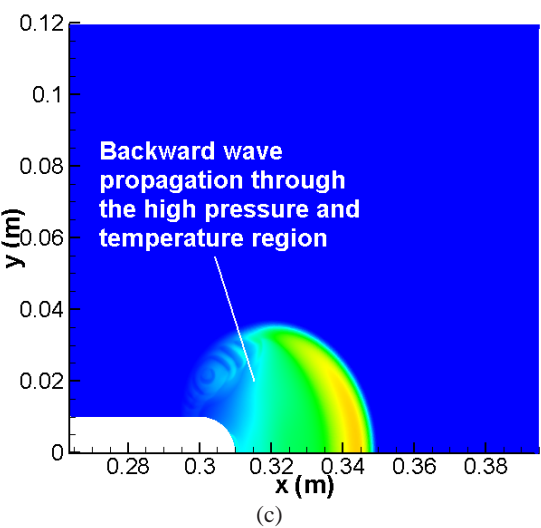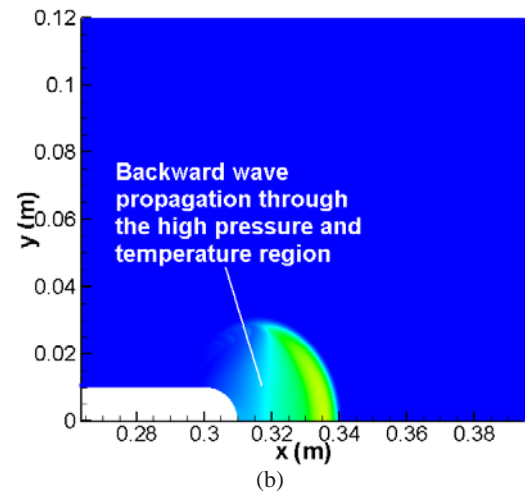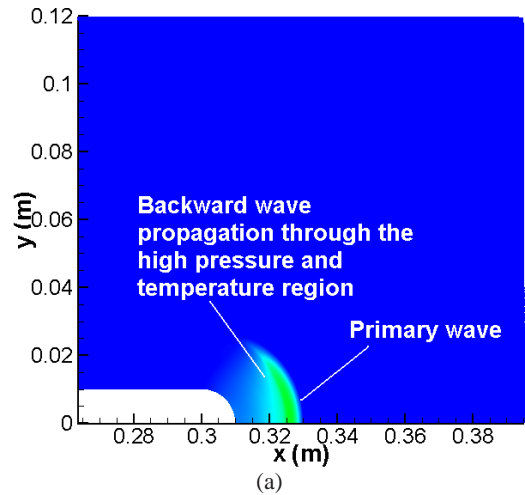
Figure 5.13: Gas-density profiles for the illustration of the formation of the secondary wave on the projectile body with the effect of backward wave propagation after the formation of the primary wave for (a) 8.8, (b) 11, (c) 12.7 μs for blunt-nosed projectile impact case of 100 m/s with $r = 10$ mm cone radius
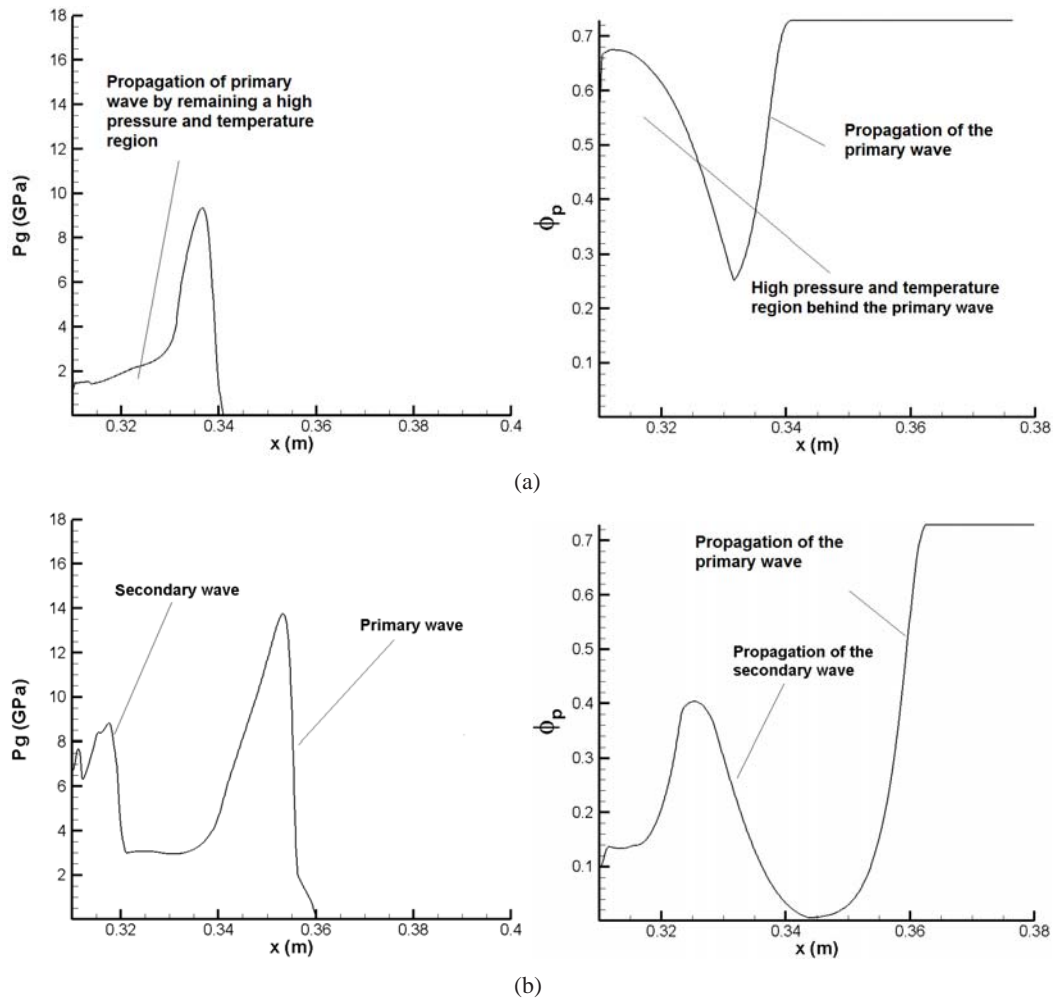
Figure 5.14: (a) Propagation of deflagration wave-front by remaining a high pressure and temperature region behind (t=11 μs), (b) formation of secondary wave (t=12.7 μs) for blunt-nosed projectile impact case of 100 m/s with $r = 10$ mm cone radius (extracted from the $y = 0$ symmetry axis)
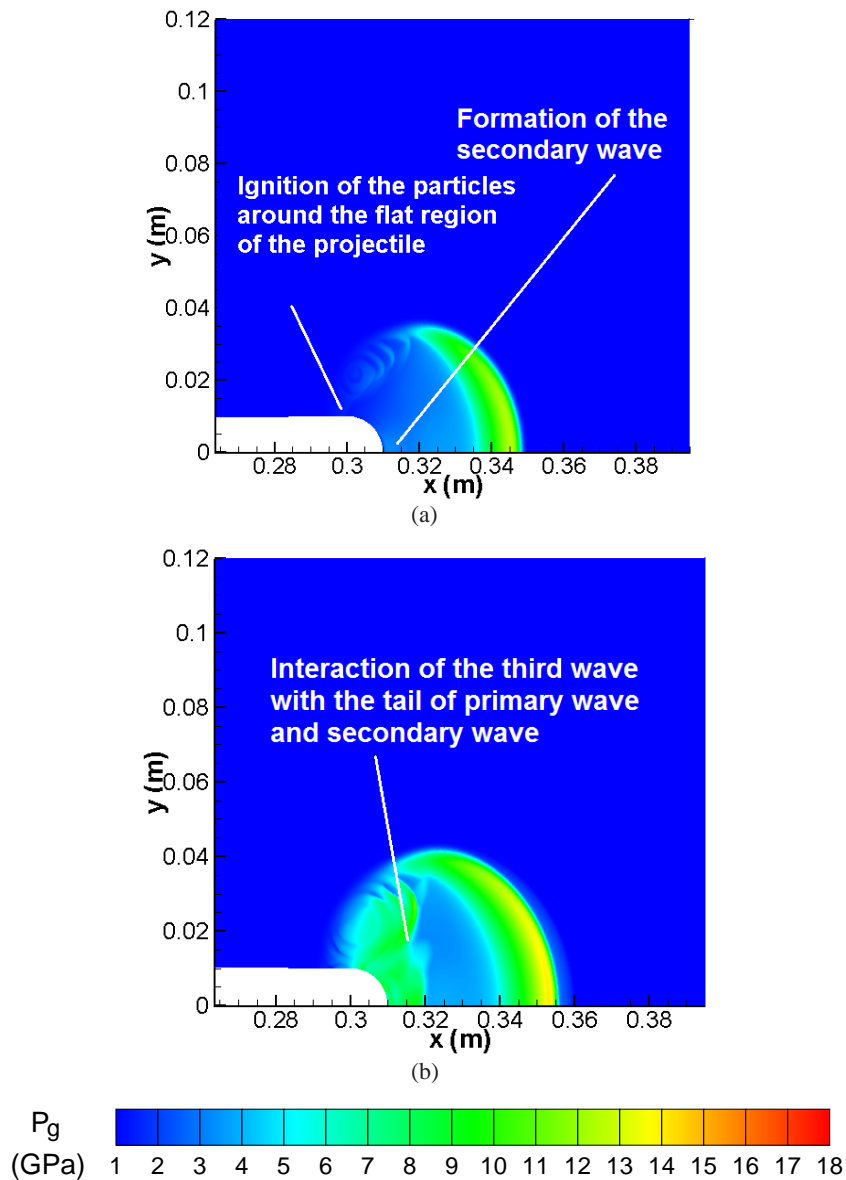
Figure 5.15: (a) Ignition of the particles around the flat region of the projectile and formation of third wave (12.7 μs), (b) interaction of the third wave with primary and secondary waves (14 μs) for the blunt-nosed projectile impact case of 100 m/s with $r = 10$ mm cone radius

Another interesting observation is the ignition of the particles around the flat region of the projectile (or corner of the projectile) and interaction of the generated third wave by this ignition mechanism with the tail of the primary wave (Figure 5.7 (f), (g)). This third wave structure also interacts with the secondary wave structure formed around the curved part of the projectile nose. The secondary and third wave fronts combine with each other and propagates as a single wave front in high pressure and temperature region (Figures 5.7 (f), (g), (h), (i)). These situations are also criticized in Figure 5.15 by repeating Figures 5.7 (f), (i).
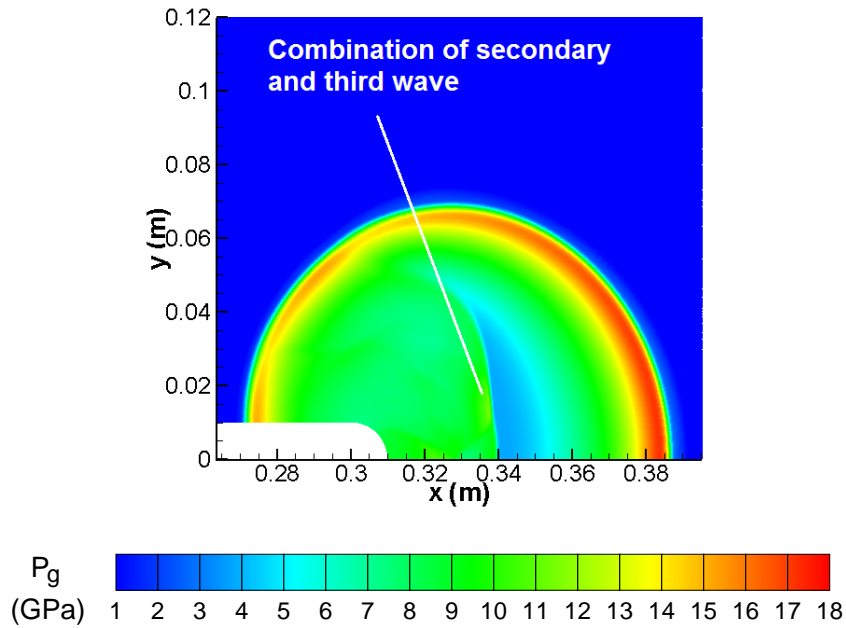
Figure 5.16: Combination of secondary and third waves for the blunt-nosed projectile impact case of 100 m/s with $r = 10$ mm cone radius

The secondary and third wave structures combine to each other to form a single wave structure in the high pressure and temperature region of the primary wave (Figure 5.16). After 18.5 μs from the bullet impact (Figure 5.7 (h)), two wave fronts are observed in the domain: (i) one propagates through the downstream of the explosive domain and, (i) the other propagates through the high pressure and temperature region of the primary wave as mentioned.

In Figure 5.10 the gas-phase temperature profiles are given for 100 m/s impact case of blunt-nosed projectile. It is observed that in compaction region, in high pressure and temperature region and, in primary deflagration wave the gas-phase temperatures are on the orders of 500 K, 4000 K and 14000 K, respectively.

In Figures 5.17 and 5.18, evolution of gas-phase pressure and density profiles for 150 m/s impact situation are shown. All the phenomena here is very similar to the 100 m/s bullet impact case. But a very interesting situation is observed in this case: The ignition of the particles on the flat region of the projectile takes place nearly simultaneously with the primary one (Figure 5.17 (b) and Figure 5.19 (a)). Following the formation of the primary and secondary wave structures, a wave structure also forms around the curved part of the projectile nose like in the 100 m/s case (Figure 5.17 (c) and Figure 5.19 (b)). Then the secondary wave interacts with this structure (Figure 5.17 (d) and Figure 5.20 (a)) to form a third wave structure. In Figure 5.20 (b) propagation of this triple wave structure is observed.

The ignition of the particles on the flat region of the projectile (or corner of the projectile) is discussed on solid-phase temperature (T_p) line plots extracted from the corner of the projectile in Figure 5.21 (a). The T_p values for 100 m/s impact condition are given in Figure 5.21 (b). Here the ignition is defined as the exceed of the T_p value over the 310 K. For the 100 m/s case, in the projectile corner, the T_p value exceeds the 310 K at about 11 μs. Whereas for 150 m/s case (Figure 5.21 (c)), ignition of the particles in the projectile corner is observed at about 2.7 μs. It is pointed out that, for the 150 m/s case, the ignition of particles at the corner of the projectile is achieved faster than that of 100 m/s case.

For 100 and 150 m/s impact velocities, it is determined that the ignition of the particles in the explosive domain is achieved. To determine the sensitivity of this impact velocity, a set of calculations are also performed for 50 m/s impact velocity (Figure 5.22). It is concluded that the gas-phase pressure increases and a compaction wave is formed in the domain similar to the 100 m/s and 150 m/s cases. But in this case this increase does not cause the ignition of the particles neither around the curved part of the projectile nose nor on the flat region of the projectile. This is a very important finding for blunt impact case: 50 m/s impact of blunt-nosed projectile cannot cause any sensitivity on the HMX explosive bed for reaction.
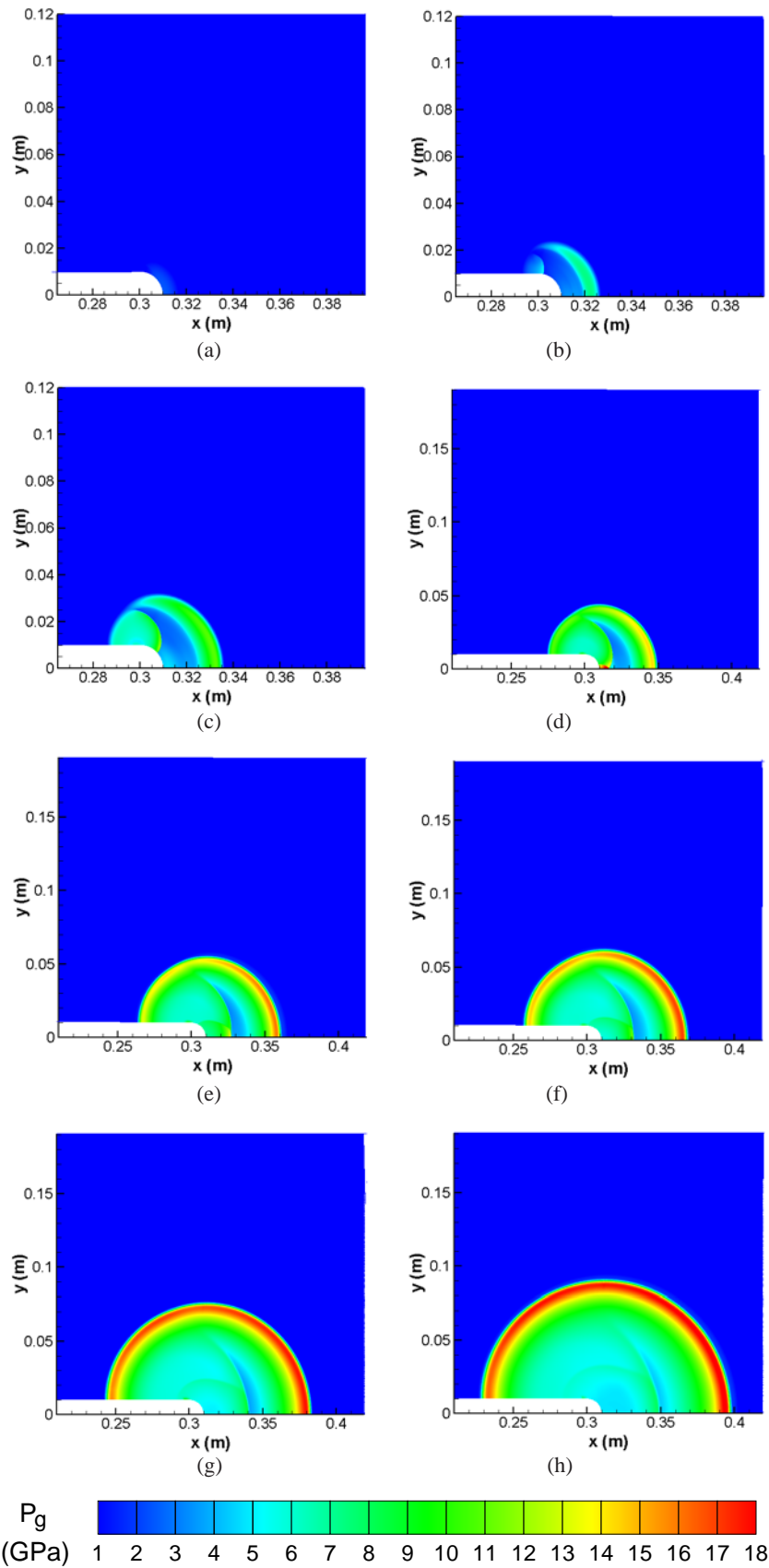
Figure 5.17: Evolution of gas-phase pressure contours for blunt-nosed projectile impact case of 150 m/s with r = 10 mm cone radius for (a) 5.6, (b) 8.1, (c) 9.9, (d) 12.3, (e) 14.3, (f) 15.3, (g) 17.5, (h) 19.8 μs
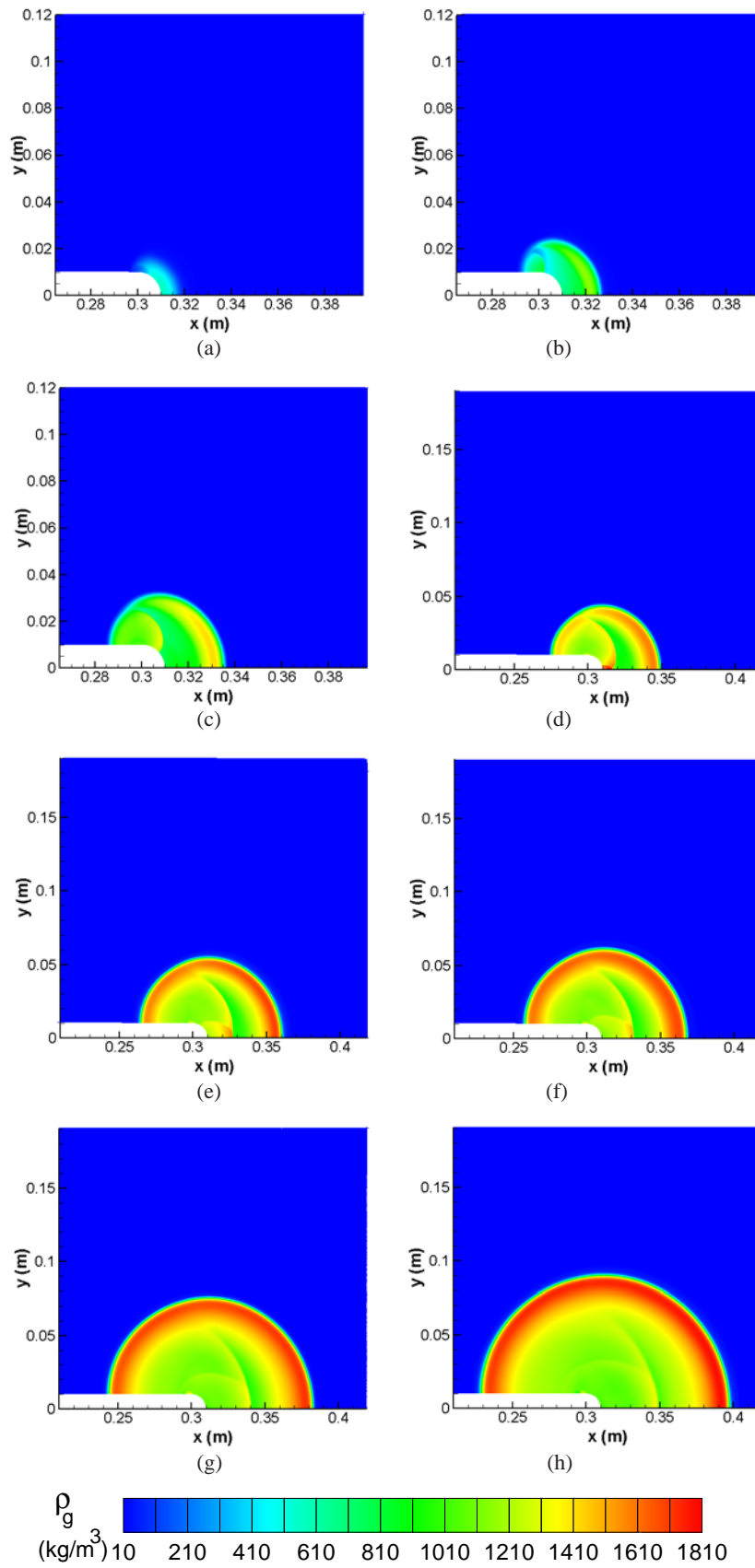
Figure 5.18: Evolution of gas-phase density contours for blunt-nosed projectile impact case of 150 m/s with r = 10 mm cone radius for (a) 5.6, (b) 8.1, (c) 9.9, (d) 12.3, (e) 14.3, (f) 15.3, (g) 17.5, (h) 19.8 μs
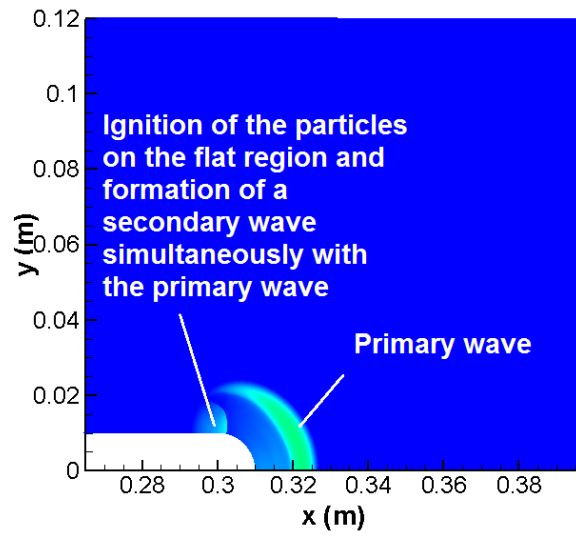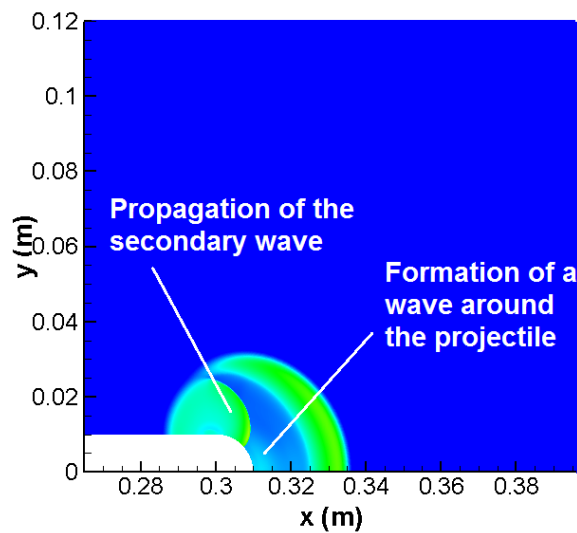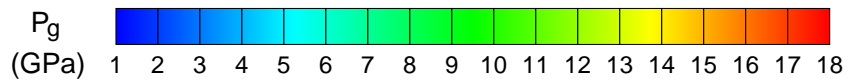
Figure 5.19: (a) Formation of the secondary wave because of the ignition of the particles on flat region of projectile, (b) propagation of this secondary wave and formation of a wave structure around the curved part of the projectile nose for the blunt-nosed projectile impact case of 150 m/s with $r = 10$ mm cone radius (Figures 5.17 (b) and (c)are repeated, respectively)
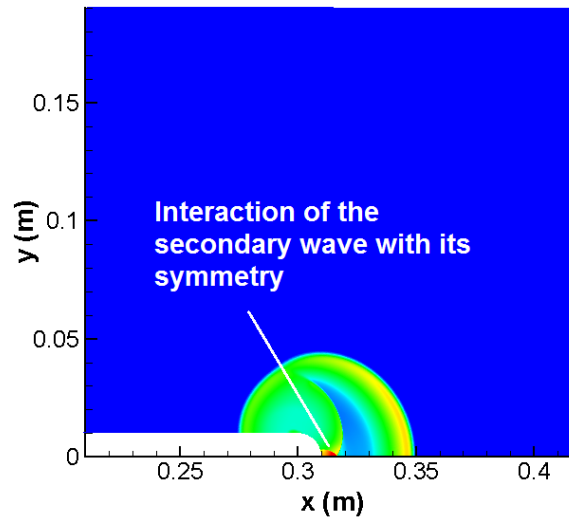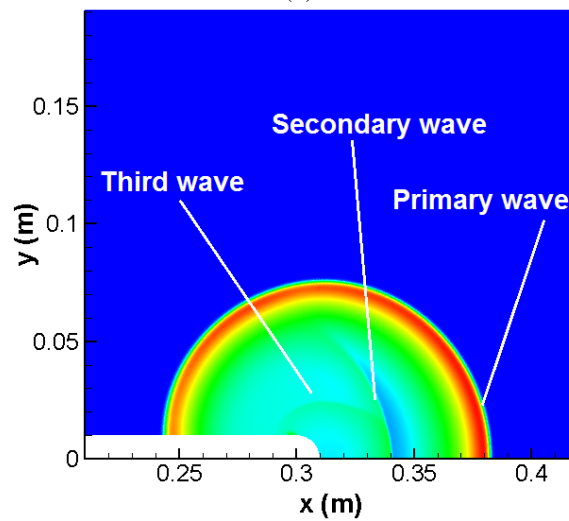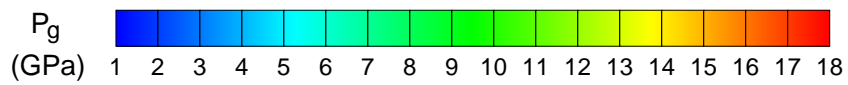
Figure 5.20: (a) Interaction of secondary wave with its symmetry and, formation of a third wave because of this interaction, (b) propagation of the triple wave structure in the domain for the blunt-nosed projectile impact case of 150 m/s with $r = 10$ mm cone radius (Figure 5.17 (d) and (f) are repeated, respectively)
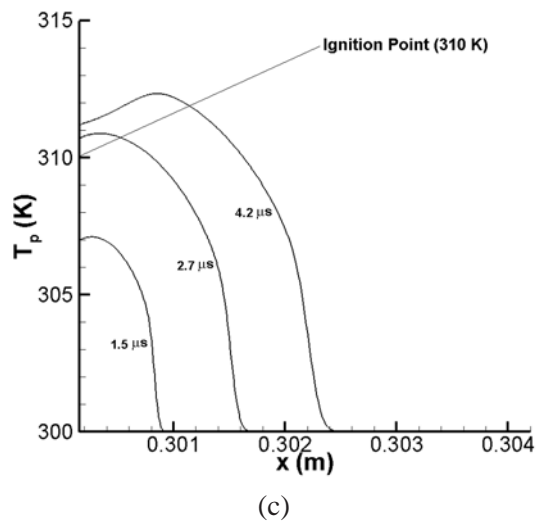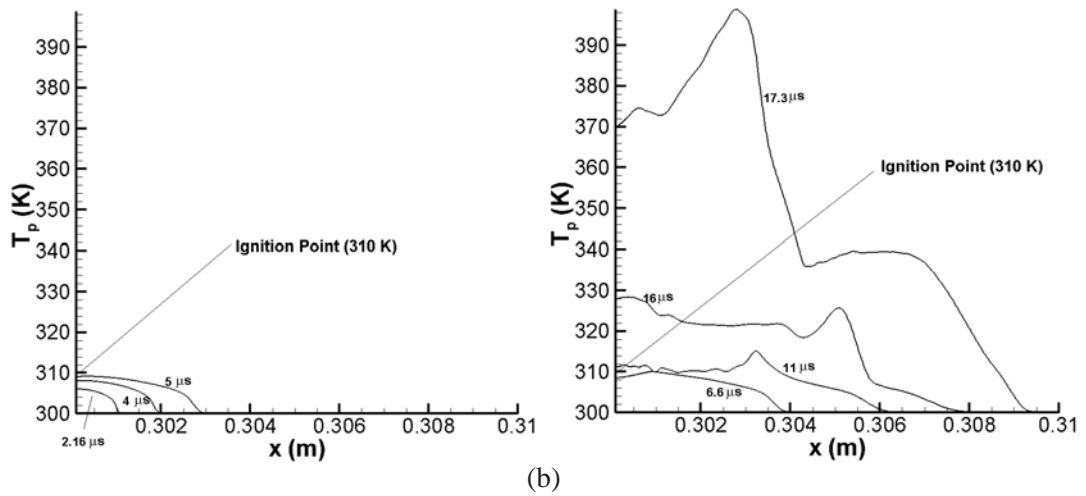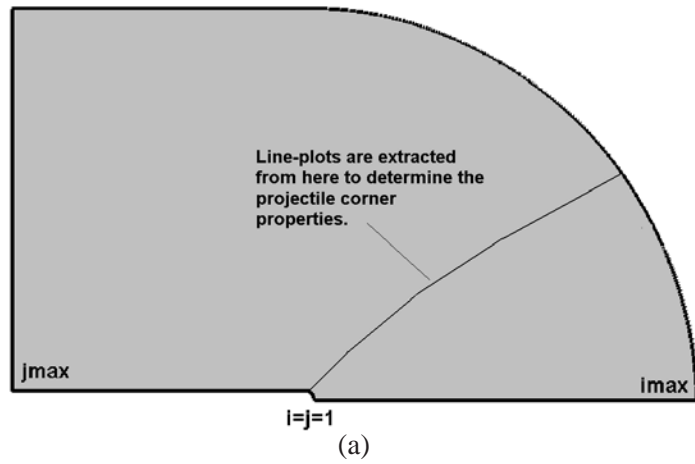
Figure 5.21: (a) Illustration of extraction line for line-plot of projectile corner properties, (b) T_p line plots for 100 m/s impact situation at projectile corner (through the constant line), (c) T_p line plots for 150 m/s impact situation at projectile corner (through the constant line) for the blunt-nosed projectile with $r = 10$ mm cone radius
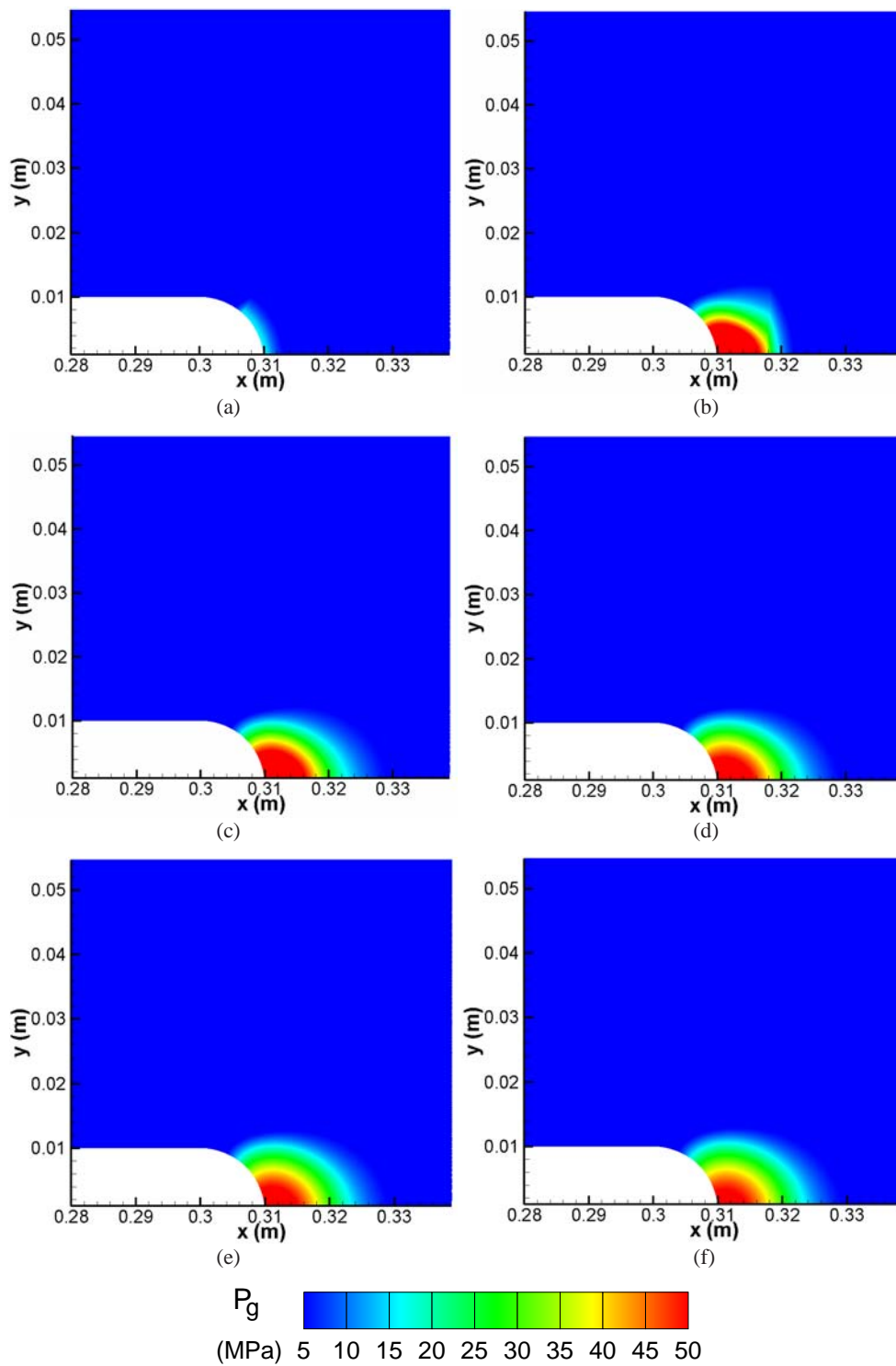
Figure 5.22: Evolution of gas-phase pressure contours for blunt-nosed projectile impact case of 50 m/s with $r = 10$ mm cone radius for (a) 5.8, (b) 7.4, (c) 9, (d) 10.8, (e) 12.2, (f) 18.8 μs

5.2.2 Sharp-nosed projectile impact problem

Sharp-nosed projectile impact situation is illustrated in Figure 5.23. For this case it is assumed that the process is started with the penetration of nose of the sharp-nosed projectile. The half cone angle of the projectile is $45°$. Like in the blunt case, effects of 100, 150 and 50 m/s impact velocities are investigated.
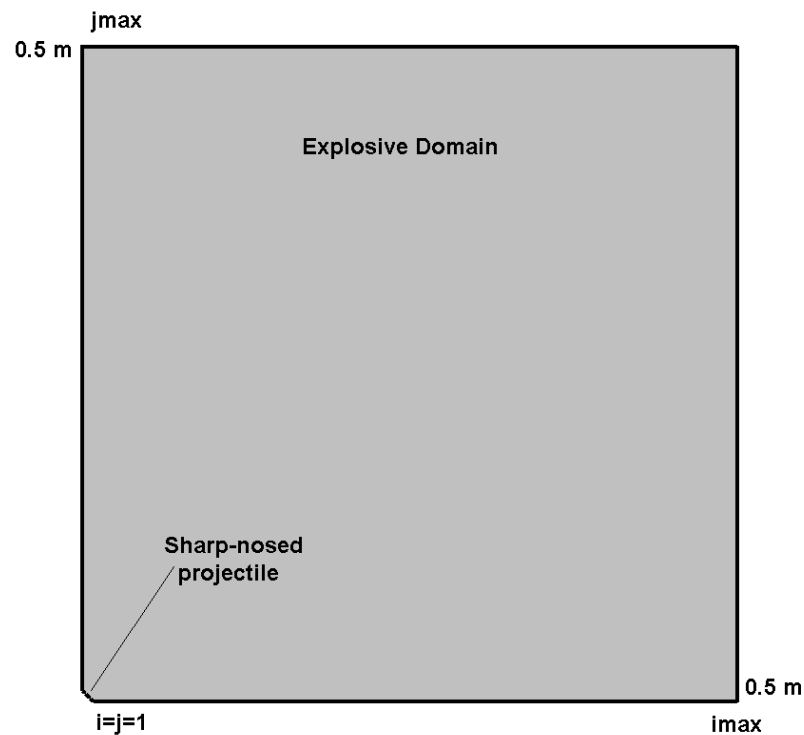
Figure 5.23: Physical demonstration of sharp-nosed projectile impact situation

For the simulation of this case, h-grid is generated by taking into account the given form in Figure 5.23. The domain is 0.5x0.5 m^2 with 1001x1001 grid resolution (Figure 5.24). In this first part of the calculations for the sharp-nosed projectile impact situation, it is assumed that the all the processes start the penetration of the sharp-nose of the projectile. In blunt-nosed impact calculations, the upstream boundary is removed away from the nose which means that all the processes start after a specific embedment of the projectile nose.
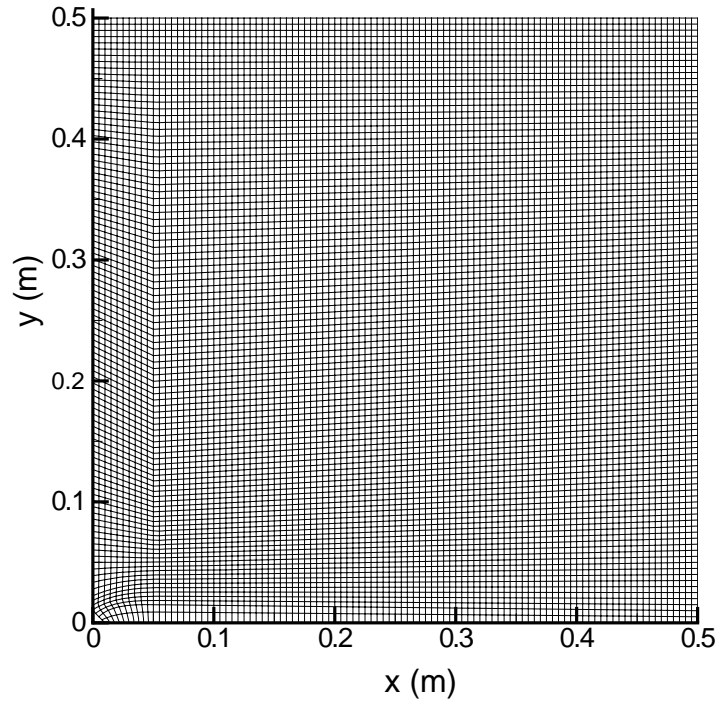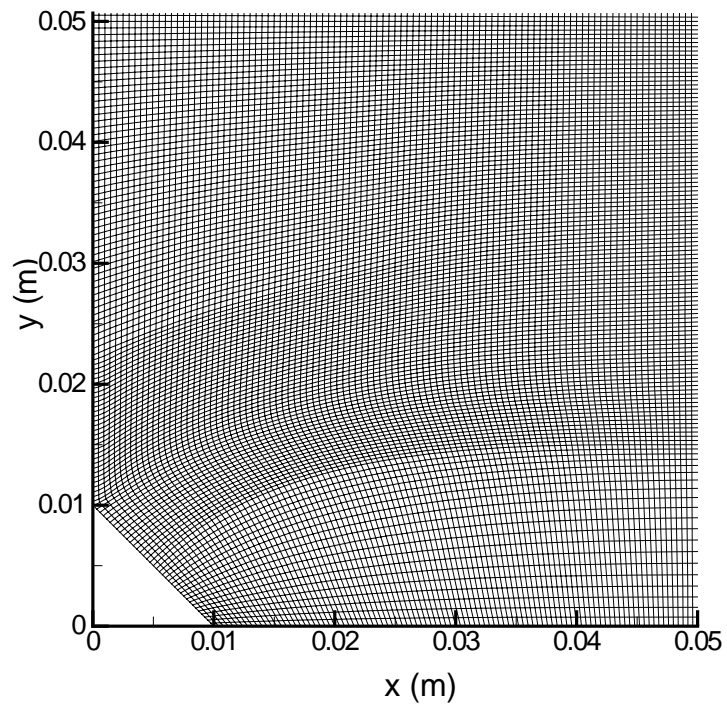
Figure 5.24: Solution grid for the sharp-nosed projectile impact situation (a) full-scale view with every 10 points shown, (b) zoomed view

In Figures 5.25 and 5.26 gas-phase pressure and density profiles for 100 m/s impact case are given. Very similar to the blunt case, compaction wave forms in the explosive domain and this compaction wave causes the formation of a high pressure and temperature region. In the compaction region, gas-phase pressure is about 20 MPa, whereas in high pressure and temperature region gas-phase pressure is about 150 MPa (Figures 5.27 (a) and (b)). After the formation of the primary wave, gas-phase pressure increases to about 2.5 GPa similar to the blunt-impact case (Figure 5.28 (a)). In this 100 m/s impact case, similar to blunt-nosed projectile 100 m/s impact case, a secondary shock wave formation in the high pressure and temperature region is observed ((Figure 5.28 (b)) with the effect of backward wave propagation after the formation of the primary wave (Figures 5.26 (c), (d)).
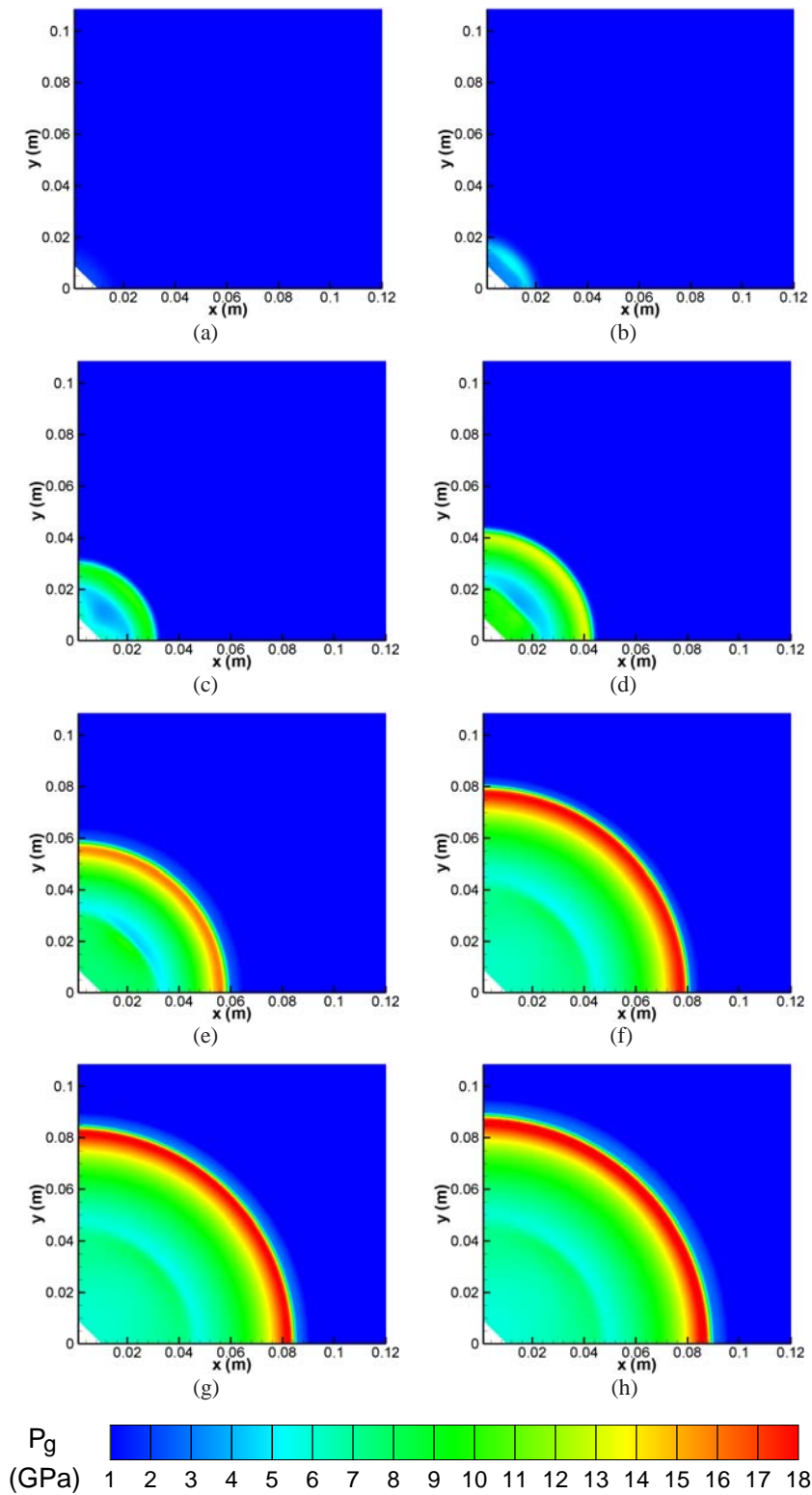
Figure 5.25: Evolution of gas-phase pressure contours for the sharp-nosed projectile impact case of 100 m/s with 45° half cone angle for (a) 7, (b) 8, (c) 10, (d) 12.2, (e) 16.4, (f) 18.1, (g) 19.5, (h) 21.9 μs
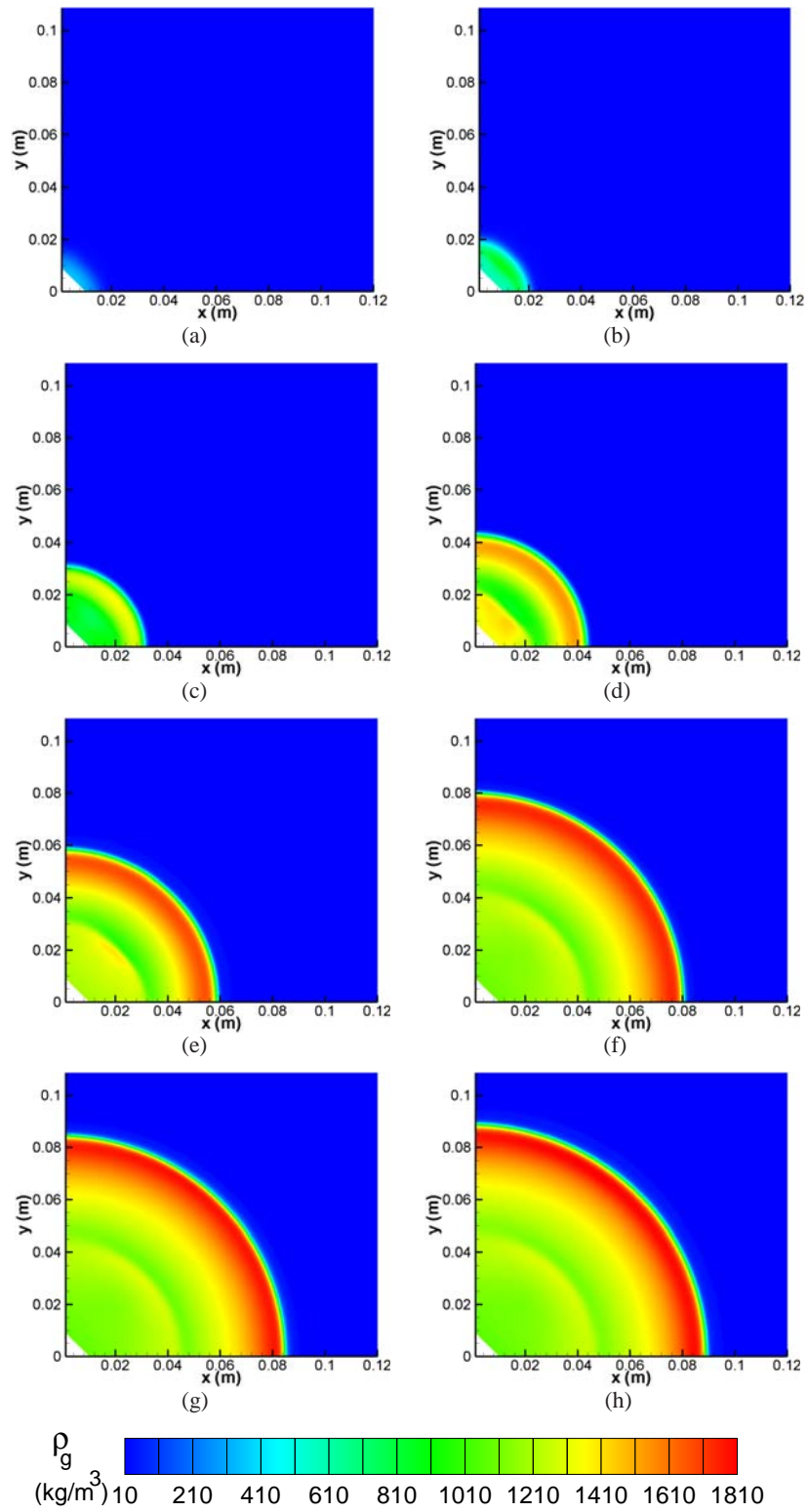
Figure 5.26: Evolution of gas-phase density contours for the sharp-nosed projectile impact case of 100 m/s with 45° half cone angle for (a) 7, (b) 8, (c) 10, (d) 12.2, (e) 16.4, (f) 18.1, (g) 19.5, (h) 21.9 μs
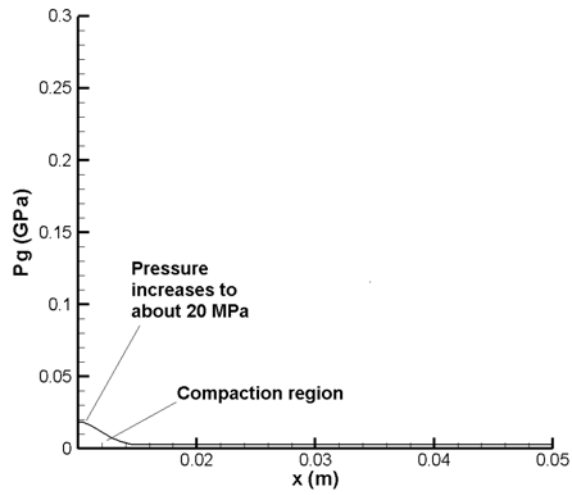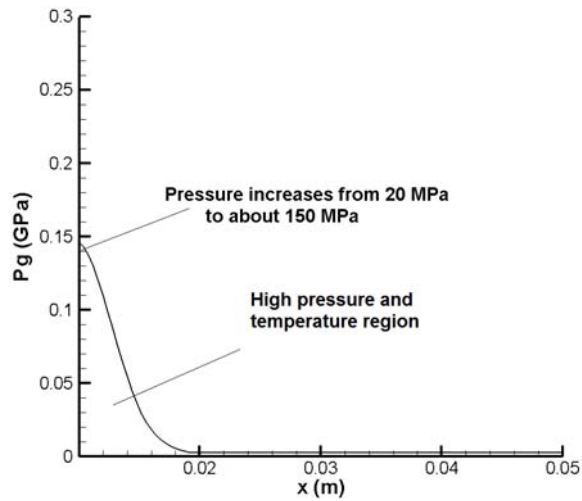
Figure 5.27: (a) Formation of compaction region and, (b) formation of high pressure and temperature region projectile impact case of 100 m/s with 45° half cone angle ((extracted from the $y = 0$ symmetry axis)
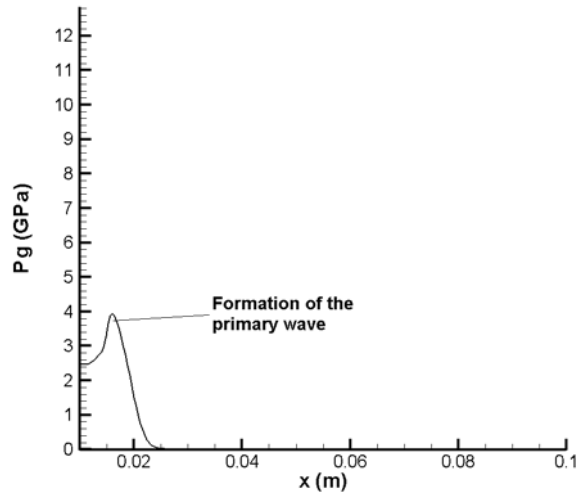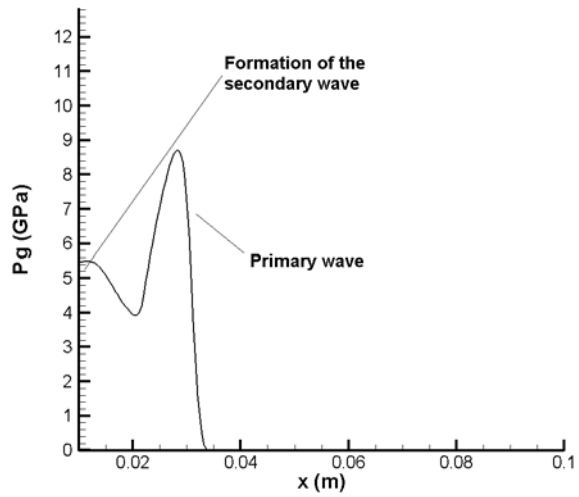
Figure 5.28: (a) Formation of the primary wave and, (b) formation of secondary wave in high pressure and temperature region for the sharp-nosed projectile impact case of 100 m/s with 45° half cone angle (extracted from the $y = 0$ symmetry axis)

Propagation of the primary wave, formation and propagation of the secondary wave is also seen in solid-phase volume fraction (ϕ_p) line plots extracted from the $y = 0$ symmetry axis (Figure 5.29). These line-plots show the formation of the primary wave, formation of the secondary wave and, propagation of both waves in the domain. In the upstream of the primary wave, the ϕ_p value decreases, which defines the consumption of the explosive particles. After the formation of secondary wave with the effect of backward wave propagation in the high pressure and temperature domain, the ϕ_p value starts to decrease in this domain also.
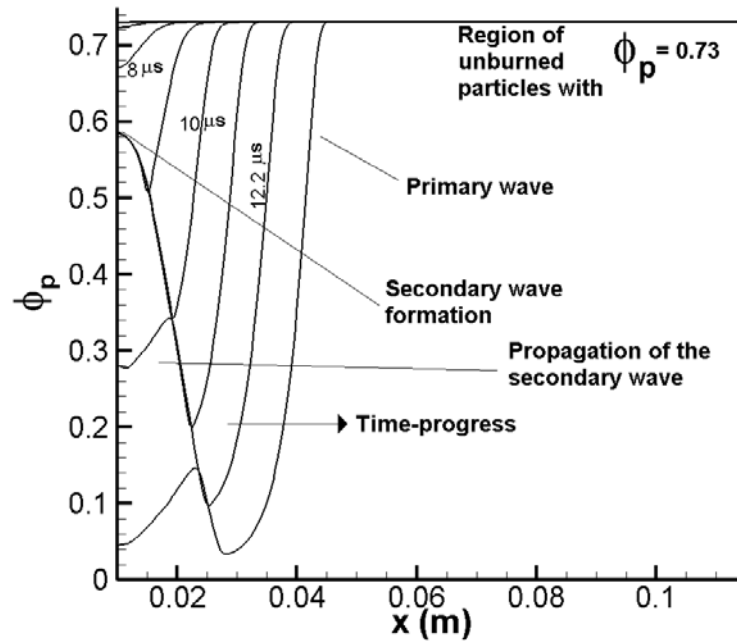
Figure 5.29: ϕ_p line plots extracted from the $y = 0$ symmetry axis for the sharp-nosed projectile impact case of 100 m/s with 45° half cone angle

The calculations for sharp-nosed impact situation with 100 m/s impact velocity are repeated with a similar grid topology (O-grid) used for blunt-nosed calculations. For this it is assumed that the nose of the projectile is embedded into the explosive domain. By this manner it is aimed to avoid from the possible upstream boundary reflection effects. The grid topology used in the calculations is given in Figure 5.30.
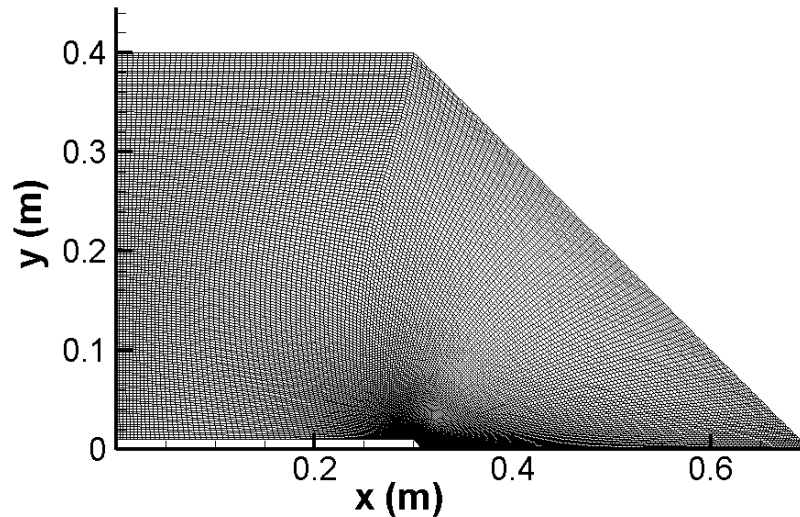
Figure 5.30: Solution grid for sharp-nosed projectile impact situation in O-grid topology (full-scale view with every 10 points shown)

The gas-phase pressure and density profiles for this new grid topology is given in Figures 5.31 and 5.32, respectively. Similar to the blunt-nosed impact case, after the formation of the primary wave, a backward wave propagation is observed (Figure 5.33). This backward wave propagation causes the formation of the secondary wave on the projectile body when it hits to the projectile. Meanwhile, a third wave propagation around the flat region of the projectile is also observed (Figure 5.33) like in the blunt-nosed impact case. Remember that, in the calculations with no-embedded projectile nose (with H-grid topology) described above, the formation of third wave around the flat region of the projectile is not observed.
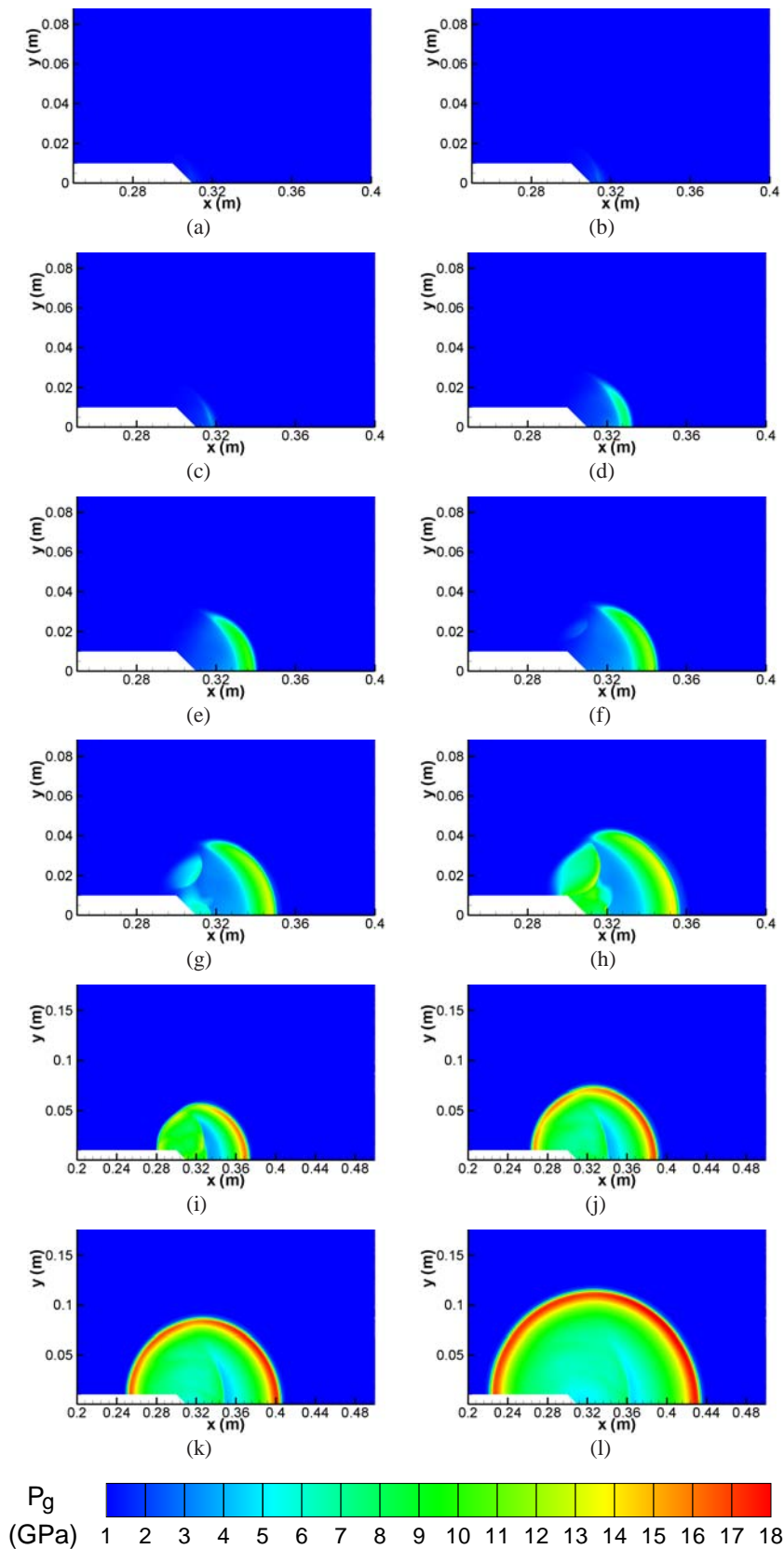
Figure 5.31: Evolution of gas-phase pressure contours for the sharp-nosed projectile impact case of 100 m/s with 45° half cone angle and with far-away upstream boundary for (a) 4,93, (b) 5.91, (c) 6.94, (d) 9.96, (e) 11.46, (f) 12.5, (g) 13.4, (h) 14.9, (i) 17.1, (j) 19.8, (k) 21.84, (l) 25.9 μs

101
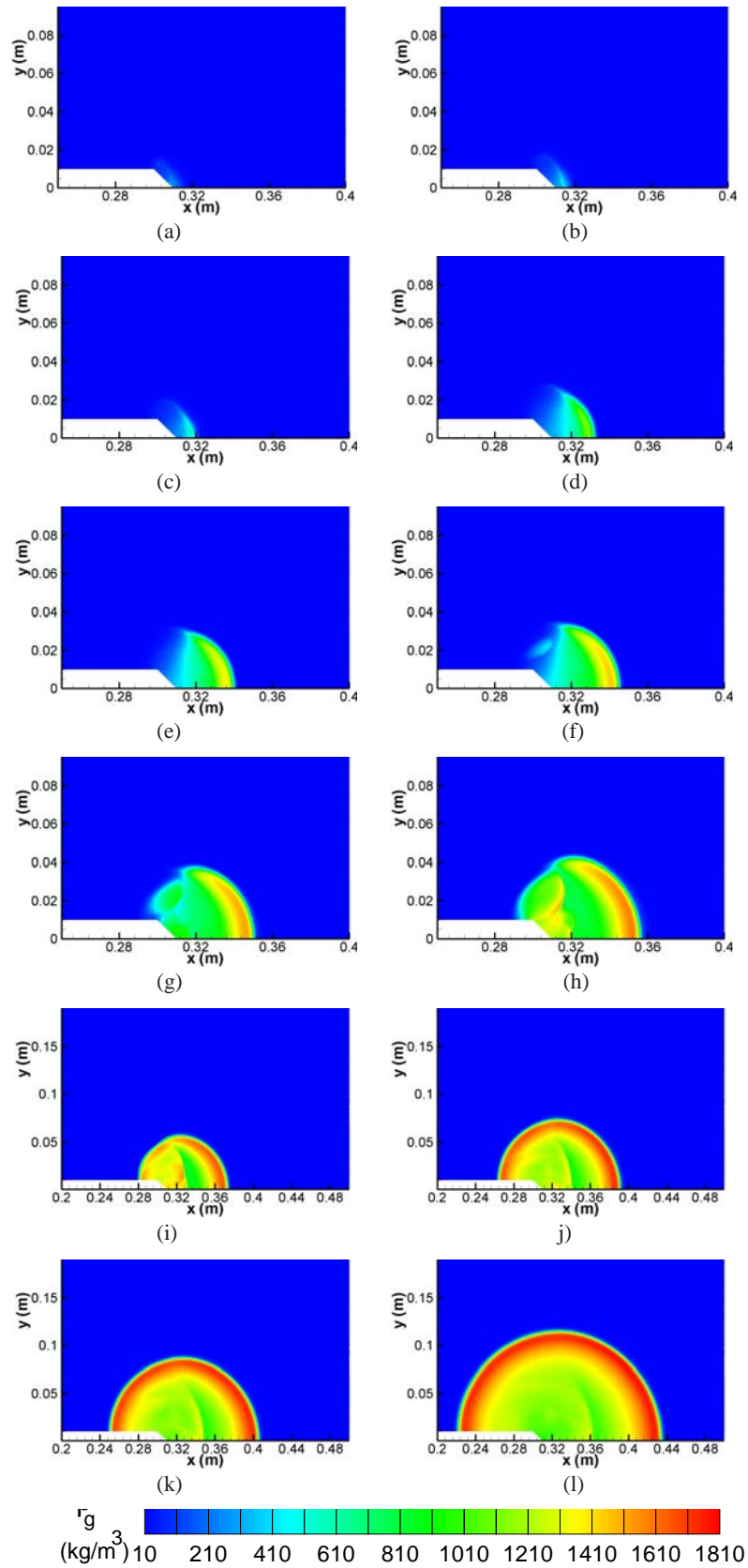
Figure 5.32: Evolution of gas-phase density contours for the sharp-nosed projectile impact case of 100 m/s with 45° half cone angle and with far-away upstream boundary for (a) 4,93, (b) 5.91, (c) 6.94, (d) 9.96, (e) 11.46, (f) 12.5, (g) 13.4, (h) 14.9, (i) 17.1, (j) 19.8, (k) 21.84, (l) 25.9 μs
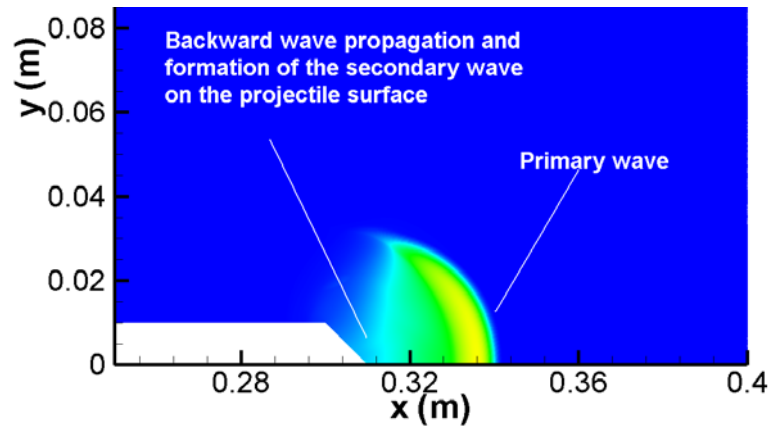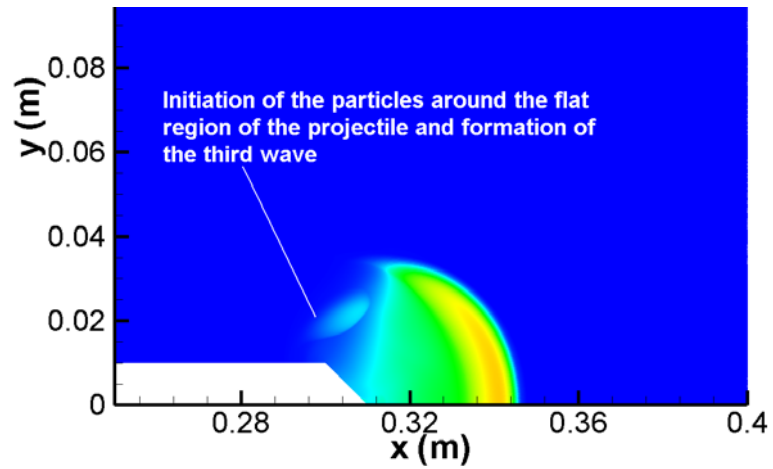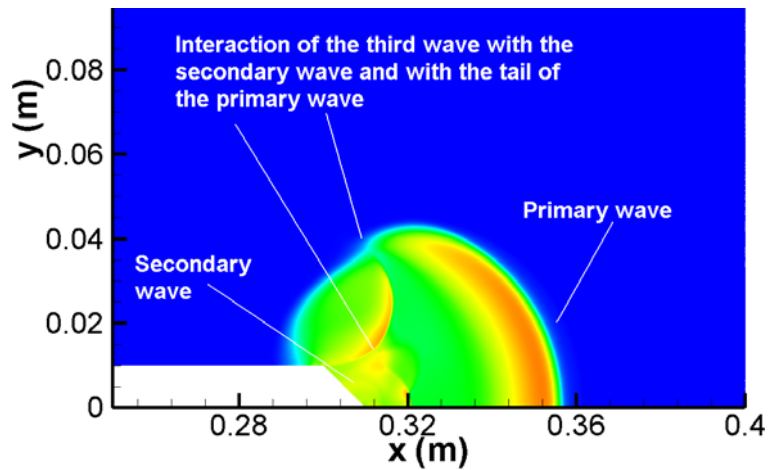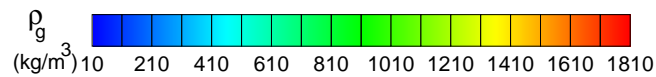
Figure 5.33: Gas-density profiles for the illustration of the formation of the secondary wave on the projectile body with the effect of backward wave propagation after the formation of the primary wave and formation of third wave for (a) 9.96, (b) 11.46, (c) 12.5 μs for the sharp-nosed projectile impact case of 100 m/s with 45° half cone angle and with far-away upstream boundary

103

Similar to the H-grid calculation case, formation of the secondary wave is also investigated in these calculations with far-away upstream boundary. Similar to the H-grid case, formation of the primary wave, formation of the secondary wave and, propagation of both waves in the domain is observed. In the upstream of the primary wave, the ϕ_p value decreases, which defines the consumption of the explosive particles. After the formation of secondary wave with the effect of backward wave propagation in the high pressure and temperature domain, the ϕ_p value starts to decrease in this domain also (Figure 5.34).
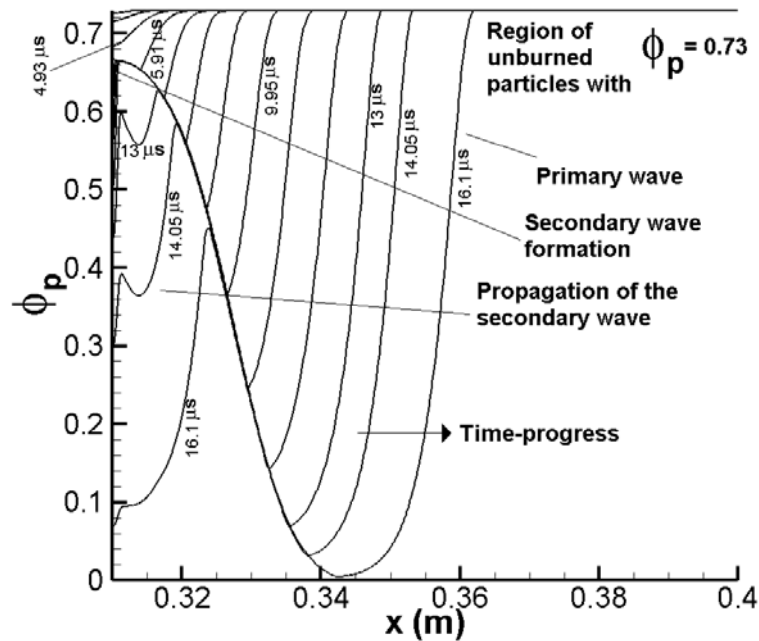
Figure 5.34: ϕ_p line plots extracted from the $y = 0$ symmetry axis for the sharp-nosed projectile impact case of 100 m/s with 45° half cone angle and with far-away upstream boundary

In Figures 5.35 and 5.36 gas-phase pressure and density profiles for 150 m/s impact case are given. Similar to the 100 m/s case, compaction and high pressure and temperature region formation phenomena are observed. But in this case secondary and third wave formation and propagation is not observed in the domain (on the corner of the projectile and on the projectile surface) and all the process is dominated only by the primary wave. Therefore, these calculations are also repeated with the new O-grid topology given in Figure 5.30 to see if any secondary and third wave formation may be obtained. The results are given in Figures 5.37 and 5.38. Similar to the blunt-nosed 150 m/s impact case, a secondary ignition on the corner of the projectile is observed (Figure 5.37 (d)). Meanwhile, a third wave formation is also observed on the projectile surface.
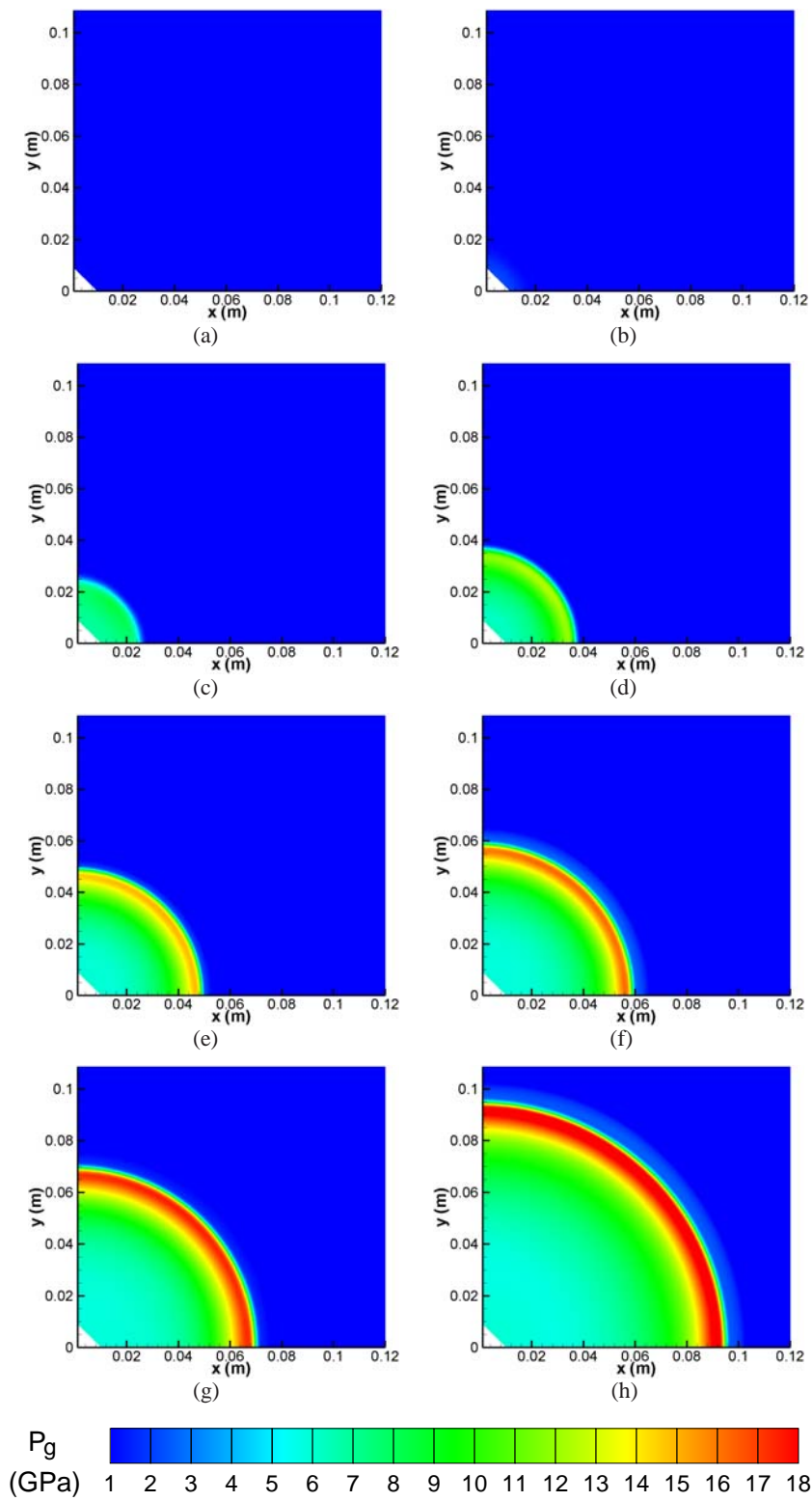
Figure 5.35: Evolution of gas-phase pressure contours for the sharp-nosed projectile impact case of 150 m/s with 45° half cone angle for (a) 5,3, (b) 7, (c) 8.5, (d) 10.8, (e) 12.9, (f) 14.6, (g) 17.1, (h) 20 μs
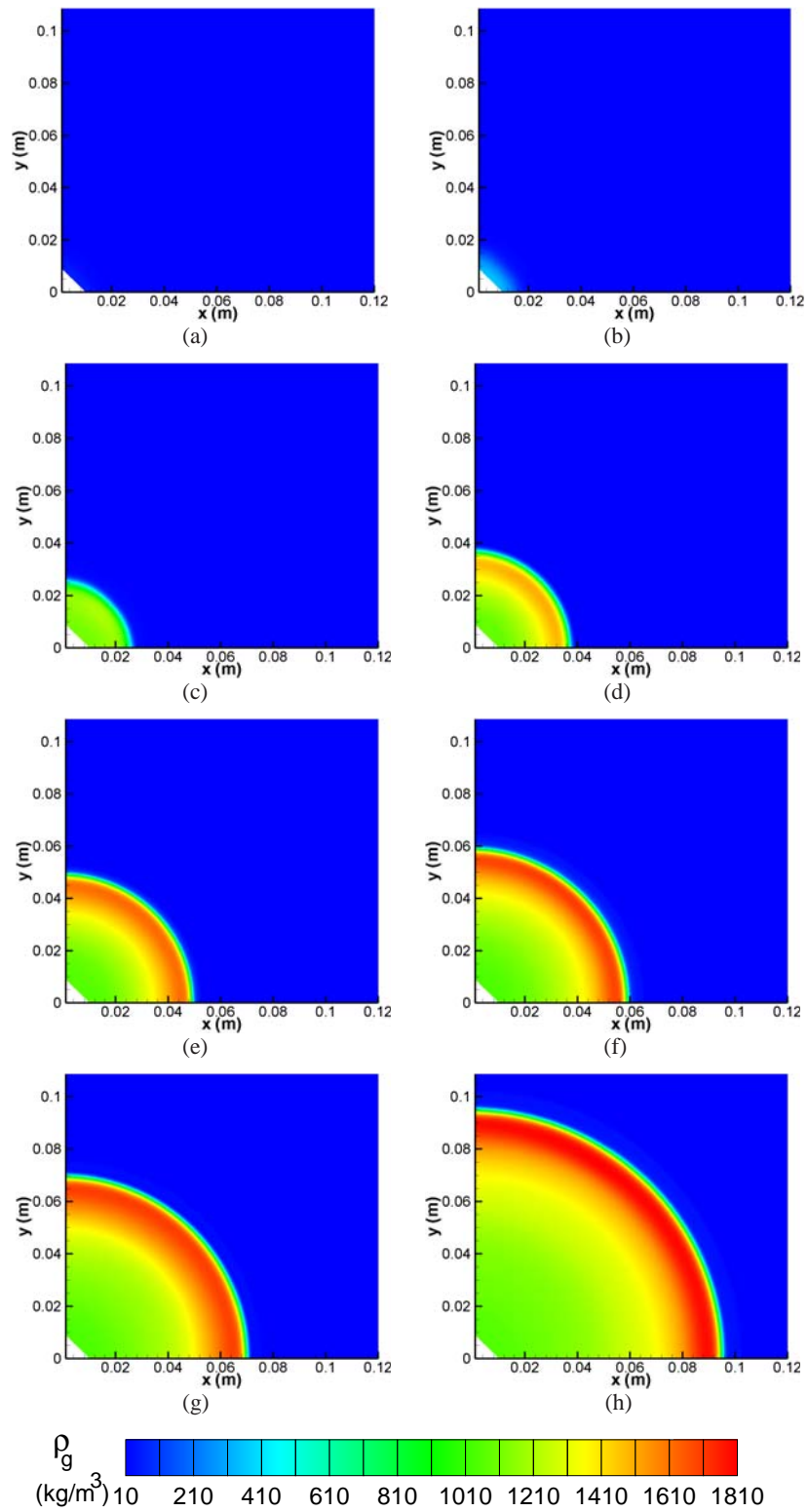
Figure 5.36: Evolution of gas-phase density contours for the sharp-nosed projectile impact case of 150 m/s with 45° half cone angle for (a) 5.3, (b) 7, (c) 8.5, (d) 10.8, (e) 12.9, (f) 14.6, (g) 17.1, (h) 20 μs

106
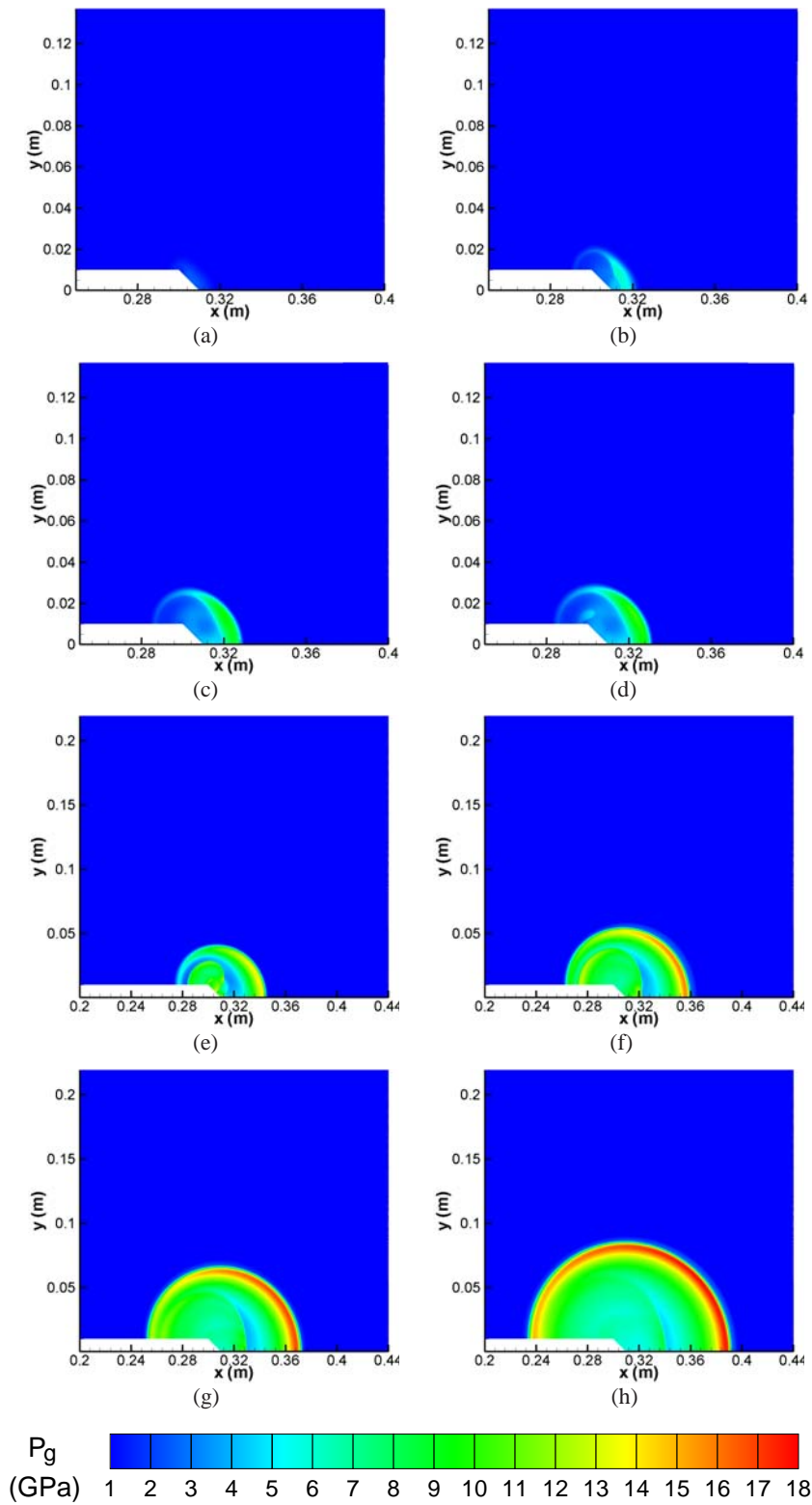
Figure 5.37: Evolution of gas-phase pressure contours for the sharp-nosed projectile impact case of 150 m/s with 45° half cone angle and with far-away upstream boundary for (a) 5.3, (b) 7.2, (c) 9.1, (d) 10.1, (e) 11.9, (f) 14.4, (g) 16.2, (h) 19.3 μs
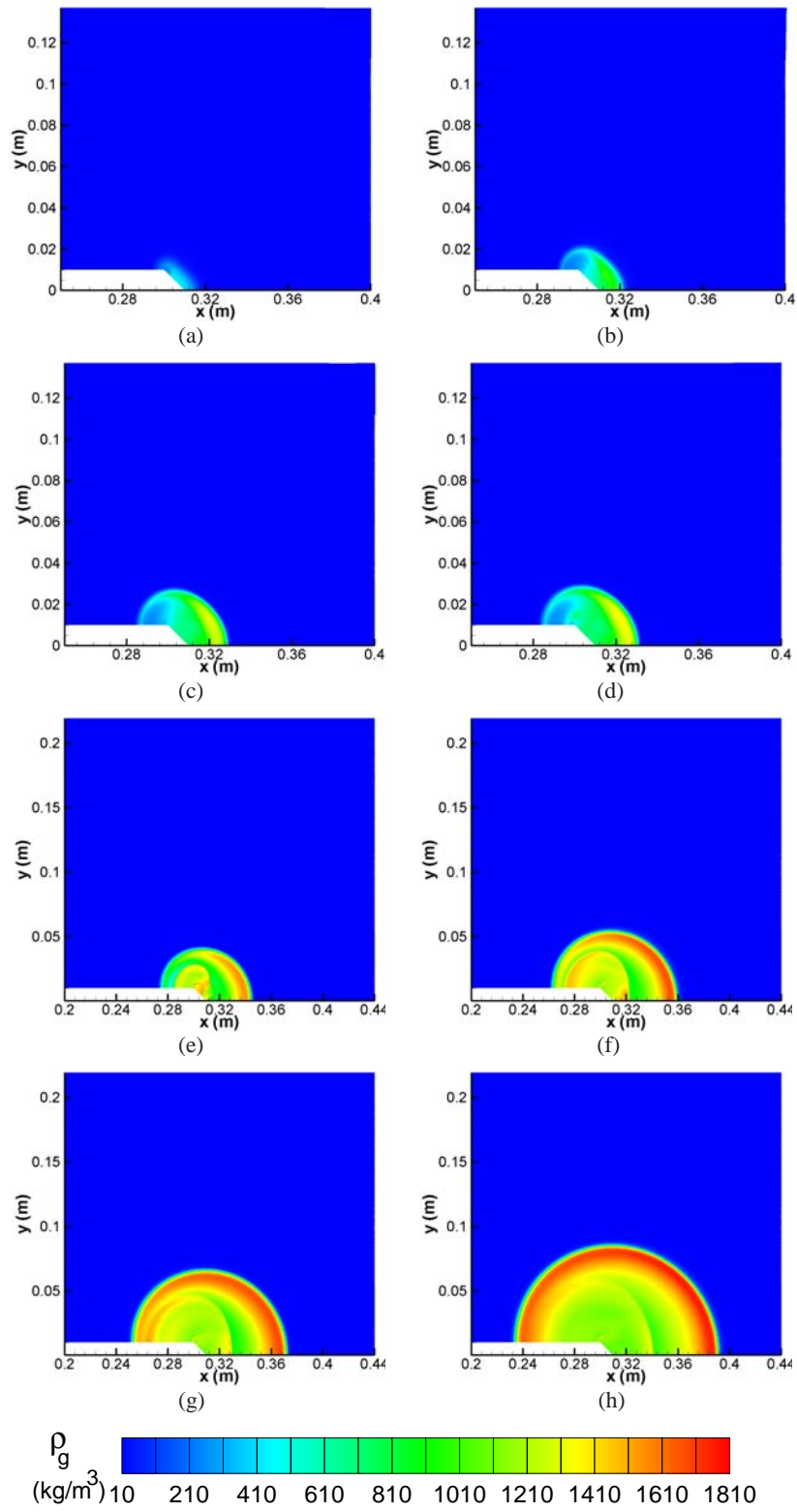
Figure 5.38: Evolution of gas-phase pressure contours for the sharp-nosed projectile impact case of 150 m/s with 45° half cone angle and with far-away upstream boundary for (a) 5.3, (b) 7.2, (c) 9.1, (d) 10.1, (e) 11.9, (f) 14.4, (g) 16.2, (h) 19.3 μs

108

In order to show the differences between the O-grid (without far-away upstream boundary) and H-grid (with far-away upstream boundary), ϕ_p line plots extracted from the $y = 0$ symmetry axis is used (Figure 5.39). As stated above, no secondary wave formation is observed for O-grid calculations(Figure 5.39 (a)), whereas for the H-grid calculations secondary wave formation is observed in the domain similar to the blunt-nosed impact case (Figure 5.39 (b)).

50 m/s impact velocity calculations are also performed for sharp-nosed as in the blunt-nosed impact case. The gas-phase pressure values are given in Figure 5.40. It is observed that the pressure value increases in the domain up to the compaction pressure value levels of around 30 MPa. But this increase does not lead to ignition of the particles and does not lead to formation of the high pressure and temperature region. Therefore, for this impact velocity it may be concluded that, detonation cannot be achieved like in the blunt 50 m/s case.
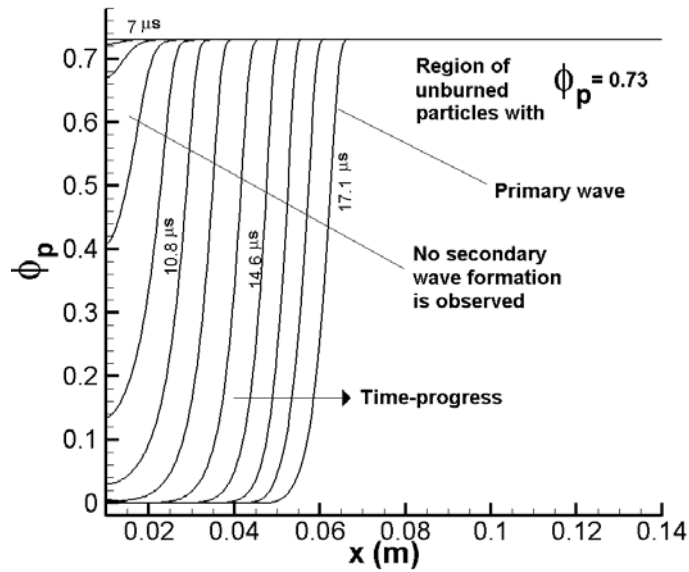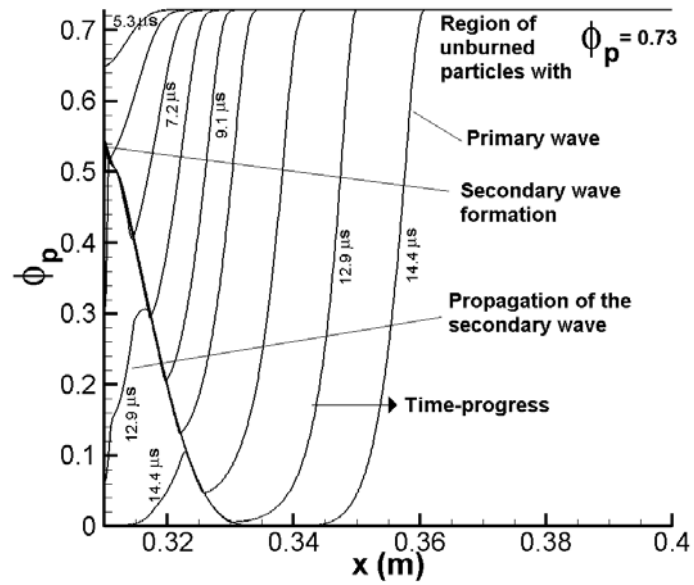
Figure 5.39: ϕ_p line plots extracted from the $y = 0$ symmetry axis for the sharp-nosed projectile impact case of 100 m/s with 45° half cone angle and with far-away upstream boundary, (a) for O-grid topology, (b) for H-grid topology
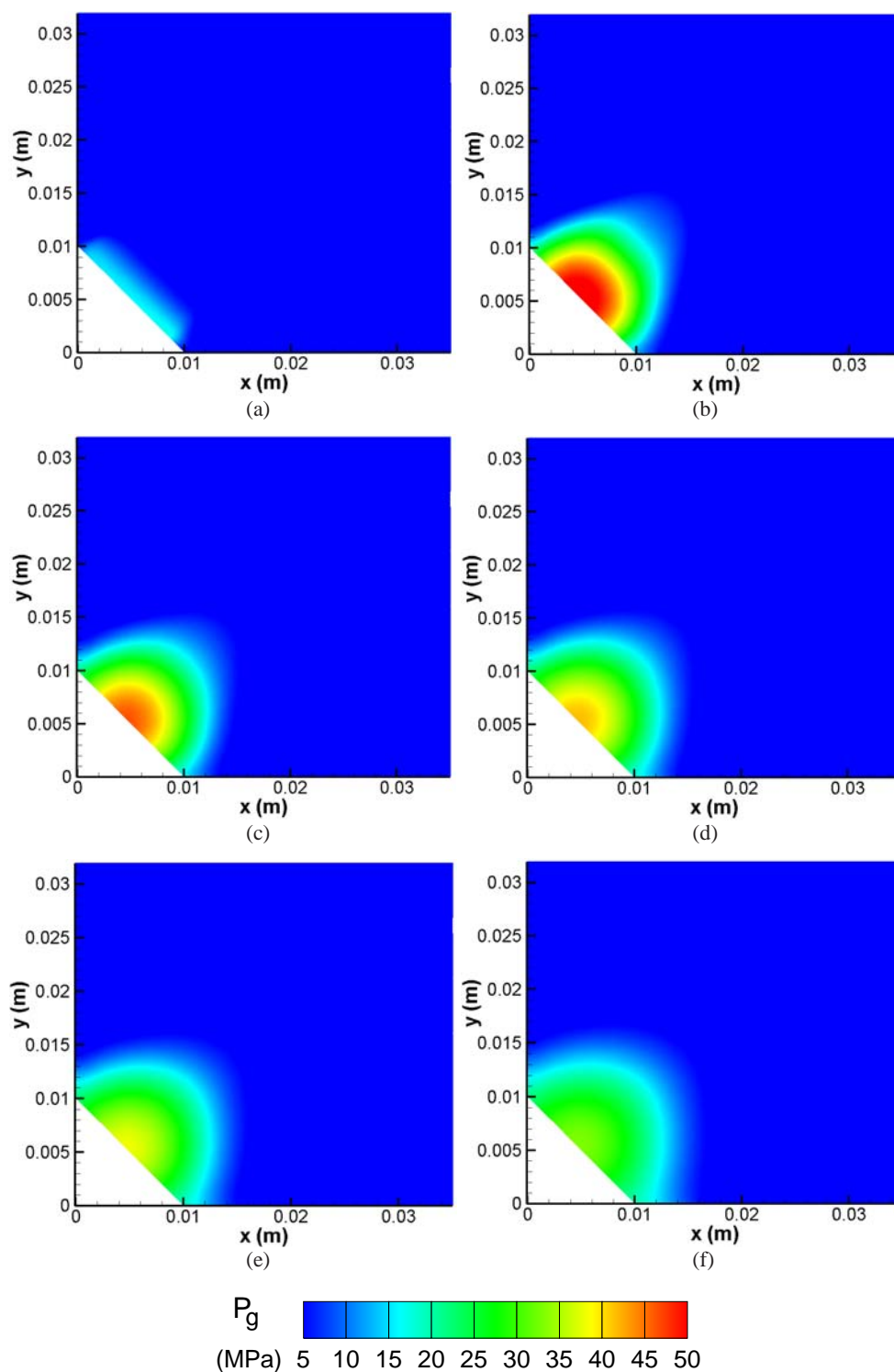
Figure 5.40: Evolution of gas-phase pressure contours for the sharp-nosed projectile impact case of 50 m/s with 45° half cone angle for (a) 1.8, (b) 5.5, (c) 7.4, (d) 9.2, (e) 11.1, (f) 20 μs

5.3 Wave-shaper investigations

In munitions engineering, shaped-charge type systems have great importance. A typical shaped-charge system may be defined as a hollow explosive in an axisymmetric configuration encapsulated with a metal liner in hollow part (Figure 5.41). These types of munitions systems are widely used against armors of battle-tanks or armored personnel carrier type military crafts. Besides, some special types of shaped-charge are used to attack against bunkers, depots, and aircraft shelters.
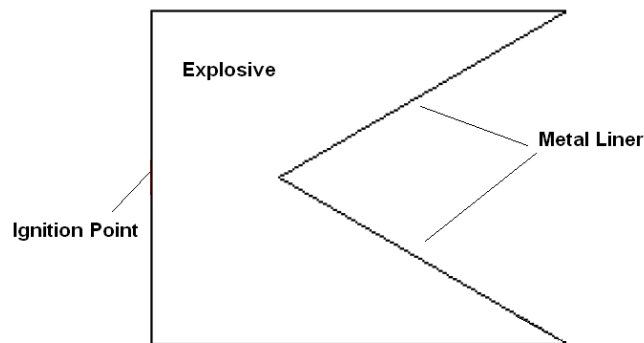
Figure 5.41: Shaped-charge concept

To improve the performance of shaped-charge systems, wave-shaper concept has been explored in the last twenty-years. In wave shaping, it is aimed to increase the shaped-charge jet velocity by re-shaping the detonation wave front to hit the metal liner. As the inclination angle decreases, shaped-charge velocity and shaped-charge efficiency increases (Figure 5.42).

In this study, a special wave-shaper problem is defined and results are compared to those of AutoDYN, a commercial Eulerian and Lagrangian hydrocode solver, for the same problem. The explosive domain is 0.08x0.04 m^2 with r=0.01 m spherical wave-shaper is located in it. The ignition of the explosive bed is performed by applying the piston BCs in the quarter part of the $i = 1$ constant line. This ignition zone is illustrated in Figure 5.43. The solution grid topology is seen in Figure 5.44.

In Figure 5.45, the evolution of the gas-phase pressure contours for the solution of the defined wave-shaper problem is given. This illustration aims to depict the evolution of wave under the effect of a specific wave-shaper geometry in this study.
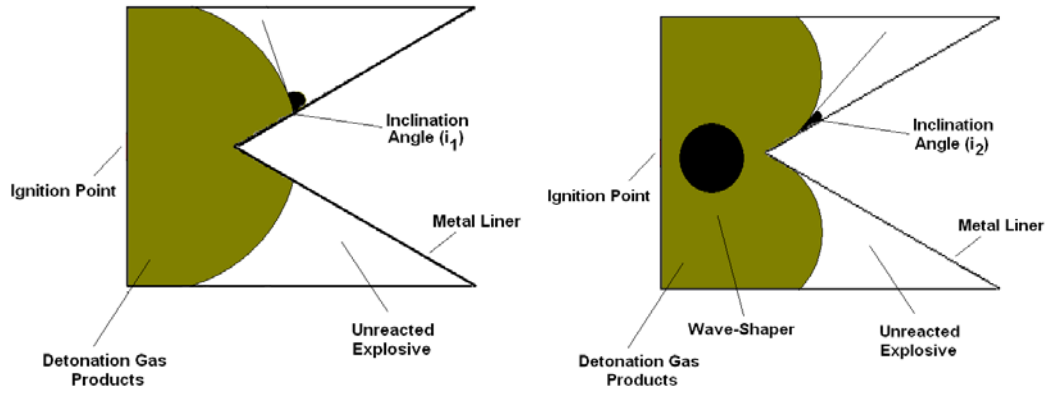
Figure 5.42: Wave-shaper concept ($i_2 < i_1$)
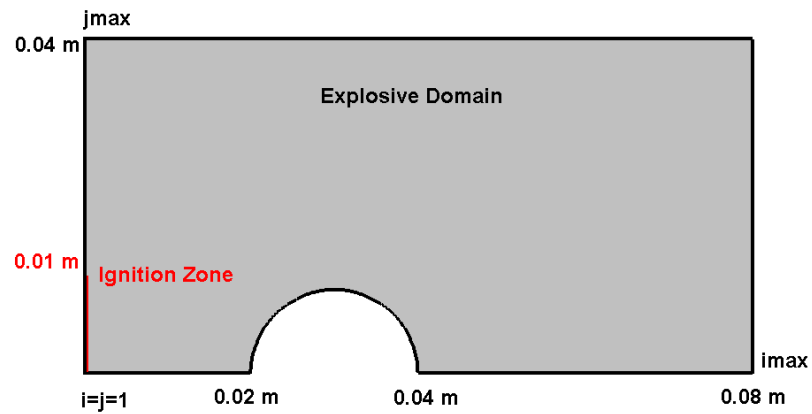
Figure 5.43: Illustration of the wave-shaper problem for this study

In Figure 5.46, shaped-charge liner is located to the domain for t=16 μs to determine the incidence angle. It is determined that incidence angle is 13.1° for this case. The same problem is solved by AutoDYN by using Octol 70/30 explosive since any mechanical and thermal ignition model is not existent for HMX. But Octol 70/30 includes 70 % HMX and, 30 % TNT with 1800kg/m^3 bulk density, 8330 m/s detonation wave velocity (i.e. D_{cj}) and, 32 GPa detonation pressure (i.e. P_{cj}). This post detonation properties are slightly greater than those of pure HMX that we have taken into account in this study (P_{cj} = 25 GPa and, D_{cj} = 7500 m/s).
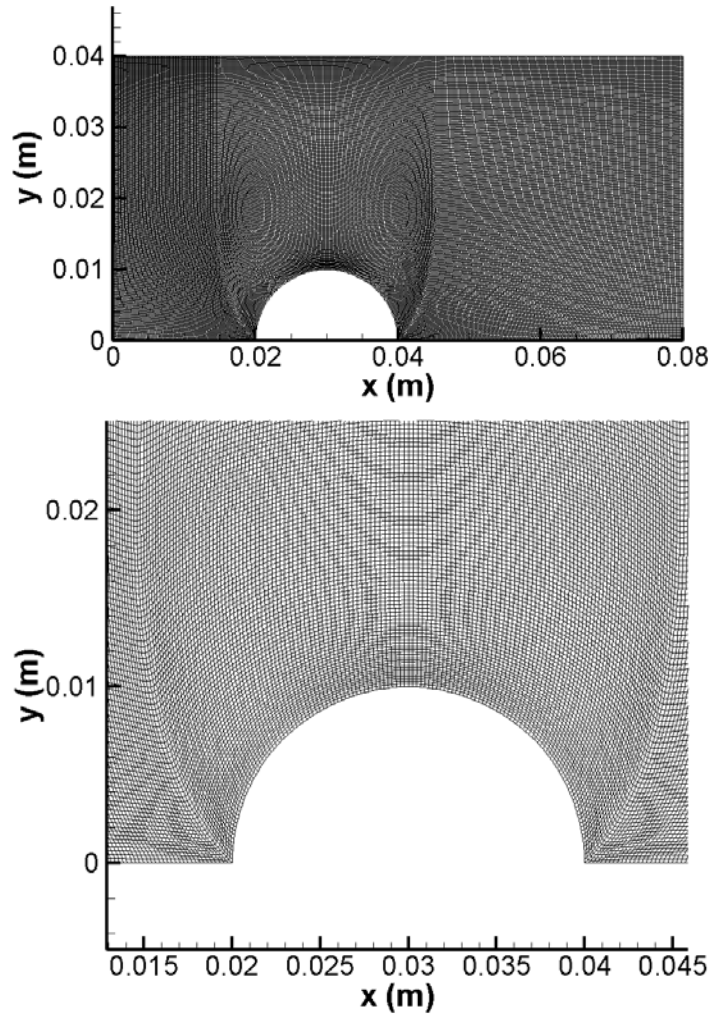
Figure 5.44: Solution grid topology for wave-shaper problem of this study
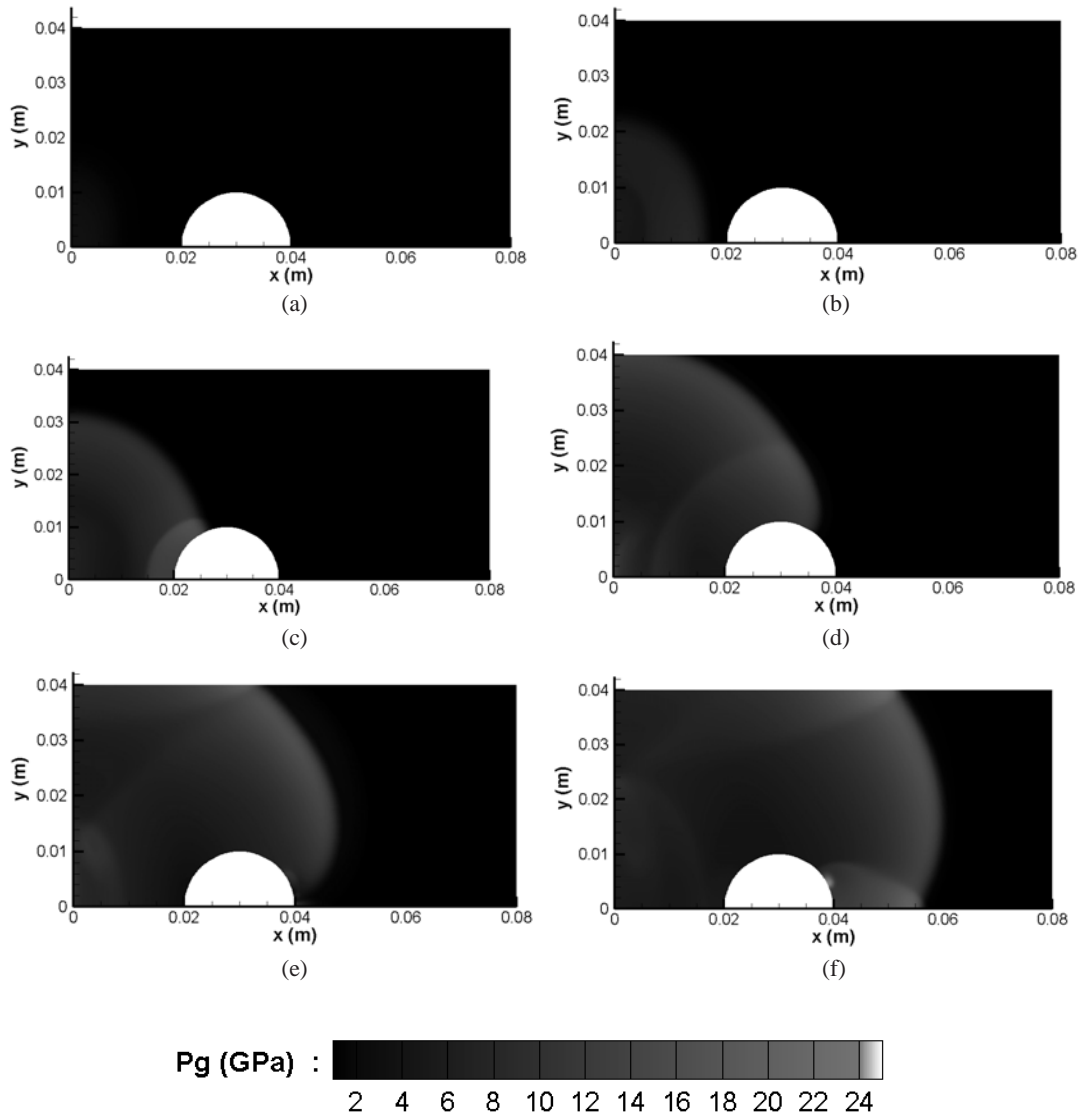
Figure 5.45: Evolution of gas-phase pressure with the effect of spherical wave-shaper for (a) 6, (b) 8, (c) 10, (d) 12, (e) 14, (f) 16 μs
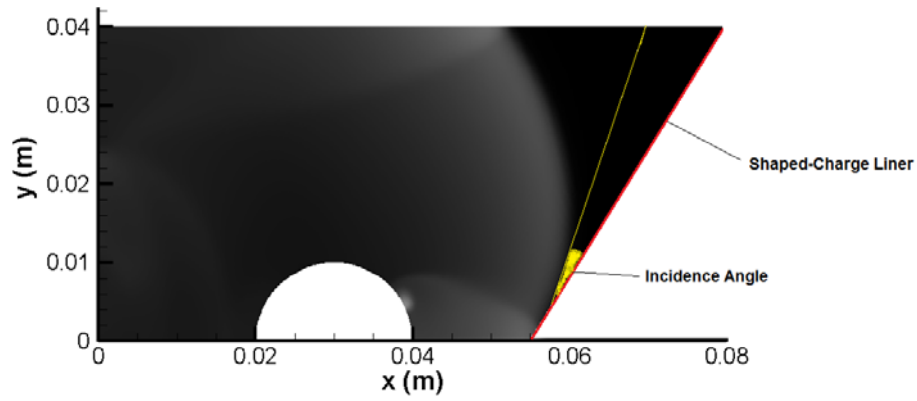
Figure 5.46: Determination of incidence angle for wave-shaper problem

The AutoDYN model is given in Figure 5.47. The Octol 70/30 explosive domain is initiated by Comp-A3 type explosive initiator in the same grid points with our solution. The comparison performed for this wave-shaper problem is focused on the wave structure under the effect of wave-shaper in given form; therefore, these differences in the post-detonation properties are not taken into account.
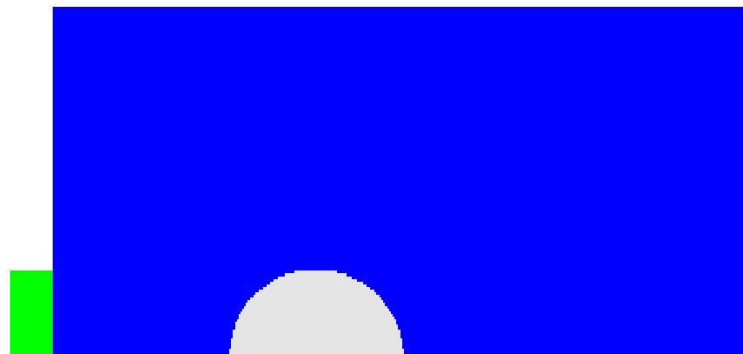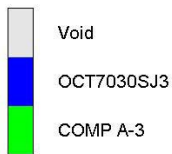
Figure 5.47: AutoDYN solution model for defined wave-shaper problem (AutoDYN solution)

The evolution of the wave structure determined with the AutoDYN solution is given in Figure 5.48. Figure 5.49 illustrates the determination of incidence angle for AutoDYN simulation. Incidence angle is determined to be $12.35°$. There is a very good agreement between the results of current study and AutoDYN solution.

116

(a)　　　　　　　　　　　　　　　　　　　(b)

(c)　　　　　　　　　　　　　　　　　　　(d)

(e)　　　　　　　　　　　　　　　　　　　(f)

PRESSURE (Mbar)

2.500e-01　　2.020e-01　　1.540e-01　　1.060e-01　　5.800e-02　　1.000e-02
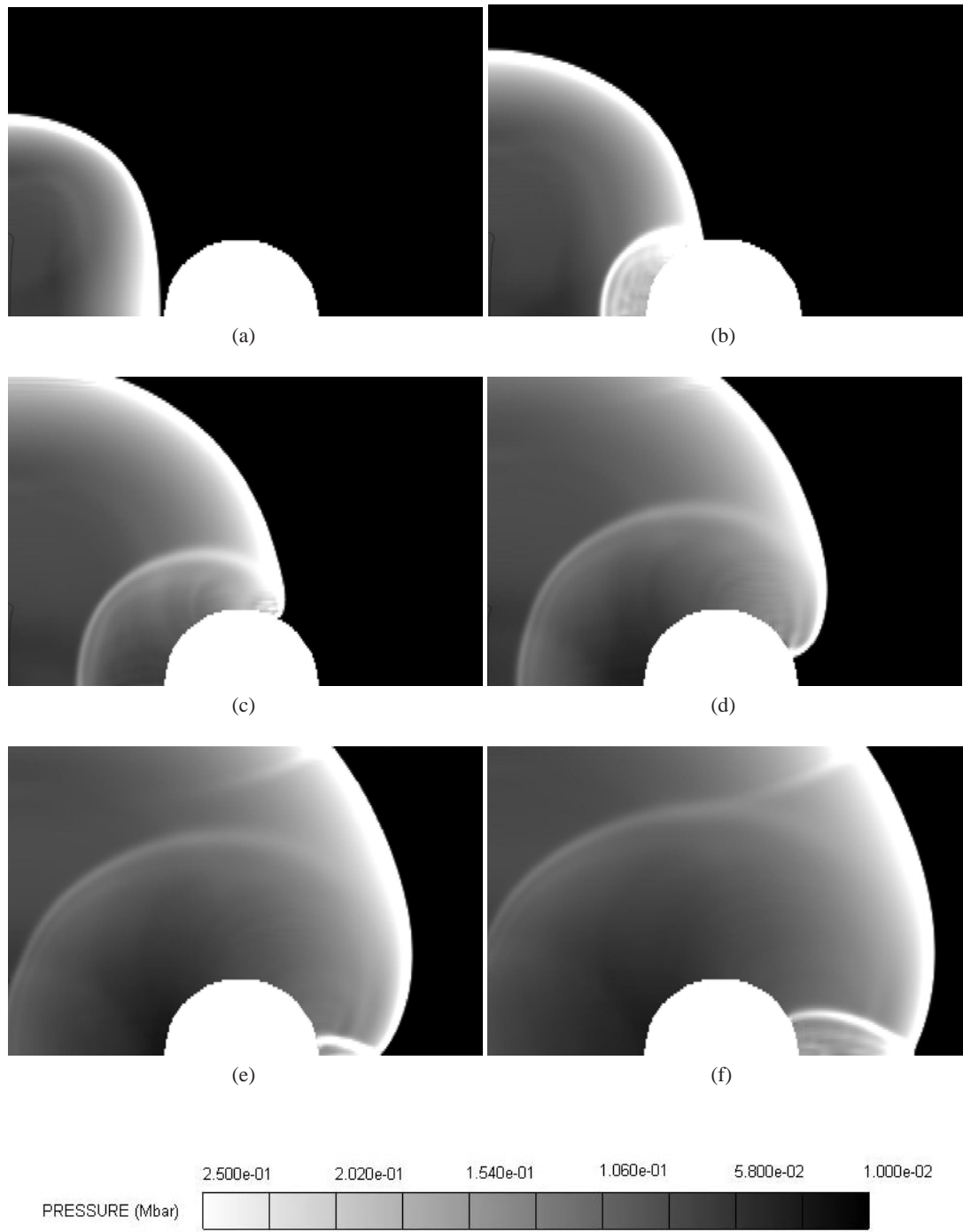
Figure 5.48: Evolution of gas-phase pressure with the effect of spherical wave-shaper for (a) 6.3, (b) 8.4, (c) 10.4, (d) 12.5, (e) 14.6, (f) 16 μs (AutoDYN solution)
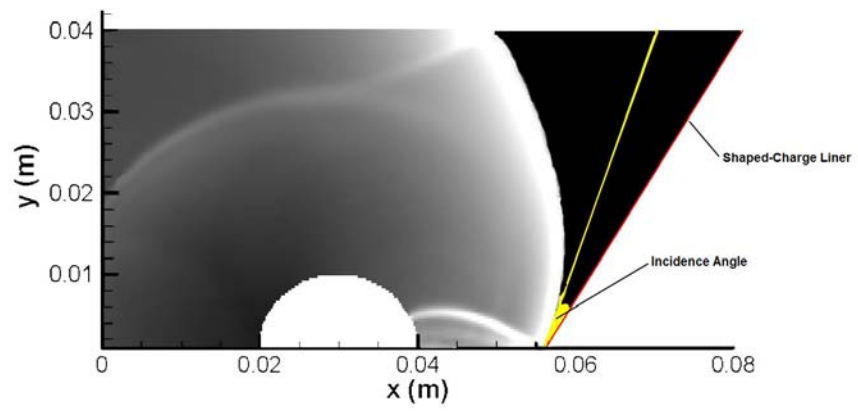
Figure 5.49: Determination of incidence angle for wave-shaper problem (AutoDYN solution)

CHAPTER 6

CONCLUSIONS

This thesis presents the results of numerical studies for simulation of the compaction-to-ignition transition (CIT) and deflagration-to-detonation transition (DDT) phenomena in energetic materials. One-dimensional and two-dimensional numerical computations are performed using solvers running in a parallel computing environment. The solvers are developed through the implementation of the mathematical models given in open literature. Various inert and reactive problems are solved and investigated for the validation of the developed solvers.

The developed solvers are based on the finite difference formulation of the mass, momentum and energy equations in a conservation-law form. Time integration is done via a 6-stage, low storage Runge-Kutta method. Spatial derivatives are approximated using high-order central differencing. The non-physical high-frequency waves and the numerical dispersion errors are avoided applying selective-filtering and shock-capturing method.

The one-dimensional solver is verified using the exact solution of the well-known Sod-case shock tube problem. First, suitable model constants for the numerical method are determined, then, the solution is computed. A very good agreement is achieved. Then, one-dimensional inert compaction and reactive calculations are performed for a typical well-documented explosive ingredient called HMX. In these calculations, formation and evolution of the inert compaction wave in explosive domain is investigated. The mechanical effects (i.e. piston impact), ignition delay (i.e. compaction-to-ignition) and transition characteristics are considered. It is observed that, after piston impact, an inert compaction wave structure appears in the domain during some finite time and along some spatial range. This process is followed by the formation of a high pressure and temperature region. Then in front of this region, more particles are ignited and a deflagration wave front forms which overtakes the compaction wave

after some time limit. In the final stage of the process, deflagration wave shows transition to steady detonation. Post detonation properties of the HMX are also determined in this study and compared to those given the open literature. Reasonably good agreement is observed in comparisons.

Two-dimensional extension of the one-dimensional model is achieved by splitting the inter-phase drag terms into the horizontal and vertical components. Momentum and energy transfers terms are also split to horizontal and vertical components. Different than some other two-dimensional modelling attempts defined in open literature [38, 39], the extension of the one-dimensional model to two-dimensional model is applied in complete two-phase manner. This is the main contribution of this study. The developed two-dimensional solver is tested solving a special shock-tube problem. In this problem, a two dimensional shock-tube with a circular bump is considered. The curvilinear boundary condition implementation is also verified in this numerical test. The computed results are compared to those of a commercial software, and good agreement is observed. After the verification of the developed solver, two-dimensional reactive problems are investigated, which involve sharp and blunt-nosed projectile impact situations on a typical explosive domain with different impact velocities.

In the blunt-nosed projectile impact case at $100m/s$ impact velocity, formation of the compaction wave and high pressure and temperature region is first observed as in one-dimensional case. Then, deflagration wave (primary wave) forms and propagates in the domain. After the formation of the primary wave in the domain, backward wave propagation takes place in the domain to the projectile nose. This backward wave hits to the projectile nose and a secondary wave formation takes place. In addition to formation of this secondary wave structure, with the ignition of particles on flat region of the projectile, a third wave structure is observed. This third wave interacts with the tail of primary wave and with the secondary wave. With the interaction of secondary and triple wave structures, a single wave forms in the high pressure and temperature region of the primary wave.

For the case in which the impact velocity is $150m/s$, different than the 100 m/s impact case, ignition of the particles on the flat region of projectile takes place simultaneously with those of the primary wave. This case the third wave forms around the curved part of the projectile nose and, interacts with the secondary wave forms from the flat region.

In the 100 and 150 m/s impact cases, it is determined that the explosive particles are ignited

with slightly different structures in the domain. To completely resolve the physics behind the 100 and 150 m/s impact cases, some detailed experiments should be performed with specialized visualization techniques (i.e. flash X-ray, Schilieren photography, etc.). In Chapter 5, the physical properties observed for 100 m/s and 150 m/s impact velocities are discussed. For the blunt-nosed projectile impact case with 100 and 150 m/s cases, it is observed that HMX explosive block shows tendency to reaction. Some further calculations are performed for 50 m/s impact velocity to investigate whether the explosive block shows reactive characteristics. It is determined that for 50 m/s impact case, no reaction is observed in the domain. This impact velocity may be concluded as the safety limit for HMX used in this study.

In the sharp-nosed projectile case at $100 m/s$ impact velocity, a similar wave structure is observed as in the case of blunt projectile at $100 m/s$. However, if the impact velocity is increased to $150 m/s$, then, all the process is dominated by the primary wave and no secondary wave formation is observed. Again in the blunt-nosed projectile impact case, the explosive bed shows a reactive characteristic for 100 and 150 m/s impact cases. The calculations with 50 m/s impact velocity are also performed and, it is investigated that, similar to the blunt-nosed case, reaction is not observed in the domain.

In the two-dimensional case studies, a special wave-shaper problem is defined and, results are discussed. It is determined that under the effect of wave shaper, the wave structure is changed to decrease the incidence angle of the wave to shaped-charge liner.

6.1 Future study and suggestions

In this study a bulk ignition criterion is used, which bases on the solid-phase temperature directly. In our calculations, the ignition of the particles is started with the exceed of the bulk solid-phase temperature up to an *ad hoc* level. This is the weakest part of this study. In further studies it is suggested that, the designation and application of more sophisticated and specialized ignition criteria should be applied. This is also concluded in some recent publications, ignition criterion and burn-rate models should be improved to cover the complex physical processes during a typical DDT sequence.

The application of the finite-rate chemistry instead of pressure based burn rate model used in this study is another suggestion for the future studies. The finite-rate chemistry modelling may

be started by using some reduced kinetic models for HMX, RDX, etc. With this application, the deflagration part of the process may be modelled and, the transition features may be observed in more detail.

Another important issue that may be performed in is the improvement of the current solvers to simulate the metal-explosive interactions. This improvement will bring the capability to the solver to perform simulation of the shaped-charge jet formation and, simulation the fragment formation due to case fracture type applications. The solution of these type of problems are very important in terminal ballistics research area and the developed solvers in this study will be used with necessary improvements for the solution of these problems.

REFERENCES

[1] Isler, J., "*The Transition to Insensitive Munitions (IM)*", Propellants, Expolosives, Pyrotechnics, Vol.23, pp. 283-291, 1998.

[2] http://en.wikipedia.org/wiki/1967-USS-Forrestal-fire

[3] http://eaglehorse.org/3-home-station/doha/doha.htm

[4] Hayles, D.R., "*How Safe Should Our Weapons Be ?*", Maxwell Air Force Base, U.S.A., 2005.

[5] http://www.globalsecurity.org/military/systems/munitions/im.htm

[6] STANAG-4439, "*Policy for Introduction, Assesment and Testing for Insensitive Munitions (MURAT)*", NATO-MAS, 1998.

[7] Zukas, A.Z., Walters, P.W., "*Explosive Effects and Applications*", Springer-Verlag New York Inc., 1998.

[8] Narin, B., Özyörük, Y., Ulaş, A. "*Application of Parallel Processing to Numerical Modeling of Two-Phase Deflagration-to-Detonation (DDT) Phenomenon*", International Conference on Parallel Computational Fluid Dynamics, Turkey, 2007.

[9] Narin, B., Özyörük, Y., Ulaş, A. "*One Dimensional, Two Phase Modeling of Deflagration-to-Detonation Transition (DDT)Phenomenon in Porous Energetic Materials*", 4th Ankara International Aerospace Conference, 2007.

[10] Narin, B., Özyörük, Y., Ulaş, A. "*Katı Enerjik Malzemelerde Yanma Patlama Geçişinin İki Fazlı, İki Boyutlu Sayısal Benzetimi*", II. Ulusal Havacılık ve Uzay Konferansı, 2008.

[11] Van Tassel, W.F., Krier, H., "*Combustion and Flame Spreading Phenomena in Gas-Permeable Explosive Materials*", Int. J. of Heat and Mass Transfer, Vol.18, pp. 1377-1386, 1975.

[12] Krier, H., Rajan, S., Van Tassel, W.F., "*Flame-Spreading Combustion in Packed Beds of Propellant Grains*", AIAA Journal, Vol. 14, pp. 301-309, 1976.

[13] Baer, M.R., Nunziato, J.W., "*A Two-Phase Mixture Theory for the Deflagration-to-Detonation Transition (DDT) in Reactive Granular Materials*", International Journal of Multiphase Flow, Vol.12, No.6 , pp 861-889, 1986.

[14] Baer, M.R., Gross, R.J., Nunziota, J.W., Igel, E.A., "*An Experimental and Theoretical Study of Deflagration-to-Detonation Transition (DDT) in the Granular Explosive, CP*", Combustion and Flame, Vol.65, pp. 15-30, 1986.

[15] Chapman, D.L., "*On the Rate of Explosion in Gases*", Philos. Mag., Vol.47, pp. 90-104, 1899.

[16] Jouget, E., "*On the Propagation of Chemical Reactions in Gases*", J. de Mathematiques Pures et Apliquees, Vol.1, pp. 347-425, 1905.

[17] Jouget, E., "*On the Propagation of Chemical Reactions in Gases*", J. de Mathematiques Pures et Apliquees, Vol.2, pp. 5-85, 1906.

[18] Zel'dovich, Y.B., "*On the Theory of the Propagation of Detonation in Gaseous Systems*", Zh. Eksp. Teor. Fiz., Vol.10, pp. 542-568, 1940.

[19] von Neumann, J., "*Theory of Detonation Waves*", John von Neumann collected works, Vol.6, ed. A.J. Taub, New York, Macmillan, 1942.

[20] Döering, W., "*On Detonation Processes in Gases*", Ann. Phys., Vol.43, pp. 421-436, 1943.

[21] Kuo, K.K., Vichnevetsky, R., Summerfield, M., "*Theory of Flame Propagation in Porous Propellant Charges under Confinement*", AIAA Journal, Vol.11, No.4, 1972.

[22] Becstead, M.W., Peterson, N.L., Pilcher, D.T., Hopkins, B.D., Krier, H., "*Convective Combustion Modeling Applied to Deflagration-to-Detonation Transition of HMX*", Combustion and Flame, Vol. 30, pp. 231-241, 1977.

[23] Krier, H., Gokhale, S.S., "*Modelling of Convective Mode Combustion Through Granulated Propellant to Predict Detonation Transition*", AIAA Journal, Vol.16, No.2, pp. 177-183, 1978.

[24] Gough, P.S., Zwarts, F.J., "*Modelling Heterogenous Two-Phase Reacting Flow*", AIAA Jorunal, Vol.17, No.1, 1979.

[25] Gokhale, S.S., Krier, H., "*Modelling of Unsteady Two-Phase Reactive Flow in Porous Beds of Propellant*", Prog. Energy Combust. Sci., Vol. 8, pp. 1-39, 1982.

[26] Butler, P.B., Krier, H., "*Analysis of Deflagration to Detonation Transition in High-Energy Solid Propellants*", Technical Report UILU-ENG-84-4010, Department of Mechanical and Industrial Engineering, University of Illinois at Urbana-Champaign, 1984.

[27] Butler, P.B., Lembeck, M.F., Krier, H., "*Modeling of Shock Development and Transition to Detonation Initiated by Burning in Porous Propellant Beds*", Combustion and Flame, Vol.46, pp. 75-93, 1982.

[28] Butler, P.B., Krier, H., "*Analysis of Deflagration to Detoantion Transition in High-Energy Solid Propellants*", Combustion and Flame, Vol.63, pp. 31-48, 1986.

[29] Markatos, N.C., "*Modeling of Two-Phase Transient Flow and Combustion of Granular Propellants*", International Journal of Multiphase Flow, Vol. 12, No. 6, pp. 913-933, 1986.

[30] Baer, M.R., "*Numerical Studies of Dynamic Compaction of Inert and Energetic Granular Materials*", Journal of Applied Mechanics, Vol. 55, pp. 36-43, 1988.

[31] Powers, J.M., Stewart, D.S., Krier, H., "*Theory of Two-Phase Detonation - Part I : Modeling*", Combustion and Flame, Vol.80, pp. 264-279, 1990.

[32] Powers, J.M., Stewart, D.S., Krier, H., "*Theory of Two-Phase Detonation - Part II : Structure*", Combustion and Flame, Vol.80, pp. 280-303, 1990.

[33] Baer, M.R., Nunziota, J.W., Embid, P.F., "*Deflagration to Detonation Transition in Reactive Granular Materials, Numerical Approaches to Combustion Modelling*", Progress in Astronautics and Aeronautics, Volume 135, 1991.

[34] Bdzil, J.B., Son, S.F., "*Engineering Models of Deflagration-to-Detonation Transition*", Technical Report, LA-12794-MS, Los Alamos National Laboratory,U.S.A., 1995.

[35] Kapila, A.K., Menikoff, R., Bdzil, J.B., Son, S.F., Stewart, D.S., "*Two-Phase Modeling of DDT in Granular Materials: Reduced Equations*", Technical Report, LA-UR-99-3329, Los Alamos National Laboratory, U.S.A., 2000.

[36] Xu, S., Stewart, D.S., "*Deflagration-to-Detonation Transition in Porous Energetic Materials: A Comperative Model Study*", Journal of Engineering Mathematics, Vol. 31, pp. 143-172, 1997.

[37] Bdzil, J.B., Menikoff, R., Son, S.F., Kapila, A.K., Stewart, D.S., "*Two-Phase Modeling of Deflagration-to-Detonation Transition in Granular Materials : A Critical Examination of Modeling Issues*", Physics of Fluids, Vol. 11, Number 2, 1999.

[38] Orth, L.A., "*Shock Physics of Non-Ideal Detonations for Energetic Explosives with Aluminum Particles*", Ph.D. Dissertation, University of Illinois at Urbana-Champaign, 1999.

[39] Xu, S., "*Modeling and Numerical Simulation of Deflagration-to-Detonation Transition in Porous Energetic Materials*", Ph.D. Dissertation, Ph.D. Dissertation, University of Illinois at Urbana-Champaign Graduate College, 1999.

[40] Gonthier, K.A., Powers, J.M., "*A High-Resolution Numerical Method for a Two-Phase Model of Deflagration to Detonation Transition*", Journal of Computational Physics, Vol.163, pp. 376-433, 2000.

[41] Gonthier, K.A., Powers, J.M., "*A Numerical Investigation of Transient Detonation in Granulated Material*", Shock Waves, Vol.6, pp. 183-195, 1996.

[42] Yoh, J.J., "*Thermomechanical and Numerical Modeling of Energetic Materials and Multi-Material Impact*", Ph.D. Dissertation, University of Illinois at Urbana-Champaign Graduate College, 2001.

[43] Kapila, A.K., Schwendeman, D.W., Quirk, J.J., Hawa, T., "*Mechanisms of Detonation Formation Due to a Temperature Gradient*", Combustion Theory Modelling, Vol.6, pp. 553-594, 2002.

[44] Prokhnitsky, L.A., "*Model Detonation of Solid Explosives by the Homogenous Mechanism*", Combustion, Explosion, and Shock Waves, Vol. 39, No.2, pp. 204-210, 2003.

[45] Chinnayya, A., Daniel, E., Saurel, R., "*Modeling Detonation Waves in Heterogeneous Energetic Materials*", Journal of Computational Physics, Vol.196, pp. 490-538, 2004.

[46] Adrianov, N., Warnecke, G., "*The Riemann Problem for the Baer-Nunziato Two-Phase Flow Model*", Journal of Computational Physics, Vol.195, pp. 434-464, 2004.

[47] Saurel, R., Massoni, J., "*On Riemann-Problem-Based Methods for Detonations in Solid Energetic Materials*", International Journal for Numerical Methods in Fluids, Vol.26, pp. 101-121, 1998.

[48] Schwendeman, D.W., Wahle, C.W., Kapila, A.K., "*A Study of Detonation Evolution and Structure for a Model of Compressible Two-Phase Reactive Flow*", Technical Report, Department of Mathematical Sciences, Rensselaer Polytechnic Institute, U.S.A, 2006.

[49] DeOliveira, G., Kapila, A.K., Schwendeman, D.W., Bdzil, J.B., Henshaw, W.D., Tarver, C.M., "*Detonation Diffraction, Dead Zones and the Ignition-and-Growth Model*", 13th International Detonation Symposium, 2006.

[50] Stevens, D.E., Murphy, M.J., Dunn, T.A., "*A Multiphase Model for Heterogenous Explosives in Both the Dense and Dilute Limits*", 13th International Detonation Symposium, 2006.

[51] Chan, S.K., "*Prediction of Confinement Effects on Detonation with an Analytical Two-Dimensional Model*", 13th International Detonation Symposium, 2006.

[52] Stewart, D.S., Yoo, S., Wescott, B.L., "*High-Order Numerical Simulation and Modelling of the Interaction of Energetic and Inert Materials*", Combustion Theory and Modelling, Vol.11, No.2, pp. 305-332, 2007.

[53] Gonthier, K.A., Menikoff, R., Son, S.F., Asay, B.W., "*Modeling Compaction-Induced Energy Dissipation of Granular HMX*", Eleventh International Detonation Symposium, 1998.

[54] Gonthier, K.A., "*Modeling and Analysis of Reactive Compaction for Granular Energetic Solids*", Combustion Science and Technology, Vol.175, pp. 1679-1709, 2003.

[55] Powers, J.M., "*Two-Phase Viscous Modeling of Compaction of Granular Materials*", Physics of Fluids, Vol.16, No.8, pp. 2975-2990, 2004.

[56] Oran, E.S., Weber, Jr., J.W., Stefaniw, E.I., Lefebvre, M.H., Anderson, Jr., J.D. "*A Numerical Study of a Two-Dimensional H_2-O_2-Ar Detonation Using a Detailed Chemical Reaction Model*", Combustion and Flame, Vol.113, pp. 147-163, 1998.

[57] Togashi, F., Löhner, R., Tsuboi, N., "*Numerical Simulation of H_2/Air Detonation Using Detailed Reaction Models*", 44th AIAA Aerospace Sciences Meeting and Exhibit, 2006.

[58] Khokhlov, A.M., Oran, E., Wheeler, J.C., "*A Theory of Deflagration-to-Detonation Transition in Unconfined Flames*", Combustion and Flame, Vol.108, pp. 503-517, 1997.

[59] Fedkiw, R., Merriman, B., Osher, S., "*High Accuracy Numerical Methods for Thermally Perfect Gas Flows with Chemistry*", Journal of Computational Physics, Vol.132, pp. 175-190, 1997.

[60] Gu, X.J., Emerson, D.R., Btadley, D., "*Modes of Reaction Front Propagation From Hot Spots*", Combustion and Flame, Vol.133, pp. 63-74, 2003.

[61] Trotsyuk, A.V., Kudryavtsev, A.N., Ivanov, M.S., "*Numerical Modeling of Standing Gas Detonation Waves*", 9th AIAA/ASME Joint Thermophysics and Heat Transfer Conference, 2006.

[62] Strang, G., "*On the Construction and Comparison of Difference Schemes*", SIAM Journal on Numerical Analysis, Vol.5, No.3, pp. 506-517, 1968.

[63] Swanson, R.C., Radespiel, R., Turkel, E., "*Comparison of Several Dissipation Algorithms for Central Difference Schemes*", ICASE Report No. 97-40, 1997.

[64] Caramana, E.J., Shashkov, M.J., Whalen, P.P., "*Formulations of Artificial Viscosity for Multi-dimensional Shock Wave Computations*", Journal of Computational Physics, Vol.144, pp. 70-97, 1998.

[65] Visbal, M.R., Gaitonde, D.V., "*High-Order-Accurate Methods for Complex Unsteady Subsonic Flows*", AIAA Journal, Vol.37, No.10, pp. 1231-1239, 1999.

[66] Visbal, M.R., Gaitonde, D.V., "*Shock Capturing Using Compact-Differencing-Based Methods*", 43rd AIAA Aerospace Sciences Meeting and Exhibit,2005.

[67] Bogey, C., Bailly, C., "*A Family of Low Dispersive and Low Dissipative Explicit Schemes for Flow and Noise Computations*", Journal of Computational Physics, Vol.194, pp. 194-214, 2004.

[68] Bogey, C., Bailly, C., "*On the Application of Explicit Spatial Filtering to the Variables or Fluxes of Linear Equations*", Journal of Computational Physics, Vol.225, pp. 1211-1217, 2007.

[69] Bogey, C., de Cacqueary, N., Bailly, C., "*Self-Adjusting Shock-Capturing Spatial Filtering for High-Order Non-Linear Computations*", 14th AIAA/CEAS Aeroacoustics Conference (29th AIAA Aeroacoustics Conference),2008.

[70] Berland, J., Bogey, C., Marsden, O., Bailly, C. "*High-Order, Low-Dispersive and Low Dissipative Explicit Schemes for Multiple-Scale and Boundary Problems*", Journal of Computational Physics, Vol.224, pp. 637-662, 2007.

[71] Hirsch, C., "*Numerical Computation of Internal and External Flows, Vol. 1-2*", John Wiley-Sons, 1989.

[72] Toro, E.F., "*Riemann Solvers and Numerical Methods for Fluid Dynamics, 2nd Edition*", Springer, 1999.

[73] Sùceska, M., "*Evaluation of Detonation Energy from EXPLO5 Computer Code Results*" Propellants, Explosives, Pyrotechnics, Vol.24, pp. 280-285, 1999

[74] Sùceska, M., "*EXPLO5-Computer Program for Calculation of Detonation Parameters*" Proc. of 32th Int. Annual Conference of ICT, pp. 110/1, 2001

[75] Sùceska, M., "*Calculation of Detonation Parameters by EXPLO5 Computer Program*" Material Science Forum, Vol. 465-466, pp. 325-330, 2004

[76] Mader, C., "*Numerical Modeling Explosives and Propellants*", CRC Press, 2nd Edition, 1998.

[77] Hwang, K., Xu, Z., "*Scalable Parallel Computing, Technology, Architecture, Programming*", McGraw-Hill Science/Engineering/Math, 1st Edition, 1998.

[78] Kaya, M., "*Path Optimization of Flapping Airfoils Based on Unsteady Viscous Flow Solutions*", Ph.D. Dissertation, Middle East Technical University, 2008.

VITA

PERSONAL INFORMATION

Surname, Name   : Narin, Bekir
Nationality   : Turkish (TC)
Date and Place of Birth : April 1977, Kayseri
Phone   : +90 (312) 590 9089
E-mail   : bnarin@sage.tubitak.gov.tr

EDUCATION

Degree	Institution	Year of Graduation
M.S.	METU Aerospace Engineering	2001
B.S.	METU Aeronautical Engineering	1999
High School	Malatya Science High School	1994

ACADEMIC EXPERIENCE

Year	Place	Enrollment
2002-Present	TÜBİTAK-SAGE	Chief Research Engineer
1999-2002	METU Aerospace Engineering Dept.	Graduate Research Assistant

RESEARCH INTERESTS

Detonation Physics, Computational Fluid Dynamics, Parallel Processing

FOREIGN LANGUAGES

Advanced English, Intermediate Spanish

INTERNATIONAL CONFERENCE PRESENTATIONS

1. B. Narin, Y. Özyörük, A. Ulaş, *One-Dimensional, Two-Phase Modeling of Deflagration-to-Detonation Transition Phenomenon in Porous Energetic Materials*, 4th Ankara International Aerospace Conference, Ankara, Turkey, 2007

2. B. Narin, Y. Özyörük, A. Ulaş, *Application of Paralel Processing on Two-Phase Deflagration-to-Detonation (DDT) Modeling*, Proceedings of Parallel CFD 2007 Conference, Antalya, Turkey, 2007

3. F. Cengiz, B. Narin, A. Ulaş, *GASPX: A Computer Code For The Determination of The Detonation Properties of Energetic Premixed Gaseous Mixtures*, 10th International Seminar, NTREM, Czech Republic, Pardubice, 2007

4. F. Cengiz, B. Narin, A. Ulaş, *BARUT-X: A Computer Code For Computing The Steady-State Detonation Properties of Condensed Phase Explosives*, 10th International Seminar, NTREM, Czech Republic, Pardubice, 2007

5. B. Narin, Y. Özyörük, A. Ulaş, *Development of a One-Dimensional Solver for Two-Phase, Reactive, Deflagration-to Detonation Transition Phenomenon in Porous Energetic Materials*, 3rd Ankara International Aerospace Conference, Ankara, Turkey, 2005

NATIONAL CONFERENCE PRESENTATIONS

1. B. Narin, Y. Özyörük, A. Ulaş, *Katı Enerjik Malzemelerde Yanma-Patlama Geçişinin, İki-Fazlı, İki-Boyutlu Sayısal Benzetimi*, 2nci Ulusal Havacılık ve Uzay Konferansı (UHUK 2008), İstanbul, 2008

2. F. Cengiz, B. Narin, A. Ulaş, *Kararlı Durum Ve Kimyasal Denge Koşulunda Patlama Tepkimesinin Modellenmesi Ve Uygulamalar*, Üçüncü Savunma Teknolojileri Kongresi (SAVTEK), Ankara, 2006